Summer 8-15-2019

Development and Application of New Methods for Magnetic Resonance Elastography of the Brain

Charlotte Anne Guertler
Washington University in St. Louis

WASHINGTON UNIVERSITY IN ST. LOUIS

School of Engineering and Applied Sciences

Department of Mechanical Engineering and Materials Science

Dissertation Examination Committee:
Philip V. Bayly, Chair
Hong Chen
Joel Garbow
Mark Meacham
Ruth J. Okamoto

Development and Application of New Methods for Magnetic Resonance Elastography of the Brain

by

Charlotte A. Guertler

A dissertation presented to
The Graduate School
of Washington University in
partial fulfillment of the
requirements for the degree
of Doctor of Philosophy

August 2019
Saint Louis, Missouri

Table of Contents

List of Figures

List of Tables

Acknowledgments

Dr. Philip Bayly has been an extraordinary mentor during my time at Washington University over the last five years. His approachability and guidance drew me to Washington University and to his research group. I am constantly amazed at how he manages the responsibilities as chair, professor, and head project investigator while still making time to troubleshoot experiments and code, edit papers and presentations, and meet with students. His energy and enthusiasm for learning and research is contagious. I am honored to continue to work with him after graduation.

Dr. Ruth Okamoto is a wonderful mentor and research partner. Our lab would not function without her. She has been essential to my growth as researcher, helping me with experiments, data analysis, and countless other research activities. Ruth's unyielding attention to detail has opened my eyes to complexity and beauty in minutia I would have overlooked. Under her wing, I have learned to question what is "known". I look forward learning more with her as a colleague in the new makerspace.

I was lucky to have additional mentorship from Dr. Andrew Badachhape and Dr. John Schmidt as their fellow graduate student. Andrew frequently paused his work to answer my questions, which helped the *in vivo* scan preparations and analysis go smoothly. John was essential in my expansion into finite element modeling and *ex vivo* scanning. He taught me to operate the scanner and gave me the foundation to successfully incorporate ultrasound actuation into the experimental procedure. I happy to have Andrew and John as role models and friends.

Dr. Curtis Johnson at University of Delaware provided the MR elastography sequences for the *in vivo* brain studies. MR technologist Linda Hood helped with the *in vivo* scans and taught me how to set up and run the MRI scanner. The staff of the Department of Comparative Medicine at Washington University, specifically Dr. Michael Talcott and Charles Mitchell, were accommodating and helpful when I was designing the actuation device and performing the *in vivo* mini-pig scans.

Members of the Bayly Lab have been wonderful to work alongside. The graduate and undergraduate students over the years have fostered a friendly, fun, and educational environment. I had the pleasure to work directly with two undergraduates, Rachel Mickelson and Jake Ireland. Both were enthusiastic and dedicated to their projects and helping others.

I would like to acknowledge the Biomedical Magnetic Resonance Laboratory (BMRL), specifically Dr. Joel Garbow, Dr. Xia Ge, and Dr. James Quirk. Dr. Xia Ge and Dr. James Quirk were always available to help with any issues that arose during scanning. Dr. Joel Garbow provided mentorship for the research connected to my final aim.

The Chen lab was essential in starting the MR-HUM project. Dr. Hong Chen taught me the basics of ultrasound and provided mentorship for the MR-HUM project. Her PhD student, Chris Pacia, was always willing to help me solve the issues that arose when using the Image Guided Therapy (IGT) system. Erik Dumont installed the IGT system at Washington University and trained me on the equipment.

The Mechanical Engineering and Materials Science department has contributed to my success as a graduate student. Linda Buckingham, Laura Barker, Kevin Cowell, and Felicia Dilworth helped

with everything from administrative tasks and educational requirements to answering miscellaneous concerns or questions. Gene Bulfin maintained the computational and modeling resources for the lab, which was vital to the research.

Financial support for this work was provided by Imaging Sciences Pathway Fellowship NIH 5T32 EB01485505, NIH R01 NS 055951, ONR N00014-15-C-5160, NSF CMMI-1332433, NSF CMMI-1727412. In addition to funding, the Imaging Sciences Pathway Fellowship provided me with a good foundation of imaging science. Through this fellowship I learned about the basics of biological imaging, strengthened my biological background, and was exposed to cutting-edge imaging research. Because of this fellowship, I was ultimately able to graduate with a Certificate in Imaging Science.

Charlotte A. Guertler

Washington University in St. Louis

August 2019

To my family and friends: your unwavering support inspires me to believe in myself and empowers me to achieve my goals.

Abstract of the Dissertation

Development and Application of New Methods for Magnetic Resonance Elastography of the Brain

by

Charlotte A. Guertler

Doctor of Philosophy in Mechanical Engineering and Materials Science

Washington University in St. Louis, 2019

Professor Philip V. Bayly, Chair

Accurate mechanical properties of the intact, living brain are essential for modeling traumatic brain injury (TBI). However, the properties of brain tissue *in vivo* have traditionally been measured in *ex vivo* samples. Magnetic resonance elastography (MRE) can be used to measure motion and estimate material properties of soft tissues *in vivo*, but MRE typically assumes tissue isotropy and homogeneity. The objective of this thesis is to improve MRE of soft tissue, like the brain, by developing and evaluating methods for *in vivo* estimation of heterogeneous, anisotropic properties. This was achieved through pursuit of the following aims: (1) quantifying the differences between *in vivo* and *ex vivo* brain tissue, thereby clarifying the need for *in vivo* measurements; (2) introducing and applying a new approach to anisotropic MRE, using data obtained during external actuation of the porcine brain *in vivo*, which highlighted the need for new actuation methods; and (3) developing and evaluating a method for anisotropic property estimation using MRE with actuation by harmonic focused ultrasound (FUS). This research has led to new methods for anisotropic MRE, and improved material property estimates of the brain and other soft tissues.

Chapter 1: Mechanical Characterization of Brain Tissue: Magnetic Resonance Elastography, Mechanical Anisotropy, and Focused Ultrasound

1.1 Overview

Accurate mechanical characterization of biological soft tissues, like the brain, is important for the understanding of injury and disease. Simulations are useful in describing and understanding injury biomechanics, but they require accurate material properties. Unfortunately, knowledge of brain tissue material properties is still limited due to its inaccessibility for direct, *in vivo* characterization. Most biological tissues are viscoelastic and mechanically anisotropic, yet they are often modeled in simulations as elastic and isotropic due to the lack of experimental data on anisotropic properties. To improve the estimation of material properties and improve simulations, more experimental data and better methods for anisotropic parameter estimation are needed. This chapter reviews current and past efforts to characterize and simulate soft tissues, with a focus on elastography techniques.

1.2 Motivation and Significance

1.2.1 Traumatic brain injury (TBI) modeling

Traumatic brain injury (TBI) occurs when sudden head acceleration leads to shearing and stretching of brain tissue [2, 3]. In 2014, over 2.87 million people were diagnosed with a TBI based

on records from emergency department visits, hospitalizations, and deaths [4]. Figure 1.1 shows the trends of TBIs from emergency department visits, hospitalizations, and deaths from 2006 to 2014 (EDHD).

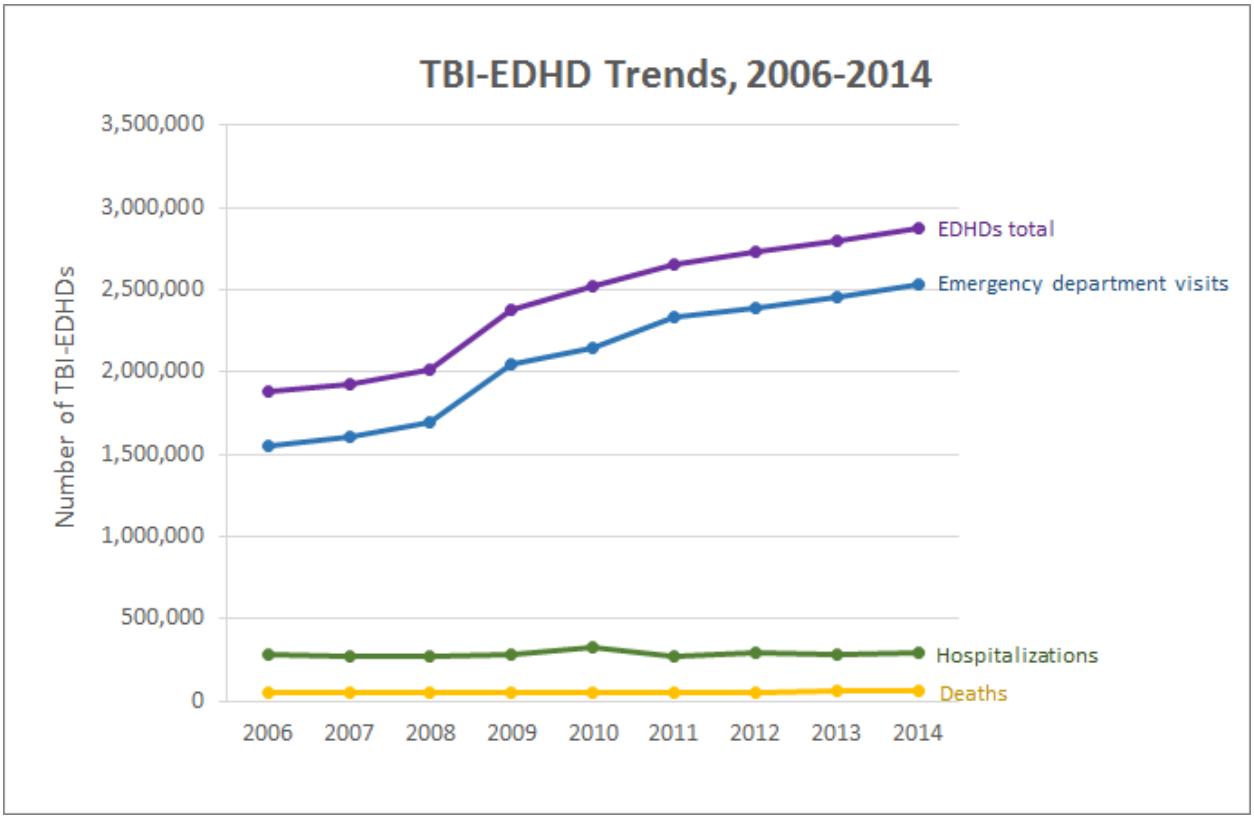

Figure 1.1: Trends of TBI from 2006 to 2014 of emergency department visits, hospitalizations, and deaths from 2006 to 2014 (EDHD) in the United States. Over this time period, the total number of TBI EDHDs increased by 53%. By 2014, there were over 2.87 million TBI EDHDs in the United States, with over 837,000 of those among children. Figure reproduced from [4].

TBI can result in physical, cognitive, behavioral, and/or emotional impairments. These effects can last for a few days to a person's entire life [4]. Severe TBI is considered one of the most disabling injuries [5]. Despite the prevalence and potential severity of TBI, the mechanisms by which head impact leads to neural injury are still unknown [6]. Computer models can be used to simulate TBI, particularly the mechanics of fast brain deformation. Simulations can, in principle, be used to improve methods for injury prevention, diagnosis, and treatment of TBI. To make relevant

computer models of TBI, accurate representations of the material properties for brain tissue are necessary [7]. The mechanical behavior of the brain tissue remains incompletely characterized [8]. Characterizing the mechanical properties of brain tissue is challenging in part due to the inability to directly test the brain, and in part due to the inherent structural and mechanical complexity of its tissue.

Since the brain is completely enclosed by the skull, direct mechanical testing of the brain *in vivo* is not possible. Therefore, most models are based on mechanical properties for brain tissue that has been obtained from human cadavers or animals *ex vivo* [9-17]. However, *ex vivo* measurements may not necessarily reflect *in vivo* behavior [18, 19]. A small number of tests have been performed using indentation of the intact brain *in situ* and *in vivo* in animals [18, 20]. Magnetic resonance elastography (MRE) has also been performed on both animals and humans [21-25]. Sizable differences have been found between estimates of material parameters from different studies, likely due to differences in methodology, frequency range, or time scale. Comparison between *in vivo* and *ex vivo* results [26] are limited and more research is necessary to better characterize the differences.

1.2.1 Mechanical anisotropy

In addition to the lack of data on the differences between *in vivo* and *ex vivo* measurements, there is a dearth of experimental data and simulations that account for the mechanical complexity of the brain. Brain tissue, specifically white matter, is structurally anisotropic (Figure 1.2), which likely causes the tissue's mechanical properties to be directionally dependent (i.e., different for loading parallel or perpendicular to axonal fibers) [27, 28]. Anisotropy may have an impact in injury and disease mechanisms, so understanding its effects is important for the study of biological tissues.

Characterizing anisotropic properties is important for developing more accurate and reliable computer models that can improve our understanding, diagnosis, and treatment of injury and diseases [29]. However, despite the potential importance of anisotropy in mechanical behavior, direction-dependent mechanical properties are often ignored, and simpler, isotropic material models are used [28, 29]. This is largely due to the complexity of more accurate models. Anisotropic properties of soft materials are difficult to test and analyze. MRE can be used to measure the anisotropic shear and tensile properties of transversely isotropic soft tissue like brain tissue by analyzing shear wave propagation at different angles relative to the fiber orientation and polarization direction [30, 31]. Accurate and comprehensive characterization requires the same sample to be analyzed with multiple shear wave propagation and polarization directions. There is a need for more experimental data investigating the anisotropic material properties of biological tissues using multiple propagation directions.

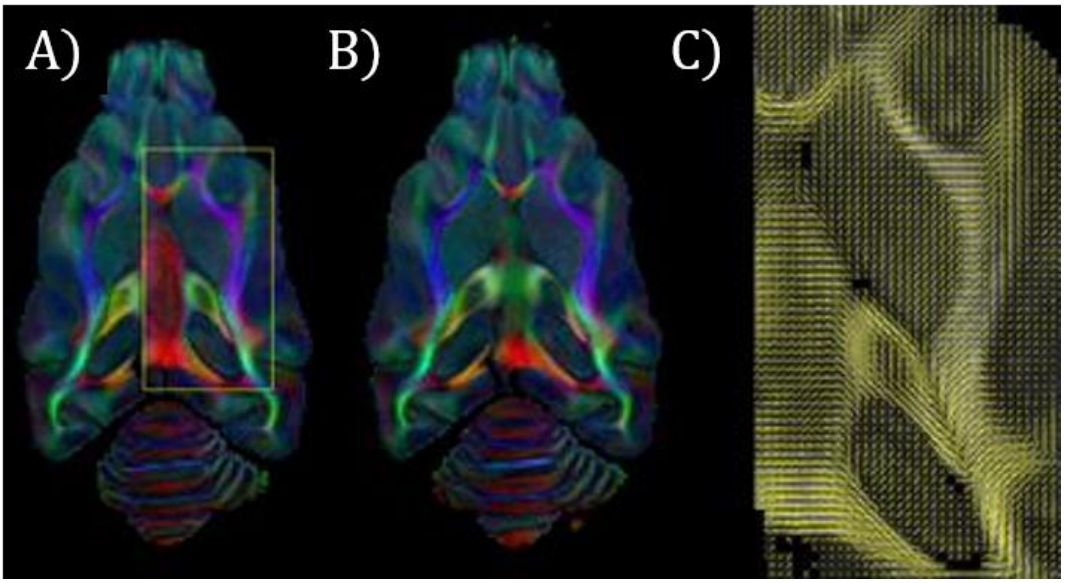

Figure 1.2: Diffusion tensor images (DTI) of structural anisotropy in the ferret brain. Diffusion, measured by MR imaging sequences, is faster along the dominant fiber direction. (A-B) The direction of maximum diffusivity is indicated by color (red = left-right; green = front-back; blue = up-down). Brightness indicates the magnitude of diffusion anisotropy. (C) Vector field of dominant fiber direction inferred from the direction of maximum diffusivity for the zoomed-in area outlined in (A). Figure reproduced from proposal CMMI-1332433 (PI: PV Bayly).

Novel actuation methods are necessary for improved anisotropic property estimation. To acquire shear wave propagation at multiple different angles relative to fiber orientation, the actuator that generates shear waves should ideally be non-invasive and be able to produce waves with controlled propagation and polarization directions. Current MRE methods *in vivo* typically use actuators either on the surface of a tissue or body part [23, 32-34] while *ex vivo* methods may utilize a thin rod inside the tissue [30] for excitation. Another *ex vivo* method involves surface actuators, which noninvasively vibrate the surface of the sample. However, since small shear waves dissipate rapidly, excitation from surface actuators may be unable to reach the area of interest in the tissue. In addition, the propagation direction is difficult to control as waves typically propagate inwards from the surface. Internal excitation with a thin rod or needle directly applies displacement to the center of the tissue, so dissipation is less of an issue. However, this method is destructive to the tissue, so only one wave and propagation direction can be observed per sample. These limitations

underscore the need for a non-invasive, localized, direct, and nondestructive MRE actuator to study anisotropy.

1.3 Modeling the Mechanics of the Brain

Since the 1970s, researchers have been developing finite element head models to understand the brain mechanics of head impacts and injury [28]. These models investigate head impact [35-41], brain injuries [36, 42-45], and types of accelerations [46]. Figure 1.3 shows an example finite element model of the human head used in head impact and TBI research [41].

These models have provided insight into impacts and injury, but models are only as good as their assumptions and inputs. Most models are either unvalidated or validated using data from a sparse set of radio-opaque markers in cadaver brain [36, 37, 39, 45]. Validation of models is limited due to the lack of experimental data [45]. All the simulations cited above use isotropic material models, despite the potential anisotropy of brain tissue, due the lack of knowledge of anisotropic parameters [28, 45]. Majority of the finite element head models assume linear elasticity, with only a few models incorporating viscoelasticity or hyperelasticity [28].

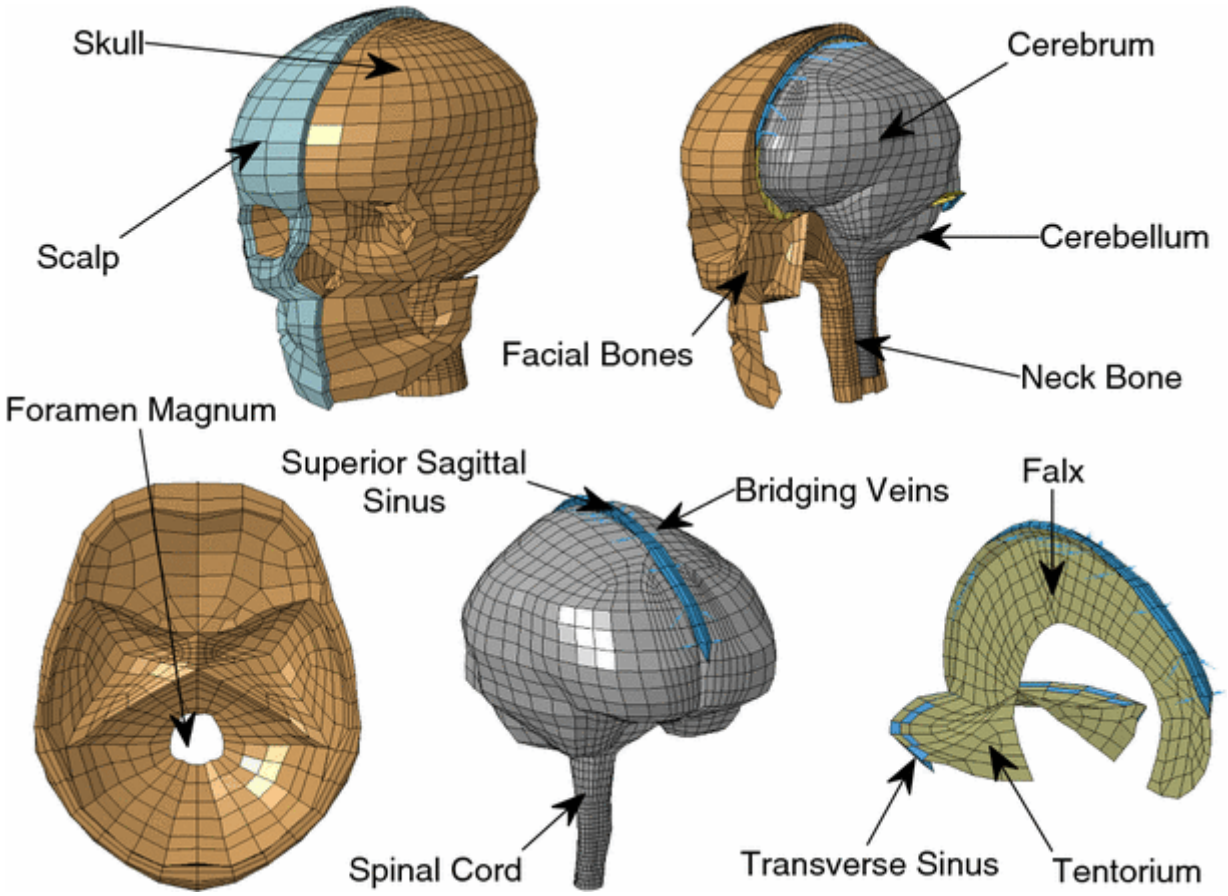

Figure 1.3: Example finite element model of the human head used in brain injury prediction. Top row shows the human head model with the open skull and exposed brain. The bottom row shows the details of the skull base, brain membranes, and bridging veins that are included in the model. This figure was reprinted from [41]

1.4 Elastography Imaging for Mechanical Property Estimation

Elastography imaging techniques provide a non-invasive quantitative evaluation of soft tissue mechanical properties. Material properties can be estimated from induced shear waves based on their propagation properties [47]. The mechanical excitation of the shear waves can be provided by external actuation, acoustic radiation force, or internal physiologic motion [48]. The displacement and velocity of the shear waves are imaged using either ultrasound-based techniques

or MRI based techniques. Examples of ultrasound-based elastography imaging are transient elastography (TE) [49], acoustic radiation force impulse imaging (ARFI) [50], and harmonic motion imaging (HMI) [47, 48]. Examples of MR-based elastography imaging are Magnetic Resonance Elastography (MRE) [51] and MR acoustic radiation force impulse imaging (MR-ARFI) [52]. MRI based techniques provide better resolution than ultrasound imaging based techniques, but ultrasound elastography is cheaper and more compact. This thesis focuses on MRI based techniques, specifically MRE.

1.4.1 Magnetic Resonance Elastography (MRE)

Magnetic resonance elastography (MRE) is an imaging technique for measuring the mechanical properties of soft tissue [51]. In MRE, shear waves are induced in tissue by harmonic external mechanical actuation; these waves are then imaged with a modified MR imaging sequence that includes harmonic, motion-sensitizing gradients. The material properties of tissue can be calculated using local wavelength estimation, direct inversion of the viscoelastic shear wave equation, phase gradient analysis, or finite element methods [53]. Deformations are typically very small (<0.1% strain) so only the linear, viscoelastic properties that govern behavior in this regime can be estimated. However, these parameters are important and complementary to parameters that describe large-amplitude, quasi-static response.

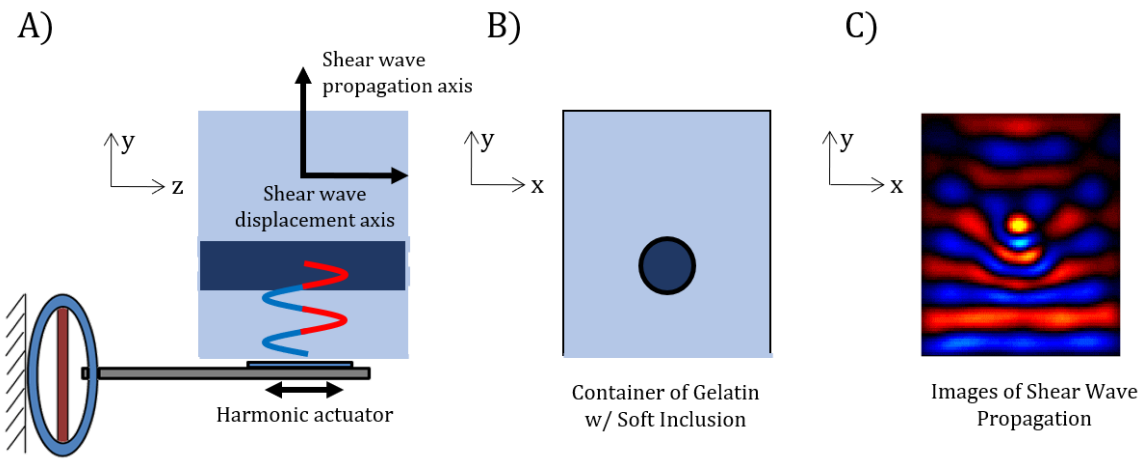

Figure 1.4: MRE in a container of gelatin with a soft inclusion. (A) Schematic of MRE actuation of sample with inclusion along the *y-z* plane. Shear waves are actuated using a harmonic actuator on the bottom surface. Red and blue sinusoid represents the peaks and valleys of the shear wave traveling through the sample. The stiffer gelatin is shown in light blue and the softer gelatin is shown in dark blue. Arrows denote the shear wave propagation and displacement axes. (B) Schematic of gelatin sample with inclusion along the *x-y* plane. (C) MRE images of shear wave displacements in the gelatin sample along a *x-y* plane. Waves travel faster in stiffer materials (longer wavelength) and slower in softer materials (shorter wavelength). (Original figure created by Erik Clayton.)

MRE has been used as a research and clinical tool to characterize tissues, like brain, liver, and muscle, *in vivo* and to study changes in stiffness due to aging, disease, or injury [33, 34, 54, 55]. However, estimates of brain properties obtained by MRE [17, 26, 33, 56, 57] tend to differ from estimates of properties measured *ex vivo* by direct mechanical tests [17, 58-60]. It is not clear whether methodological differences or actual differences in properties explain these conflicting results.

1.4.2 Acoustic radiation force-based elastography

Acoustic radiation force can be used as a method of remote shear wave actuation for elastography. In this approach, an ultrasound beam is concentrated into a focal region, which creates localized tissue displacement from acoustic radiation force [48, 61]. The shear waves in the tissue are formed by generating impulsive radiation force or harmonic radiation force [61]. Examples of shear waves generated from impulsive forces include acoustic radiation force imaging (ARFI, MR-ARFI,

mpARFI) [50, 52, 62-64], transient MRE (t-MRE) [65], spatially modulated ultrasound radiation force (SMURF) [66], shear wave elasticity imaging (SWEI) [67], supersonic shear imaging (SSI) [68], shear wave spectroscopy (SWS) [69]. Examples of shear waves generated from harmonic radiation force include harmonic motion imaging (HMI) [48, 70], vibro-acoustography [71, 72], shear wave dispersion ultrasound vibrometry (SDUV) [73], and crawling wave spectroscopy (CWS) [74]. Several of these techniques (MR-ARFI, t-MRE, mpARFI, MR-HUM) combine ultrasound-generated pulses with MRI imaging, but majority of the acoustic radiation-based elastography, including all harmonic radiation force methods, use ultrasound for both harmonic actuation and data recording.

1.5 Current Methods for Estimating Anisotropic Parameters

Anisotropic elastography has most commonly been used to try to estimate **two** elastic parameters of a transversely isotropic (TI) material model: the shear moduli governing shear in planes parallel and perpendicular to the fiber direction. These 2-parameter models are incomplete, as TI materials can have different tensile moduli as well [31] (see Chapter 2). Such studies have been performed on breast tissue [75], muscle tissue [29, 76-79], anisotropic phantoms [29], and aligned fibrin gels [80]. MRE can also be used to estimate **three** parameters (such as shear modulus, shear anisotropy, and tensile anisotropy) for incompressible TI (ITI) material models [58, 78, 81]. It is also possible to try to estimate **five** parameters for general TI material models, or more for general orthotropic models [82]. For the 3-parameter model, Tweten et al. [31] showed by simulation that two types of shear waves must exist, with propagation of both waves in different directions, to estimate

accurately the three material parameters. In the human brain, Anderson et al. [83] used multiple excitation methods and showed that estimates of isotropic material parameters depended on the directional properties of the wave field. Schmidt et al. [30] actuated tissue in two different directions to image displacements from the two types of shear waves described by Tweten et al. [31]. Theoretical studies include ITI finite element models [84], an approach for ITI using ultrasound elastography [85], and a finite element model that incorporates axonal anisotropy [27]. Gennisson et al. [86] used ultrasound elastography to study transversely isotropic phantoms and measured shear moduli parallel and perpendicular to the fibers. Other recent ultrasound studies [87, 88] describe two different shear-wave speeds in transversely isotropic phantoms, but anisotropy is not fully addressed.

1.7 Summary

The mechanical properties of biological tissue are needed to help predict, prevent, diagnose, and develop treatments for disease and injury, including TBI. Using the correct mechanical properties is essential to accurately simulate brain biomechanics. It is important to characterize the differences in brain tissue *in vivo* and *ex vivo*, model anisotropic behavior, and improve actuation methods to probe the material response.

1.8 Specific Aims and Dissertation Outline

The goal of this thesis is to address some of the limitations of material property estimation in MRE with the following aims:

Aim 1: Determine if differences exist between material properties of brain tissue measured in vivo and ex vivo, and, if so, quantify them.

Aim 2: Estimate the contributions of shear and tensile anisotropic mechanical properties estimated by MR elastography in simulations and experiments with external (boundary) excitation of shear waves.

Aim 3: Estimate anisotropic material parameters in soft tissue by MRI of ultrasound-induced shear waves.

Chapter 2 provides an overview of the mathematical theory required to perform this work. Basic principles of continuum mechanics and wave motion are reviewed. Principles underlying imaging and analysis procedures are also briefly summarized in this chapter.

Chapter 3 describes experimental work performed to estimate and compare material properties of the porcine brain *in vivo* and *ex vivo* (Aim 1). Data was collected using MRI and MRE for 6 Yucatan mini-pigs. Local direct inversion (LDI) was performed on all data to estimate the material properties of the brain tissue *in vivo* and *ex vivo*.

Chapter 4 presents data from simulations of *in vivo* porcine brain, and analysis of the effects of shear and tensile anisotropy on shear waves excited by boundary actuation (Aim 2). Wave fields were separated into slow and fast shear waves and analyzed using directional-filtered, local direct inversion (DF-LDI).

Chapter 5 describes MR imaging of shear waves induced by acoustic radiation force of focused ultrasound. MR imaging of harmonic ultrasound-induced motion (MR-HUM) can noninvasively excite shear waves in soft tissues for the purpose of material property estimation. A benefit of this method is that a sample can be sequentially tested in multiple orientations to produce a variety of propagation and polarization directions for analysis of anisotropic behavior.

Chapter 6 describes the estimation of anisotropic parameters from MR-HUM. Two methods of analysis, directional filtered local direct inversion (DF-LDI) and phase gradient (PG), are applied to simulated and experimental data and the results are compared.

Chapter 7 concludes the thesis and discusses experimental limitations and future work.

1.9 Statement of Contributions

This thesis is a culmination of my work in the Bayly Lab at Washington University in St. Louis from May 2015 through June 2019. All aspects of the research presented in the thesis were advised by Philip Bayly and Ruth Okamoto. The following paragraphs describe my contributions in more detail.

The work described in chapter 3 is reproduced from Guertler et al. 2018 [89]. This journal publication was a collaboration with the other co-authors. I designed the *in vivo* actuation device, performed all *in vivo* experiments with the help of Ruth Okamoto, analyzed the data, and wrote the paper. Curtis Johnson developed all of the MRE sequences for *in vivo* experiments; MRE sequences for *ex vivo* studies were adapted by Philip Bayly from standard spin-echo sequences.

John Schmidt performed all *ex vivo* experiments. Andrew Badachhape assisted with brain sample preparation.

The work described in chapter 4 is based on a collaboration with Philip Bayly to develop anisotropic parameter estimation through separation of slow and fast waves. The finite element models represent a significant extension of work by Dennis Tweten, who built a finite element model of an isotropic cube with two fiber tracts at 45˚. I created finite element models with multiple fiber and actuation directions. I performed the analysis of the simulations and applied it to data from the mini-pig *in vivo* (from scans described in chapter 3).

The work described in chapters 5 and 6 is based on a collaboration with Philip Bayly, Hong Chen, and Joel Garbow. The three collaborators worked with Image Guided Therapy to design the focused ultrasound system for MR-HUM. I performed all initial testing for generation of harmonic shear waves in phantoms. I did all sample preparation, experiments, and data analysis. Jake Ireland and Ryan Castile helped perform the dynamic shear testing and biaxial testing, respectively. I worked with Philip Bayly on the development and refinement of the anisotropic parameter estimation analysis.

Chapter 2: Theoretical Background and Imaging Methods

2.1 Overview

This chapter reviews the basic theory of elasticity. Constitutive relationships for isotropic and transversely isotropic, linear, elastic material models are introduced. Next, the theory of plane wave propagation is presented for harmonic shear waves in isotropic and transversely isotropic materials. Finally, this chapter summarizes the theory and application of the imaging techniques, like magnetic resonance elastography (MRE), and diffusion tensor imaging (DTI).

2.2 Theory

2.2.1 Equilibrium

Mechanical equilibrium is the state where the sum of all forces acting on a body are in balance. This is defined by Newton's second law, where the sum of forces acting on a body are equal to the body's mass multiplied with its acceleration. This law can be applied to a material element of an arbitrary solid to relate the components of the stress tensor ($\boldsymbol{\sigma}$) and the displacement vector ($\boldsymbol{u}$):

$$\frac{\partial \sigma_{ij}}{\partial x_i} = \rho \frac{\partial^2 u_j}{\partial t^2} \tag{2.1}$$

where ρ is the density, $\boldsymbol{x}$ is spatial vector (expressed in Cartesian coordinate system as $\boldsymbol{x} = x_i \boldsymbol{e_i}$), t is time, and i, j are indices representing tensor components (also known as index or Einstein notation) where $i, j = 1, 2, 3$ for the three dimensions (x, y, z).

2.2.2 Constitutive Laws for Linear Elastic Materials

2.2.2.1 General stress/strain relationships

Stress (σ) is the measure of forces on an element. For a simple, 2D material, stress is equivalent to force over area. Strain (ε) is the measure of deformation of an element. For a simple, 2D material, strain is equivalent to the change in length over the original length. In three dimensions, the infinitesimal strain tensor can be defined as

$$\varepsilon_{ij} = \frac{1}{2}\left(\frac{\partial u_i}{\partial x_j} + \frac{\partial u_j}{\partial u_i}\right) \tag{2.2}$$

For a linear elastic material under small deformations, the generalized Hooke's law can be used to relate stress and strain

$$\sigma_{ij} = C_{ijkl}\varepsilon_{kl}, \tag{2.3}$$

where C_{ijkl} is the rank-four elasticity, or stiffness, tensor. This tensor can be represented compactly as a matrix using Voigt notation to produce the elasticity (or stiffness) matrix:

$$\begin{bmatrix}\sigma_{11}\\ \sigma_{22}\\ \sigma_{33}\\ \sigma_{23}\\ \sigma_{13}\\ \sigma_{12}\end{bmatrix} = \begin{bmatrix} c_{11} & c_{12} & c_{13} & c_{14} & c_{15} & c_{16} \\ & c_{22} & c_{23} & c_{24} & c_{25} & c_{26} \\ & & c_{33} & c_{34} & c_{35} & c_{36} \\ & & & c_{44} & c_{45} & c_{46} \\ & \text{sym.} & & & c_{55} & c_{56} \\ & & & & & c_{66} \end{bmatrix} \begin{bmatrix}\varepsilon_{11}\\ \varepsilon_{22}\\ \varepsilon_{33}\\ \varepsilon_{23}\\ \varepsilon_{13}\\ \varepsilon_{12}\end{bmatrix} \tag{2.4}$$

where $c_{mn} = C_{ijkl}$ where $\{ij\} \to m$ and $\{kl\} \to n$ according to Voigt notation which maps the index pairs of a tensor into a single index: $\{11\} \to 1, \{22\} \to 2, \{33\} \to 3, \{23\} \to 4, \{31\} \to 5, \{12\} \to 6$.

The inverse of this gives the compliance tensor (S_{ijkl}), which expresses strain in terms of stress:

$$\varepsilon_{ij} = S_{ijkl}\sigma_{kl}, \tag{2.5}$$

Represented in Voigt notation gives:

$$\begin{bmatrix}\varepsilon_{11}\\ \varepsilon_{22}\\ \varepsilon_{33}\\ \varepsilon_{23}\\ \varepsilon_{13}\\ \varepsilon_{12}\end{bmatrix} = \begin{bmatrix} s_{11} & s_{12} & s_{13} & s_{14} & s_{15} & s_{16} \\ & s_{22} & s_{23} & s_{24} & s_{25} & s_{26} \\ & & s_{33} & s_{34} & s_{35} & s_{36} \\ & & & s_{44} & s_{45} & s_{46} \\ & \text{sym.} & & & s_{55} & s_{56} \\ & & & & & s_{66} \end{bmatrix} \begin{bmatrix}\sigma_{11}\\ \sigma_{22}\\ \sigma_{33}\\ \sigma_{23}\\ \sigma_{13}\\ \sigma_{12}\end{bmatrix} \tag{2.6}$$

where $s_{mn} = S_{ijkl}$ where $\{ij\} \rightarrow m$ and $\{kl\} \rightarrow n$ according to Voigt notation. Both the elasticity and compliance matrices have 21 independent elastic constants for the most generalized case.

2.2.2.2 Isotropic case

An isotropic elastic has no mechanical directional dependence. Therefore, the elasticity matrix can be simplified using these material symmetries. The 21 independent constants can be reduced to two elastic constants:

$$\begin{bmatrix}\sigma_{11}\\ \sigma_{22}\\ \sigma_{33}\\ \sigma_{23}\\ \sigma_{13}\\ \sigma_{12}\end{bmatrix} = \begin{bmatrix} c_{11} & c_{12} & c_{12} & 0 & 0 & 0 \\ & c_{11} & c_{12} & 0 & 0 & 0 \\ & & c_{11} & 0 & 0 & 0 \\ & & & c_{11}-c_{12} & 0 & 0 \\ & \text{sym.} & & & c_{11}-c_{12} & 0 \\ & & & & & c_{11}-c_{12} \end{bmatrix} \begin{bmatrix}\varepsilon_{11}\\ \varepsilon_{22}\\ \varepsilon_{33}\\ \varepsilon_{23}\\ \varepsilon_{13}\\ \varepsilon_{12}\end{bmatrix} \tag{2.7}$$

Equation 2.4 can be written in terms of the Lamé constants, λ and μ, or the engineering constants Young's modulus (E) and Poisson's ratio (ν) as:

$$\begin{bmatrix}\sigma_{11}\\ \sigma_{22}\\ \sigma_{33}\\ \sigma_{23}\\ \sigma_{13}\\ \sigma_{12}\end{bmatrix} = \begin{bmatrix}\lambda+2\mu & \lambda & \lambda & 0 & 0 & 0\\ & \lambda+2\mu & \lambda & 0 & 0 & 0\\ & & \lambda+2\mu & 0 & 0 & 0\\ & & & 2\mu & 0 & 0\\ & \text{sym.} & & & 2\mu & 0\\ & & & & & 2\mu\end{bmatrix}\begin{bmatrix}\varepsilon_{11}\\ \varepsilon_{22}\\ \varepsilon_{33}\\ \varepsilon_{23}\\ \varepsilon_{13}\\ \varepsilon_{12}\end{bmatrix} \tag{2.8}$$

where

$$\lambda = \frac{E\nu}{(1+\nu)(1-2\nu)}, \mu = \frac{E}{2(1+\nu)} \tag{2.9}$$

The compliance matrix for an isotropic material is

$$\begin{bmatrix}\varepsilon_{11}\\ \varepsilon_{22}\\ \varepsilon_{33}\\ \varepsilon_{23}\\ \varepsilon_{13}\\ \varepsilon_{12}\end{bmatrix} = \begin{bmatrix}\frac{\lambda+\mu}{\mu(3\lambda+2\mu)} & \frac{\lambda+\mu}{\mu(3\lambda+2\mu)}\frac{-\lambda}{2(\lambda+\mu)} & \frac{\lambda+\mu}{\mu(3\lambda+2\mu)}\frac{-\lambda}{2(\lambda+\mu)} & 0 & 0 & 0\\ & \frac{\lambda+\mu}{\mu(3\lambda+2\mu)} & \frac{\lambda+\mu}{\mu(3\lambda+2\mu)}\frac{-\lambda}{2(\lambda+\mu)} & 0 & 0 & 0\\ & & \frac{\lambda+\mu}{\mu(3\lambda+2\mu)} & 0 & 0 & 0\\ & & & \frac{(\lambda+\mu)(1+\nu)}{\mu(3\lambda+2\mu)} & 0 & 0\\ & \text{sym.} & & & \frac{(\lambda+\mu)(1+\nu)}{\mu(3\lambda+2\mu)} & 0\\ & & & & & \frac{(\lambda+\mu)(1+\nu)}{\mu(3\lambda+2\mu)}\end{bmatrix}\begin{bmatrix}\sigma_{11}\\ \sigma_{22}\\ \sigma_{33}\\ \sigma_{23}\\ \sigma_{13}\\ \sigma_{12}\end{bmatrix} \tag{2.10}$$

which simplifies to

$$\begin{bmatrix}\varepsilon_{11}\\ \varepsilon_{22}\\ \varepsilon_{33}\\ \varepsilon_{23}\\ \varepsilon_{13}\\ \varepsilon_{12}\end{bmatrix} = \begin{bmatrix}\frac{1}{E} & -\frac{\nu}{E} & -\frac{\nu}{E} & 0 & 0 & 0\\ & \frac{1}{E} & -\frac{\nu}{E} & 0 & 0 & 0\\ & & \frac{1}{E} & 0 & 0 & 0\\ & & & \frac{1}{2\mu} & 0 & 0\\ & \text{sym.} & & & \frac{1}{2\mu} & 0\\ & & & & & \frac{1}{2\mu}\end{bmatrix}\begin{bmatrix}\sigma_{11}\\ \sigma_{22}\\ \sigma_{33}\\ \sigma_{23}\\ \sigma_{13}\\ \sigma_{12}\end{bmatrix} \tag{2.11}$$

2.2.2.3 Transversely Isotropic case

The simplest anisotropic material is a transversely isotropic (TI) material model. A TI material has one fiber direction but is isotropic in the plane orthogonal to the fiber direction. Figure 2.1 shows an example of a transversely isotropic cube, where fibers are along the *x*-axis and the plane of isotropy is in the *y*-*z* plane. This material is defined by the unit vector, $\boldsymbol{a}$, which represents the fiber direction.

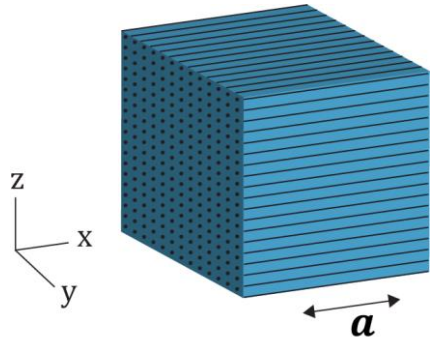

Figure 2.1: Transversely isotropic cube with fiber direction ($\boldsymbol{a}$) along x-axis.

This model assumes linear elasticity and is therefore only valid for small deformations that remain in the elastic region. It is a time independent model, so it does not take viscoelasticity into account.

For a linear, elastic TI model, the stiffness matrix can be written as

$$\begin{bmatrix}\sigma_{11}\\ \sigma_{22}\\ \sigma_{33}\\ \sigma_{23}\\ \sigma_{13}\\ \sigma_{12}\end{bmatrix} = \begin{bmatrix} c_{11} & c_{12} & c_{13} & 0 & 0 & 0 \\ & c_{22} & c_{23} & 0 & 0 & 0 \\ & & c_{33} & 0 & 0 & 0 \\ & & & c_{44} & 0 & 0 \\ & \text{sym.} & & & c_{55} & 0 \\ & & & & & c_{66} \end{bmatrix} \begin{bmatrix}\varepsilon_{11}\\ \varepsilon_{22}\\ \varepsilon_{33}\\ \varepsilon_{23}\\ \varepsilon_{13}\\ \varepsilon_{12}\end{bmatrix} \tag{2.12}$$

where $\boldsymbol{a} = \boldsymbol{e_1} = [1\ 0\ 0]^T$ is the fiber direction (Figure 2.1). A nearly incompressible TI (NITI) material can be characterized by only four parameters: minimum shear modulus (μ), shear

anisotropy (ϕ), tensile anisotropy (ζ), and bulk modulus (κ) [58]. The components of the stiffness matrix for this case are given by

$$c_{11} = \kappa + \frac{4}{3}\mu\left(1 + \frac{4}{3}\zeta\right) \tag{2.13}$$

$$c_{22} = c_{33} = \kappa + \frac{4}{3}\mu\left(1 + \frac{1}{3}\zeta\right) \tag{2.14}$$

$$c_{12} = c_{13} = \kappa - \frac{2}{3}\mu\left(1 + \frac{4}{3}\zeta\right) \tag{2.15}$$

$$c_{23} = \kappa - \frac{2}{3}\mu\left(1 - \frac{2}{3}\zeta\right) \tag{2.16}$$

$$c_{44} = 2\mu \tag{2.17}$$

$$c_{55} = c_{66} = 2\mu(1 + \phi) \tag{2.18}$$

The compliance matrix for a TI material can also be written in terms of shear modulus, shear anisotropy, tensile anisotropy, and bulk modulus by

$$\begin{bmatrix} \varepsilon_{11} \\ \varepsilon_{22} \\ \varepsilon_{33} \\ \varepsilon_{23} \\ \varepsilon_{13} \\ \varepsilon_{12} \end{bmatrix} = \begin{bmatrix} \frac{1}{\mu(4\zeta+3)} + \frac{1}{9\kappa} & \frac{-1}{2\mu(4\zeta+3)} + \frac{1}{9\kappa} & \frac{-1}{2\mu(4\zeta+3)} + \frac{1}{9\kappa} & 0 & 0 & 0 \\ \frac{-1}{2\mu(4\zeta+3)} + \frac{1}{9\kappa} & \frac{1+\zeta}{\mu(4\zeta+3)} + \frac{1}{9\kappa} & \frac{-(1+2\zeta)}{2\mu(4\zeta+3)} + \frac{1}{9\kappa} & 0 & 0 & 0 \\ \frac{-1}{2\mu(4\zeta+3)} + \frac{1}{9\kappa} & \frac{-(1+2\zeta)}{2\mu(4\zeta+3)} + \frac{1}{9\kappa} & \frac{1+\zeta}{\mu(4\zeta+3)} + \frac{1}{9\kappa} & 0 & 0 & 0 \\ 0 & 0 & 0 & \frac{1}{2\mu} & 0 & 0 \\ 0 & 0 & 0 & 0 & \frac{1}{2\mu(1+\phi)} & 0 \\ 0 & 0 & 0 & 0 & 0 & \frac{1}{2\mu(1+\phi)} \end{bmatrix} \begin{bmatrix} \sigma_{11} \\ \sigma_{22} \\ \sigma_{33} \\ \sigma_{23} \\ \sigma_{13} \\ \sigma_{12} \end{bmatrix} \tag{2.19}$$

In a near-incompressible material the bulk modulus $\kappa \to \infty$, so the effect of the bulk modulus on the compliance tensor becomes negligible. This means the material is most likely to deform in

shear when loaded [9, 31]. The compliance matrix can then be simplified so that it only depends on three parameters: μ, ϕ, and ζ.

$$\begin{bmatrix}\varepsilon_{11}\\ \varepsilon_{22}\\ \varepsilon_{33}\\ \varepsilon_{23}\\ \varepsilon_{13}\\ \varepsilon_{12}\end{bmatrix} = \begin{bmatrix} \frac{1}{\mu(4\zeta+3)} & \frac{-1}{2\mu(4\zeta+3)} & \frac{-1}{2\mu(4\zeta+3)} & 0 & 0 & 0 \\ \frac{-1}{2\mu(4\zeta+3)} & \frac{1+\zeta}{\mu(4\zeta+3)} & \frac{-(1+2\zeta)}{2\mu(4\zeta+3)} & 0 & 0 & 0 \\ \frac{-1}{2\mu(4\zeta+3)} & \frac{-(1+2\zeta)}{2\mu(4\zeta+3)} & \frac{1+\zeta}{\mu(4\zeta+3)} & 0 & 0 & 0 \\ 0 & 0 & 0 & \frac{1}{2\mu} & 0 & 0 \\ 0 & 0 & 0 & 0 & \frac{1}{2\mu(1+\phi)} & 0 \\ 0 & 0 & 0 & 0 & 0 & \frac{1}{2\mu(1+\phi)} \end{bmatrix} \begin{bmatrix}\sigma_{11}\\ \sigma_{22}\\ \sigma_{33}\\ \sigma_{23}\\ \sigma_{13}\\ \sigma_{12}\end{bmatrix} \tag{2.20}$$

The compliance matrix of a general TI material is classically written in terms of two Young's moduli (E_1 & E_2), two shear moduli (μ_1 & μ_2), and three Poisson's ratios ($\upsilon_{12}, \upsilon_{21}, \& \upsilon_2$) by

$$\begin{bmatrix}\varepsilon_{11}\\ \varepsilon_{22}\\ \varepsilon_{33}\\ \varepsilon_{23}\\ \varepsilon_{13}\\ \varepsilon_{12}\end{bmatrix} = \begin{bmatrix} \frac{1}{E_1} & -\frac{\upsilon_{21}}{E_2} & -\frac{\upsilon_{21}}{E_2} & 0 & 0 & 0 \\ -\frac{\upsilon_{12}}{E_1} & \frac{1}{E_2} & -\frac{\upsilon_2}{E_2} & 0 & 0 & 0 \\ -\frac{\upsilon_{12}}{E_1} & -\frac{\upsilon_2}{E_2} & \frac{1}{E_2} & 0 & 0 & 0 \\ 0 & 0 & 0 & \frac{1}{2\mu_2} & 0 & 0 \\ 0 & 0 & 0 & 0 & \frac{1}{2\mu_1} & 0 \\ 0 & 0 & 0 & 0 & 0 & \frac{1}{2\mu_1} \end{bmatrix} \begin{bmatrix}\sigma_{11}\\ \sigma_{22}\\ \sigma_{33}\\ \sigma_{23}\\ \sigma_{13}\\ \sigma_{12}\end{bmatrix} \tag{2.21}$$

The Young's moduli describe the stresses from the uniaxial stretch parallel (E_1) and perpendicular (E_2) to the fiber direction. The two shear moduli govern the shear stresses during shear in the planes parallel to (μ_1) and perpendicular to (μ_2) the fiber direction. The NITI material parameters, baseline shear modulus (μ), shear anisotropy (ϕ), tensile anisotropy (ζ), can thus be defined in terms of the Young's moduli (E_1 & E_2), two shear moduli (μ_1 & μ_2) as:

$$\mu = \mu_2, \tag{2.22}$$

$$\phi = \frac{\mu_1}{\mu_2} - 1, \tag{2.23}$$

$$\zeta = \frac{E_1}{E_2} - 1. \tag{2.24}$$

The Poisson's ratios v_{ij} describe the strain in the j-direction from the stretch in the i-direction. For the perfectly incompressible (ITI) material: $v_{12} = 1/2$, $v_{21} = \frac{E_2}{E_1} v_{12}$, and $v_2 = 1 - v_{21}$.

2.2.3 Viscoelasticity

Most biological materials exhibit viscoelastic behavior, which means they display mechanical properties associated with both elastic solids and viscous fluids. In viscoelastic materials, the relationship between stress and strain is time-dependent. The response of a viscoelastic material harmonic loading can be described according to the "correspondence principle" [90] simply by replacing the real (elastic) moduli (μ) with a complex (viscoelastic) moduli ($\mu^* = \mu' + i\mu''$), in which the real part captures the elastic behavior and the imaginary part captures the viscous effects of the material. These complex moduli are the ratios of the Fourier coefficients of stress and strain components [90]. In an isotropic material the real part of the shear modulus is called the storage modulus and the imaginary part the loss modulus. In anisotropic materials, it is common to assume anisotropic elastic moduli, μ, and an isotropic loss factor, η, so that the imaginary part of each viscoelastic parameter is the real part multiplied by η.

2.2.4 Wave Propagation

To investigate how plane waves travel in a nearly incompressible transversely isotropic (NITI) material, a harmonic displacement field solution is assumed (Figure 2.2)

$$\boldsymbol{u}(\boldsymbol{x},\boldsymbol{t}) = u_0\boldsymbol{m}\exp[i(k\boldsymbol{n}\cdot\boldsymbol{x}-\omega t)] = u_0\boldsymbol{m}\exp[ik(\boldsymbol{n}\cdot\boldsymbol{x}-ct)] \tag{2.25}$$

where $\boldsymbol{u}$ is the shear wave displacement, t is time, u_0 is the amplitude of displacement, $\boldsymbol{m}$ is the polarization of the displacement, k is the wave number, $\boldsymbol{n}$ is the propagation direction, ω is the excitation frequency, and c is the wave speed.

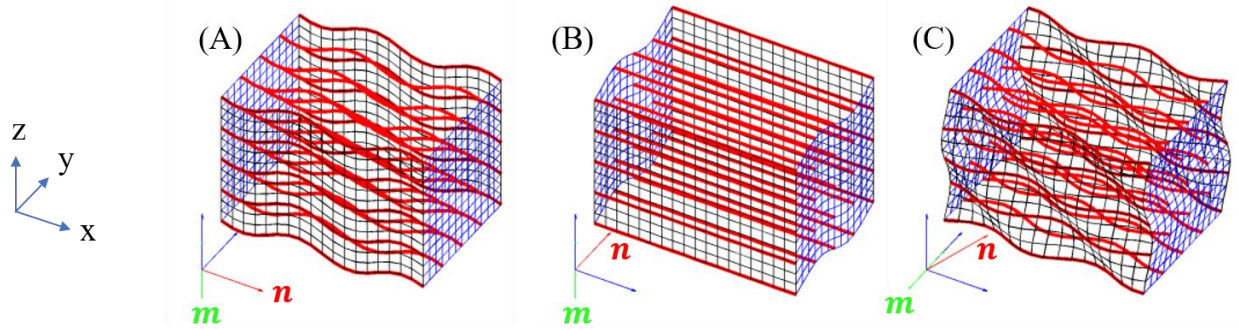

Figure 2.2: Shear waves propagating through a transversely isotropic material with fiber direction along the x-axis, $\boldsymbol{a} = [1\ 0\ 0]$; [9, 31]. Propagation direction ($\boldsymbol{n}$) is shown in red; polarization direction ($\boldsymbol{m}$) is shown in green. (A) Shear wave propagating along the fiber direction: $\boldsymbol{n} = [1\ 0\ 0]$; $\boldsymbol{m} = [0\ 0\ 1]$; (B) Shear wave propagating transverse to fibers in the plane of isotropy: $\boldsymbol{n} = [0\ 1\ 0]$; $\boldsymbol{m} = [0\ 0\ 1]$; (C) Shear wave propagating in an arbitrary direction relative to the fiber axis: $\boldsymbol{n} = [n_1\ n_2\ n_3]$; $\boldsymbol{m} = [m_1\ m_2\ m_3]$; [58].

This equation is substituted into the equation of motion in general tensor notation

$$\text{div}\,\boldsymbol{\sigma} = \rho \frac{\partial^2 \boldsymbol{u}}{\partial t^2} \tag{2.26}$$

where ρ is the density. Substitute equation 2.25 into equation 2.26 and apply the linear elastic constitutive law, $\boldsymbol{\sigma} = C\boldsymbol{\varepsilon}$, to produce

$$C_{ijkl} n_i n_k m_l = \rho c^2 m_j, \quad j = 1,2,3 \tag{2.27}$$

If we define the acoustic tensor as

$$Q_{jl} = C_{ijkl} n_i n_k \tag{2.28}$$

we obtain the eigenvalue problem

$$\boldsymbol{Q}(\boldsymbol{n}) \cdot \boldsymbol{m} = \rho c^2 \boldsymbol{m} \tag{2.29}$$

The solution to this eigenvalue problem is three eigenvalues $\lambda = \rho c^2$ and eigenvectors $\boldsymbol{m}$.

By substituting in the above elastic tensor terms and defining the 1-2 plane so that $\boldsymbol{n} = cos\theta\boldsymbol{e_1} + sin\theta\boldsymbol{e_2}$, the acoustic tensor becomes

$$\boldsymbol{Q} = \mu\begin{bmatrix} (1+\phi)sin(\theta)^2 + \left(\frac{\kappa}{\mu}+\frac{4}{3}+16\zeta/9\right)cos(\theta)^2 & \left(\frac{1}{3}+\frac{\kappa}{\mu}+\phi-8\zeta/9\right)cos(\theta)\,sin(\theta) & 0 \\ \left(\frac{1}{3}+\frac{\kappa}{\mu}+\phi-8\zeta/9\right)cos(\theta)\,sin(\theta) & (1+\phi)\,cos(\theta)^2 + \left(\frac{\kappa}{\mu}+\frac{4}{3}+16\zeta/9\right)sin(\theta)^2 & 0 \\ 0 & 0 & (1+\phi)\,cos(\theta)^2 + sin(\theta)^2 \end{bmatrix} \quad (2.30)$$

With this form and a given set of material properties, the eigenvalue problem can be solved numerically. For an NITI material, where $\kappa \rightarrow \infty$, the eigenvalues are

$$\lambda_1 = \rho c_s^2 = \mu(1 + \phi\cos^2\theta) \quad (2.31)$$

$$\lambda_2 = \rho c_f^2 = \mu(1 + \phi\, cos^2\, 2\theta + \zeta\, sin^2\, 2\theta) \quad (2.32)$$

$$\lambda_3 = \rho c_p^2 \rightarrow \infty \quad (2.33)$$

where c_s is referred to as the "slow" (or pure) shear wave speed, c_f is referred to as the "fast" (or quasi) shear wave speed, c_p is the pressure (or longitudinal) wave speed, ρ is the material density, θ is the angle between the propagation direction and the fiber direction, and μ, ϕ, ζ are the material properties (baseline shear modulus, μ, shear anisotropy, ϕ, and tensile anisotropy, ζ).

The eigenvectors are

$$\boldsymbol{v_1} = [0\ \ 0\ \ 1]^T \quad (2.34)$$

$$\boldsymbol{v_2} = [-sin\theta\ \ cos\theta\ \ 0]^T \quad (2.35)$$

$$\boldsymbol{v_3} = [cos\theta\ \ sin\theta\ \ 0]^T \quad (2.36)$$

The fiber direction ($\boldsymbol{a}$) and propagation direction ($\boldsymbol{n}$) are often in arbitrary directions. The slow and fast shear wave polarizations ($\boldsymbol{m_s}$ and $\boldsymbol{m_f}$, respectively) are defined as (Figure 2.3)

$$\boldsymbol{v_1} = -\boldsymbol{m_s} = -\frac{\boldsymbol{n}\times\boldsymbol{a}}{|\boldsymbol{n}\times\boldsymbol{a}|} \tag{2.37}$$

$$\boldsymbol{v_2} = \boldsymbol{m_f} = \mathbf{n} \times \boldsymbol{m_s} \tag{2.38}$$

$$\boldsymbol{v_3} = \mathbf{n} \tag{2.39}$$

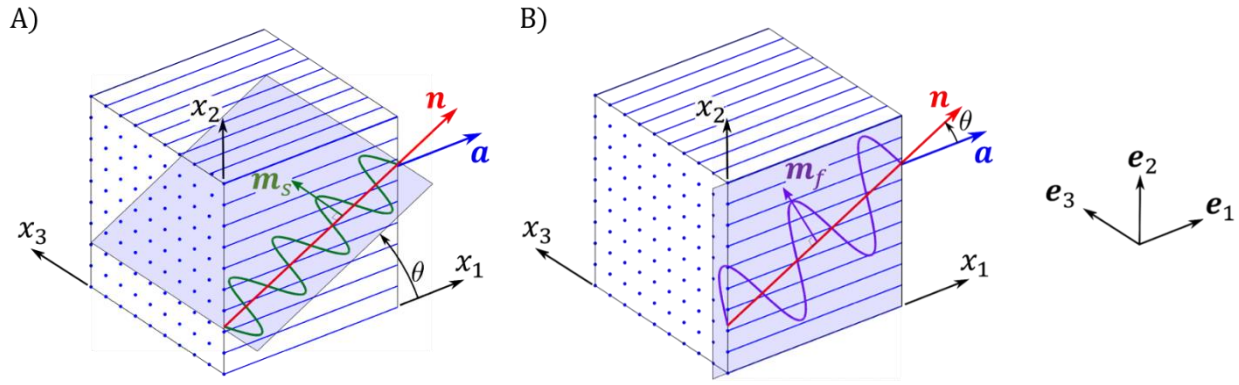

Figure 2.3: The propagation direction ($\boldsymbol{n}$) and polarization directions ($\boldsymbol{m_s}$ and $\boldsymbol{m_f}$) of slow (A) and fast (B) shear waves, respectively, in an incompressible, transversely isotropic, elastic material with a fiber direction ($\boldsymbol{a}$) along the x-axis. Reprinted from [31].

2.3 Imaging Methods

2.3.1 MRE

Magnetic resonance elastography (MRE) is a non-invasive imaging technique for measuring the mechanical properties of soft tissue [51]. In MRE, shear waves are induced in tissue by harmonic mechanical actuation; these waves are then imaged with a modified MR imaging sequence that includes harmonic, motion-sensitizing gradients (Figure 2.4). The material properties of the tissue can be calculated using an inversion method to estimate parameters that are consistent with observed wave fields (Figure 2.5).

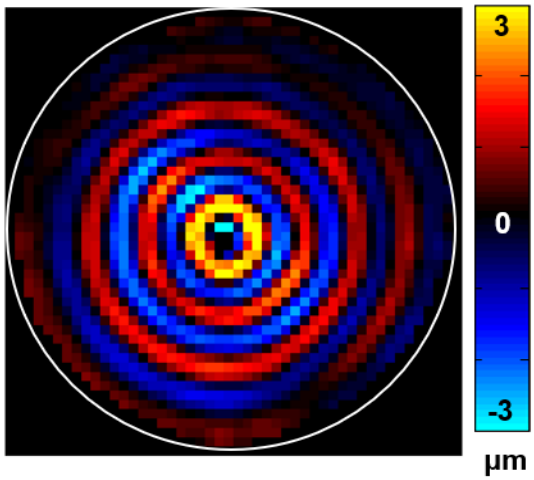

Figure 2.4: Experimental MRE displacement data acquired in isotropic gelatin/glycerol at 200 Hz mechanical actuation from a thin rod embedded in the center of the sample [1].

There are many ways to induce harmonic shear waves in a material. Typical MRE methods include using actuators either on the surface of a tissue or body part [23, 32-34] or a thin rod inside the tissue [30] to create shear waves in the tissue.

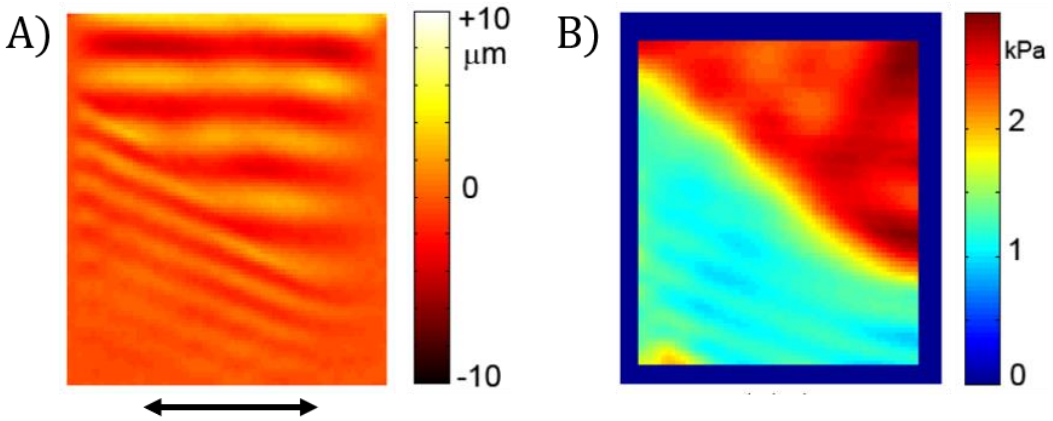

Figure 2.5: (A) Image of shear waves in a heterogeneous gelatin cube with two different shear moduli. Waves were induced by horizontal oscillatory loading of the lower surface. (B) Shear moduli were estimated by fitting the displacement field to equations of wave propagation in locally homogeneous, isotropic, linear elastic media. Longer wavelength shear waves correspond to stiffer materials. (Images courtesy P.V. Bayly).

The shear wave displacements from harmonic actuation are measured using MRE imaging sequences with motion-encoding gradients. These gradients oscillate at the same frequency as the actuation and produce phase contrast images along the period that are proportional to the displacement of the tissue [51, 91]. 2D spiral sequences (Figure 2.6) are run using motion encoding gradients in three orthogonal direction to completely measure the 3D motion field.

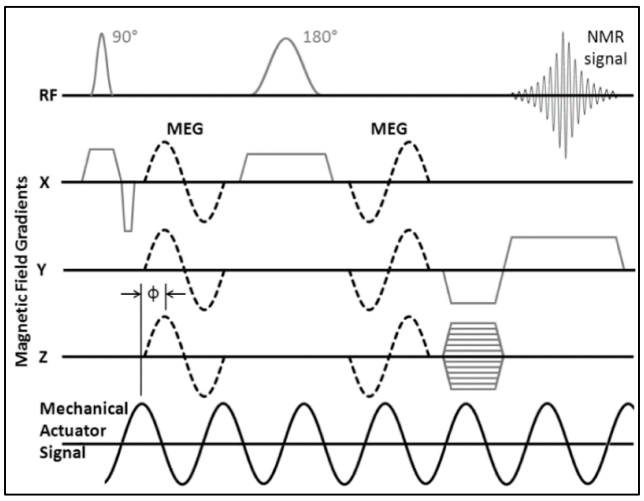

Figure 2.6: Example pulse sequence diagram for spiral 2D MRE sequence. Motion encoding gradients (X, Y, Z) are applied separately to visualize the motion in 3 orthogonal directions. The gradient is at the same frequency as the actuation (Mechanical Actuator Signal). Reprinted from [21]

During MRE imaging sequence, motion-induced phase ($\boldsymbol{\varphi}$) is obtained for every voxel, which is proportional to the oscillating displacement ($\boldsymbol{u}$) [51, 56]. The position of a material element with a nuclear spin, also known as spin packet, in a 3D sample can be defined as

$$\boldsymbol{x} = \boldsymbol{X} + \boldsymbol{u} \tag{2.40}$$

where $\boldsymbol{X}$ is the initial position of the material element. The harmonic displacement of the element is defined as

$$\boldsymbol{u} = \boldsymbol{u_0}\ \cos(\omega t - \boldsymbol{k}\cdot\boldsymbol{X} + \theta) \tag{2.41}$$

where $\boldsymbol{u_0}$ is the vibration amplitude (m), ω is the vibration frequency (rad/s), $\boldsymbol{k}$ is the spatial frequency vector (rad/m), and θ is the vibration phase (rad). The component of the phase vector for this material element in the direction of the gradient ($\varphi_G(\boldsymbol{X},\theta)$) is

$$\varphi_G(\boldsymbol{X},\theta) = \gamma\int_0^{2\pi N/\omega}(\boldsymbol{G}\cdot\boldsymbol{x})dt = \frac{\gamma\pi N(\boldsymbol{G_0}\cdot\boldsymbol{u_0})}{\omega}\cos(\theta - \boldsymbol{k}\cdot\boldsymbol{X}) \tag{2.42}$$

where γ is the gyro-magnetic ratio of water (rad/s/T), N is the number of motion-encoding gradient cycles for the sequence, and $\boldsymbol{G} = \boldsymbol{G_0}\cos(\omega t)$ is the motion-encoding magnetic field gradient (T/m) [51, 56]. This equation can be simplified to

$$\boldsymbol{u}(\boldsymbol{X},\theta) = C\boldsymbol{\varphi}(\boldsymbol{X},\theta). \tag{2.43}$$

Where C is a proportional constant that relates the MR phase to displacement equal to

$$C_i = \frac{u_{\max,i}}{\varphi_{\max,i}} = \frac{\omega}{\gamma\pi N G_{0,i}}, \tag{2.44}$$

for the i^{th} direction where $G_{o,i}$ is the gradient amplitude in the respective direction.

2.3.2 Inversion: Estimating material properties in MRE

A method of inversion is used to estimate the mechanical properties of a material. Three types of inversion are local frequency estimation (LFE), local direct inversion (LDI), and phase gradient (PG). All methods rely on specific assumptions in their analysis. For a more accurate estimate of mechanical properties, ideally all assumptions for inversion are correct, however that is not often the case.

2.3.2.1 Local frequency estimation

For a shear wave traveling through an infinite isotropic domain, the shear wavelength (λ) is directly related to the material's shear modulus (μ)

$$\lambda = \frac{1}{f}\sqrt{\frac{\mu}{\rho}} \tag{2.45}$$

where f is the frequency of the shear wave and ρ is the material density. This equation can be rearranged to give

$$\mu = \rho(f\lambda)^2, \tag{2.46}$$

In local frequency estimation (LFE), the local spatial frequency of shear wave propagation is estimated by applying a series of spatial filters of radial and directional components [92] (Figure 2.7). The shear wavelength is calculated from the dominant wave number (k) in the imaging domain (L)

$$\lambda = \frac{2\pi}{\boldsymbol{k}}. \tag{2.47}$$

The method assumes the material is isotropic, with only shear waves traveling through an infinite domain. LFE is a robust technique since it uses multi-scale data averaging for the estimation, providing local estimates for isotropic materials that are insensitive to noise [93]. LFE does not approximate material properties well near boundaries.

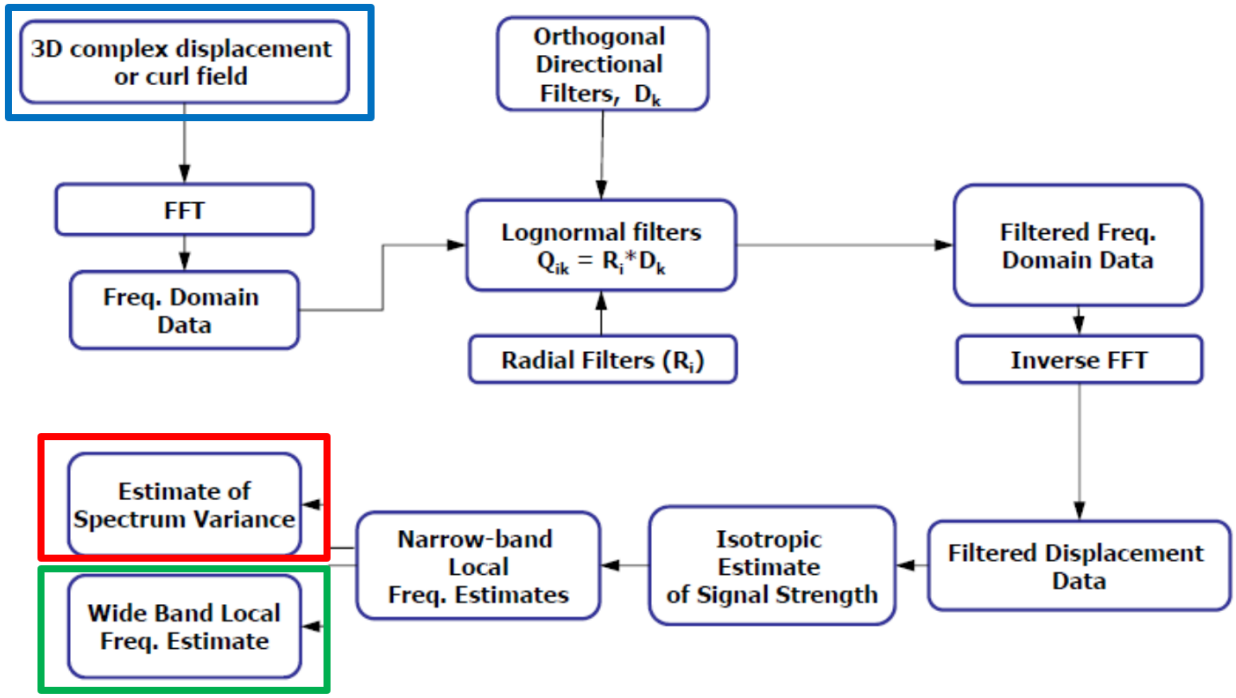

Figure 2.7: Flow chart for LFE method.

2.3.2.2 Local direct inversion

MRE shear wave displacement fields can be fitted to elastic wave equations in local direct inversion (LDI) [1]. LDI estimates the material properties with the assumption that the material is isotropic, linear, locally homogeneous, and viscoelastic.

The shear modulus of the material, μ, is assumed to be the complex shear modulus, μ^*

$$\mu = \mu^*(i\omega) = \mu'(\omega) + i\mu''(\omega), \tag{2.48}$$

where ω is the frequency of the shear wave, μ' is the shear storage modulus (real part of μ^*), and μ'' is the shear loss modulus (imaginary part of μ^*). Using this, the linear, isotropic, locally homogenous, viscoelastic Navier equation can be expressed as

$$(\mu' + i\mu'')\nabla^2 \boldsymbol{U}(\boldsymbol{x}, \omega) = -\rho\omega^2 \boldsymbol{U}(\boldsymbol{x}, \omega), \tag{2.49}$$

where $\boldsymbol{U}(\boldsymbol{x}, \omega)$ is the MRE shear wave displacement field [1]. The inversion is done using a total-least squares fitting method, fitting data within a kernel size, like $5 \times 5 \times 5$ voxels.

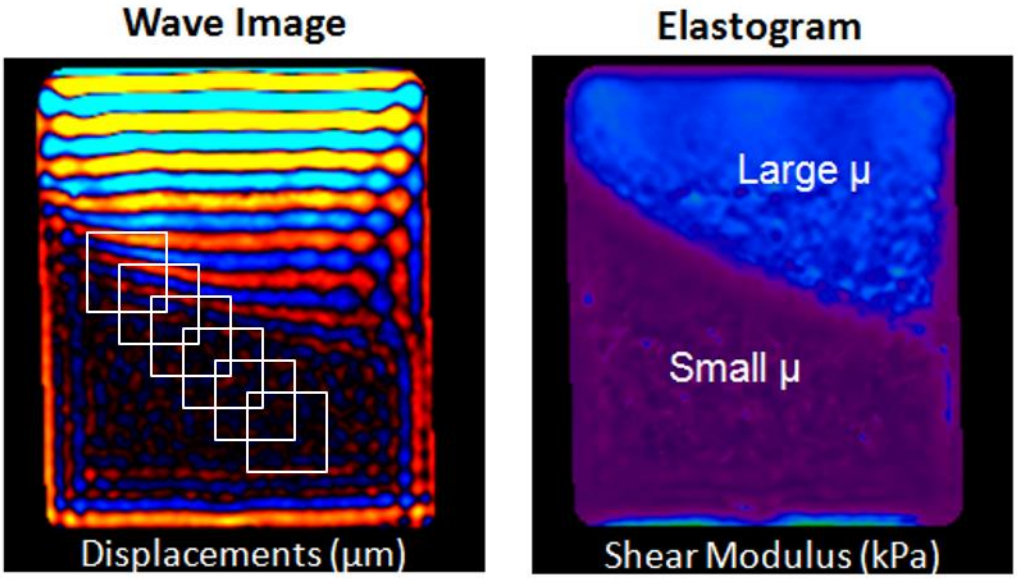

Figure 2.8: Example of LDI. Wave images are analyzed using a total-least squares fitting method, fitting data within a kernel size (white boxes). Shorter wavelengths correspond to a small shear modulus. Longer wavelengths correspond to a large shear modulus. (Figure credit E.H. Clayton)

2.3.2.3 Phase Gradient

Material properties can be calculated from the phase of harmonic shear waves at every voxel [53]. The phase angle of the shear wave (Ψ) can be calculated by taking the angle of any displacement

component (u_j). Phase angle can also be calculated using a component of curl of the displacement (Γ_j).

$$\Psi = \angle u_j \tag{2.50}$$

The wave number ($\boldsymbol{k}$) can then be calculated from the gradient of phase.

$$\boldsymbol{k} = \boldsymbol{\nabla}\Psi \tag{2.51}$$

Wavelength (λ) is proportional to the magnitude of the wave number vector, which is ideally the same as its radial component.

$$\lambda = \frac{2\pi}{|\boldsymbol{k}|} \tag{2.52}$$

Apparent shear modulus is then estimated from wavelength, using the frequency of the actuation (f).

$$\mu = \rho(\lambda f)^2 \tag{2.53}$$

The phase gradient method (PG) is very high resolution, but it is sensitive to noise [53]. This method is only accurate when there is only one simple shear wave, with no reflections [53].

2.3.3 Anisotropic Parameter Estimation

Anisotropic material properties can be estimated using slow and fast shear waves for an elastic, nearly incompressible, transversely isotropic (NITI) material. As shown in Section 2.2.2.3, a NITI material can be described by the three independent parameters: shear modulus (μ), shear

anisotropy (ϕ), and tensile anisotropy (ζ). These three parameters can be estimated using shear wave speed, propagation direction, polarization direction, and fiber direction. Using displacement data from the phase measurements, slow and fast shear waves are isolated by directional filtering with respect to the propagation and polarization directions [30, 31], defined in equations 2.37 and 2.38.

Slow shear waves do not stretch the fibers in the ITI material. Therefore, the slow shear wave speed (c_s) depends only on the baseline shear modulus (μ), density (ρ), shear anisotropy (ϕ) and the angle between the fiber direction and the propagation direction (θ).

$$\rho c_s^2 = \mu(1 + \phi \cos^2 \theta) \tag{2.54}$$

Fast shear waves stretch the fibers in the material, so the fast shear wave speed (c_f) is also dependent on tensile anisotropy (ζ).

$$\rho c_f^2 = \mu(1 + \phi \cos^2 2\theta + \zeta \sin^2 2\theta) \tag{2.55a}$$

$$\rho c_f^2 = \mu(1 + \phi) + (\zeta - \phi) \sin^2 2\theta \tag{2.55b}$$

Multiple shear wave speeds (c_s , c_f) can be measured using a variety of actuation frequencies. To define these three unknown material parameters, different angles of propagation (θ) and multiple shear wave speeds (c_s , c_f) provide independent sets of equations:

$$\begin{bmatrix} 1 & \cos^2 \theta_1 & 0 \\ \vdots & \vdots & \vdots \\ 1 & \cos^2 \theta_n & 0 \\ 1 & \cos^2 2\theta_{n+1} & \sin^2 2\theta_{n+1} \\ \vdots & \vdots & \vdots \\ 1 & \cos^2 2\theta_{n+m} & \sin^2 2\theta_{n+m} \end{bmatrix} \begin{bmatrix} \mu \\ \mu\phi \\ \mu\zeta \end{bmatrix} = \rho \begin{bmatrix} c_{1,1}^2 \\ \vdots \\ c_{1,n}^2 \\ c_{2,n+1}^2 \\ \vdots \\ c_{2,n+m}^2 \end{bmatrix} \tag{2.56}$$

where n is the number of slow shear waves and m is the number of fast shear waves. The system is solved in the least-squares sense to find the material properties $\mu, \phi,$ and ζ.

2.3.4 Directional Filtering

Propagation directions of harmonic wave fields can be estimated using directional filtering [6]. First, the Fourier coefficient, $U(\boldsymbol{X})$, of a scalar component of the wave field is extracted by Fourier transform in time. This coefficient is decomposed into harmonic functions of space, where each voxel has a 3D wavenumber vector. A directional filter is used to eliminate wave components outside a specific range about a vector, $\boldsymbol{n_m}$. This result is then inverse-Fourier transformed to obtain the filtered displacement component $U_m(\boldsymbol{X})$ for waves described by the vector $\boldsymbol{n_m}$. The propagation direction field at each voxel location is estimated by M unit vector directions distributed evenly along the unit sphere

$$\boldsymbol{n}^{(u)}(\boldsymbol{X}) = \sum_{m=1}^{M} \boldsymbol{n}_m |\boldsymbol{U}_m(\boldsymbol{X})| \tag{2.57}$$

An example of a wave field directionally filtered in each of two perpendicular directions is shown in Figure 2.9.

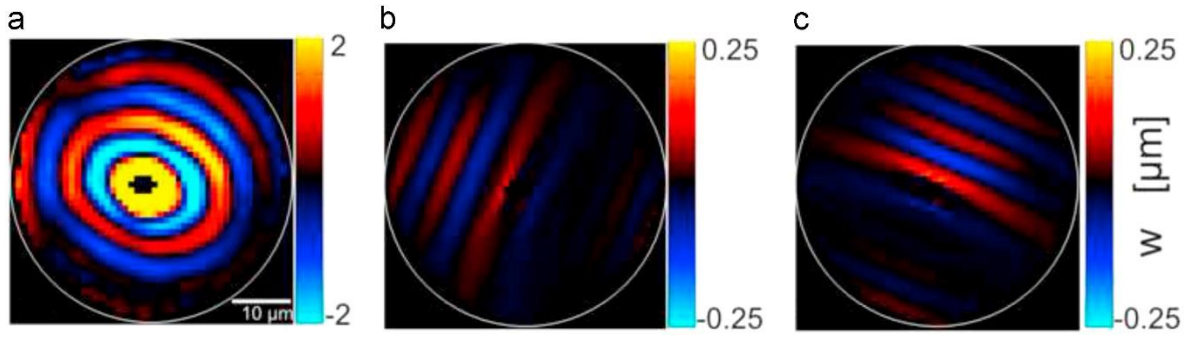

Figure 2.9: Wave propagation in a cylindrically aligned fibrin gel sample at 200 Hz actuation, illustrating analysis by directional filtering. (a) Elliptical waves exhibiting direction dependent propagation with different wave speeds in different directions. (b–c) Displacement field after directional filtering in each of two propagation directions specified by angle, θ, from the dominant fiber direction. (b) θ = 0° and (c) θ = 90°. Figure from [30].

2.3.5 Diffusion tensor imaging

Diffusion tensor imaging (DTI) is a noninvasive MR imaging method used to determine the magnitude and directional dependence of water diffusion in a material. This method can be used to investigate fiber orientation in tissues because diffusion in fibrous tissues is often anisotropic, with water diffusing faster along the fiber axis and slower perpendicular to the fibers [94, 95]. Diffusion-sensitizing magnetic field gradients are applied in a chosen number of directions to estimate the elements of the diffusion tensor for those directions. The diffusion tensor has three eigenvalues and eigenvectors, with the major principal axis corresponding to the direction of the tissue fibers (Figure 2.10).

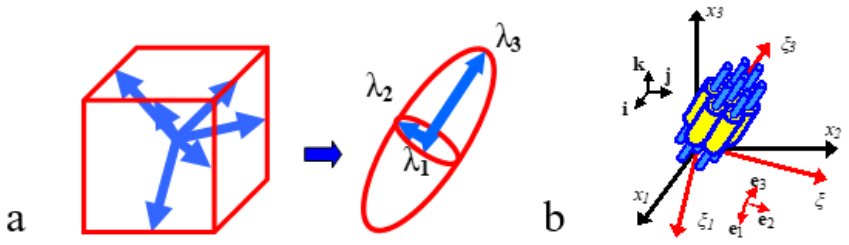

Figure 2.10: (a) Diffusion-sensitizing magnetic field gradients are applied in at least 6 directions to estimate the 6 elements of the diffusion tensor. The tensor has three eigenvalues (diffusivities $\lambda_1,\ \lambda_2,\ \lambda_3$) and associated eigenvectors, The major principal axis corresponds to fiber direction (b).

The degree of anisotropy of diffusion of a tissue is defined by the tissue's fractional anisotropy (FA). FA is a normalized measure of the differences between eigenvalues of the diffusion tensor, defined as

$$FA = \sqrt{\frac{1}{2}}\frac{\sqrt{(\lambda_1-\lambda_2)^2+(\lambda_2-\lambda_3)^2+(\lambda_3-\lambda_1)^2}}{\sqrt{\lambda_1^2+\lambda_2^2+\lambda_3^2}} \tag{2.58}$$

An isotropic material will have a FA close to 0, while a highly anisotropic material will have a FA close to 1.

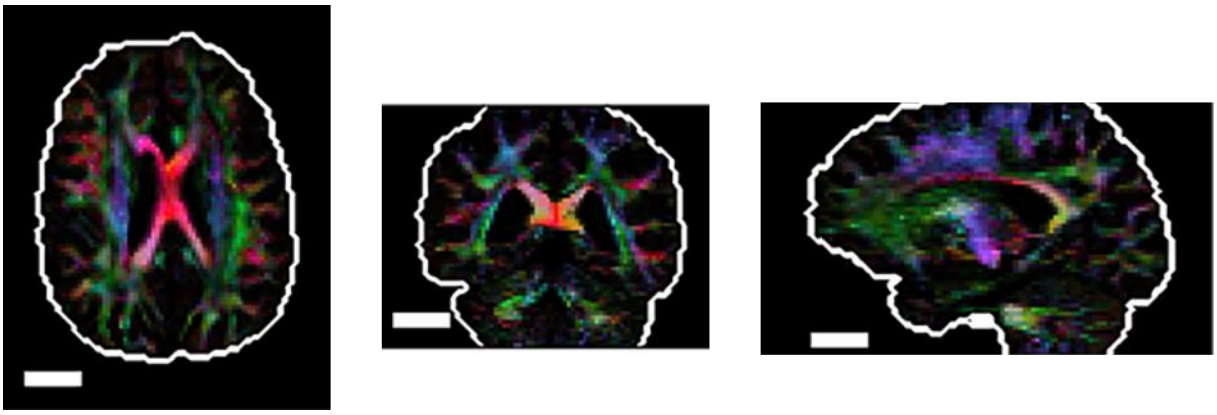

Figure 2.11: Directionally-encoded DTI color map of human brain. Colors indicate direction of maximum diffusivity (red = right-left, green = anterior-posterior, blue = superior-inferior) and brightness indicates strength of anisotropy (FA). Scale bar equals 4 cm in all images. Reprinted from [6].

2.3.6 Acoustic radiation force from focused ultrasound

Ultrasound is a mechanical sound wave with a frequency greater than 20 kHz. The ultrasound waves from a transducer can be noninvasively focused to a focal region of 0.5-3 mm^3 [65, 96] deep inside of a tissue (Figure 2.12). This focal region exerts a force called acoustic radiation force which is defined as

$$F(t) = \frac{2\alpha I(t)}{c} \tag{2.59}$$

where *F(t)* is the volumetric radiation force ($kg/(s^2m^2)$), α is the tissue absorption coefficient (m^{-1}), *I(t)* is the average acoustic intensity (W/m^2), and *c* is the speed of sound in the material (m/s). Acoustic radiation force can be used as a method of remote shear wave actuation for elastography [48, 61].

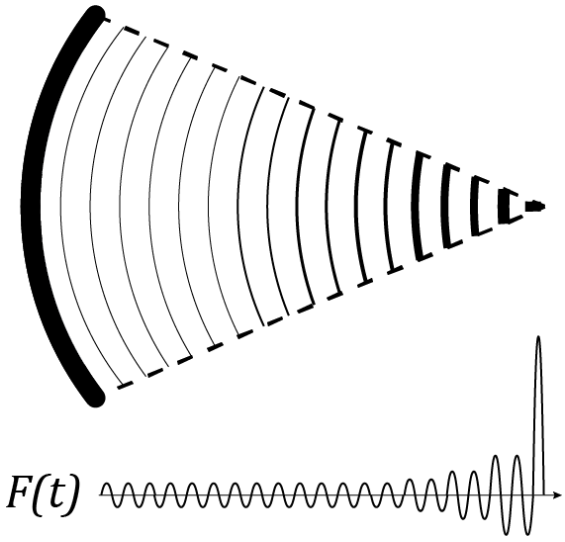

Figure 2.12: Focused ultrasound (FUS) diagram. Focusing of ultrasound waves creates focal region of increased acoustic radiation force (***F***). This force causes motion and creates a shear wave originating at the focus.

An acoustic radiation force causes motion using impulses [50, 52, 62-69] or harmonic modulation [48, 70-74] to create a shear wave in a tissue that originates from the ultrasound focus. Harmonic tissue motion can be induced by amplitude modulation of the FUS beam [96, 97]. The resulting harmonic shear waves are at the frequency of the amplitude modulation. Shear wave displacement and velocity from acoustic radiation force can be imaged by ultrasound [61] or MRI [52, 98, 99].

2.4 Summary

This chapter provides the background and fundamental theory underlying the studies described in Chapters 3-6. The following chapters will build on and apply these concepts to illuminate the mechanical properties of brain tissue.

Chapter 3:Mechanical Properties of Porcine Brain Tissue *In Vivo* and *Ex Vivo* Estimated by MR Elastography[1]

3.1 Overview

The mechanical properties of brain tissue *in vivo* determine the response of the brain to rapid skull acceleration. These properties are thus of great interest to the developers of mathematical models of traumatic brain injury (TBI) or neurosurgical simulations. Animal models provide valuable insight that can improve TBI modeling. Most direct measurements of brain mechanical properties have been performed using samples of brain tissue *ex vivo*. It has been observed that direct estimates of brain mechanical properties depend on the frequency and amplitude of loading, as well as the time post-mortem and condition of the sample. In this study we compare estimates of mechanical properties of the Yucatan mini-pig brain *in vivo* and *ex vivo* using magnetic resonance elastography (MRE) at multiple frequencies. We observe that porcine brain tissue *in vivo* appears stiffer than brain tissue samples *ex vivo*.

3.2 Objective and Significance

The mechanical behavior of the brain remains incompletely characterized [8]. Most mechanical testing of brain tissue is performed using animal tissue *ex vivo* [9-11, 14, 15, 17, 59, 100, 101].

[1] This chapter and its associated appendix is reproduced from [89] C. A. Guertler, R. J. Okamoto, J. L. Schmidt, A. A. Badachhape, C. L. Johnson, and P. V. Bayly, "Mechanical properties of porcine brain tissue in vivo and ex vivo estimated by MR elastography," *Journal of Biomechanics*, vol. 69, pp. 10-18, 2018/03/01/ 2018. Journal of Biomechanics. Author contributions are listed in Chapter 1.
The shear modulus (G) has been changed to μ for this adaptation to be consistent with the rest of the document.

However, *ex vivo* measurements may not necessarily reflect *in vivo* behavior [18, 19]. *In situ* and *in vivo* tests have also been performed using indentation on animals [18, 20] and magnetic resonance elastography (MRE) on both animals and humans [21-25]. Substantial differences have been found between estimates of material parameters, likely due to differences in methodology, frequency range, or time scale.

The relationship between *in vivo* and *ex vivo* properties of brain tissue remains a topic of active research [20]. Bilston et al. hypothesized that brain tissue properties *in vivo* would be stiffer than properties *ex vivo* [102]. Miller et al. performed one *in vivo* indentation test on exposed porcine brain and found stiffness measurements on the same order of magnitude as *in vitro* data [18]. Gefen and Margulies compared mechanical properties in the porcine brain *in vivo* to corresponding properties post-mortem, *in situ* (i.e., after death, but in the intact head), and *ex vivo* (in the extracted brain), also using indentation [20]. These studies found *in vivo* shear moduli stiffer than moduli measured post-mortem on preconditioned tissue (either *in situ* or *ex vivo*). Although these results offer insight into the relationship between *in vivo* and *ex vivo* tissue mechanical properties, the methods have important limitations. Indentation of the intact brain only measures properties near the surface. Also, indentation is sensitive to the detection of contact, and, unless performed at multiple speeds, provides limited information on frequency/strain-rate dependence. Dynamic shear testing of thin tissue samples [9, 58, 59] has been widely used for material characterization. Shear testing assumes flat samples, constant normal force, no slip, and affine deformations; conditions which are rarely satisfied. Furthermore, dynamic shear testing is impractical for *in vivo* tissue.

Still lacking are direct comparisons between dynamic mechanical properties estimated throughout the brain by the same method at similar frequencies and amplitudes, both *in vivo* and *ex vivo*. In this study, we address this need by performing MRE on porcine brain tissue over a range of frequencies, obtaining stiffness estimates both *in vivo* and *ex vivo* within the same tissue volume.

3.3 Methods

In vivo and *ex vivo* anatomical MRI and MRE scans were performed on six Yucatan mini-pigs (age range: 4 to 8 months; weight range: 23 to 50 kg). The experimental protocol was approved by the Washington University in St. Louis Animal Studies Committee, and all studies were supervised by veterinary staff.

3.3.1 *In vivo* Scanning

All scans were performed on a Siemens Prisma® 3T MRI scanner at Washington University in St. Louis. The mini-pigs were anesthetized with Telazol Ketamine Xylazine (TKX). An IV catheter and endotracheal tube were placed prior to scanning. Anesthesia was maintained with isoflurane via endotracheal tube. Temperature, pulse, respiration, and SPO_2 were monitored. Mini-pigs were scanned in either ventral or dorsal recumbency. For dorsal recumbency (4 animals), the animal was positioned with its back on the scanner table (Figure 3.1A), and its head was placed in the base of the Siemens Head/Neck 20 coil. A combination of padding and Velcro™ straps was used to secure the head. For ventral recumbency (2 animals), the animal was positioned with its stomach on the scanner table. Its head was placed under a custom half-dome Plexiglas frame (Figure 3.1C); a combination of padding and Velcro™ straps was used to secure the head. The Siemens 18-

channel Body Matrix Coil was fastened on the Plexiglas frame and MR table using Velcro™ straps.

A custom multi-directional jaw actuator was designed to transmit harmonic motion from a pneumatic driver into the porcine brain while minimizing dissipation from muscle and fat. The actuator was fabricated from two small, empty plastic bottles (Figure 3.1A.1). A custom Delrin (Acetal) holder fit around the tube/bottle neck connections of each bottle. Two holes on each side of the Delrin holder secured an elastic Velcro™ nose strap. Two rubber timing belts encircling each bottle provided traction between the bottles and mini-pig molars (Figure 3.1A and Figure 3.1C). After positioning the mini-pig head in the coil, the custom actuator was placed inside the jaw, with the bottles between the rear molars. The nose strap was tightened around the upper and lower jaws to minimize slippage between the teeth and actuator.

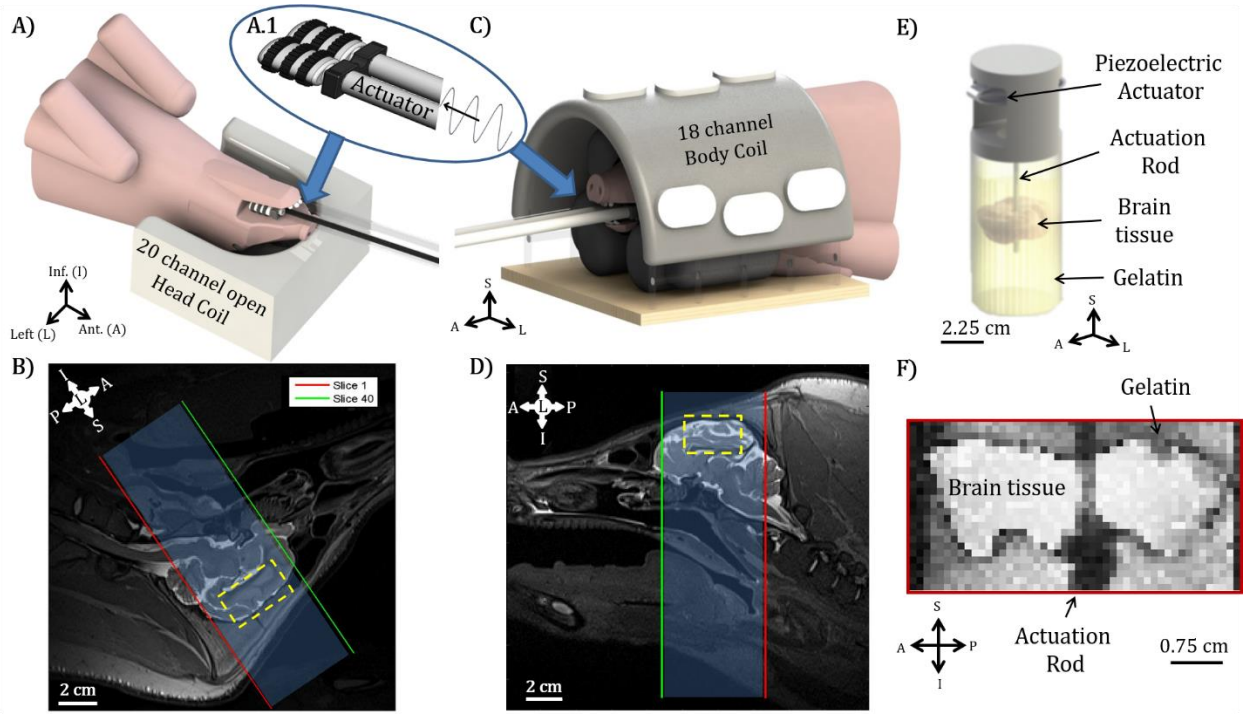

Figure 3.1: (A-D) Experimental set-up for MRE *in vivo*. A custom actuator (A.1) driven by the Resoundant™ system is placed between the back molars of the mini-pig jaw to induce vibrations in the skull and shear waves in brain at 50, 80, 100, and 125 Hz while the mini-pig is positioned in dorsal recumbency or ventral recumbency. (A) Mini-pig scanned in dorsal recumbency with its head placed in the lower part of the Seimens Head/Neck20 coil. Padding and Velcro™ secured the head from excess motion. (B) T2-weighted anatomical image (sagittal view, 0.8 mm^3 voxels) of the mini-pig in dorsal recumbency, with MRE slices highlighted. Yellow rectangle shows the approximate location of the *ex vivo* brain tissue disk. (C) Mini-pig scanned in ventral recumbency with its head placed under a custom, half-dome, Plexiglas frame which supported the Siemens 18-Channel Body Matrix Coil. Padding and Velcro™ secured the head from excess motion. (D) T2-weighted anatomical image (sagittal view, 0.8 mm^3 voxels) of mini-pig in ventral recumbency, with MRE slices highlighted. Yellow rectangle shows approximate location of *ex vivo* brain tissue disk. (E-F) Experimental set-up for MRE *ex vivo*. (E) The cylindrical brain tissue sample is embedded in gelatin and excited by a central actuation rod at 80, 100, 125, 200, and 300 Hz using a piezoelectric actuator. (F) Anatomical image (1 mm^3 voxels) of the *ex vivo* brain tissue sample and gelatin, TE = 60 ms and TR = 1000 ms.

T1-weighted ("MP-RAGE") and T2-weighted MR images were taken at the beginning of every *in vivo* MR scanning session (Figure 3.1B, Figure 3.1D; Figure 3.2A). Image volumes were acquired at 0.8 mm^3 or 0.9 mm^3 isotropic resolution for an in-plane field of view of 205 mm x 205 mm (0.8 mm^3 res) or 230 mm x 230 mm (0.9 mm^3 res). A total of 192 (0.8 mm^3 res) or 96 (0.9 mm^3 res) slices were taken for each scan. Two averages were done for each image set. The anterior-posterior direction of the image volumes was aligned with the genu-splenium axis of the corpus callosum. The total scan time for the two anatomical acquisitions was 21 minutes.

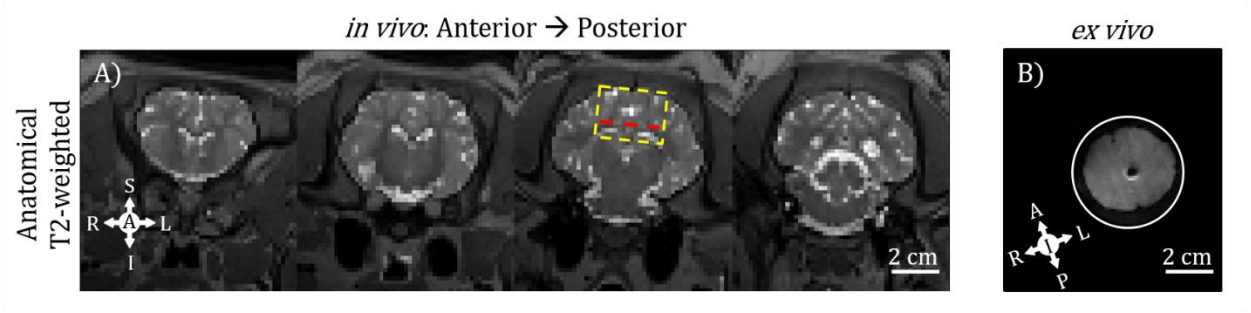

Figure 3.2: Comparison of experimental data from the porcine brain *in vivo* (A) and *ex vivo* (B). (A) T2-weighted MR images of four non-contiguous (7.5 mm spacing) coronal slices of the brain *in vivo* at 1.5 mm resolution. Yellow rectangle shows approximate location of *ex vivo* brain tissue disk. Red line denotes approximate slice location pictured in B. (B) T2-weighted image of *ex vivo* cylindrical sample from the same animal at 1 mm resolution.

For MRE, the skull was vibrated at frequencies of 50 Hz, 80 Hz, 100 Hz, or 125 Hz using a commercially available pneumatic driver (Resoundant™ Rochester, MN) connected to the custom jaw actuator (Table 1). MRE data with 3D displacement components, each encoded by image phase, were acquired with a 2D multi-shot spiral sequence [103] with 1.5 mm isotropic voxels covering a volume of 180 x 180 x 60 mm^3. One vibration frequency was used per acquisition. Multiple sinusoidal motion-encoding cycles of gradient strength 30 mT/m were synchronized with motion to induce phase contrast proportional to displacement (2.45 microns/rad at 50 Hz and 100 Hz, 3.91 microns/rad at 80 Hz, and 3.06 microns/rad at 125 Hz) [56]. Data for each mini-pig were collected over 2-3 scanning sessions using 1-3 actuation frequencies per session.

Table 3.1: Numbers of anatomical and MRE scans performed *in vivo* and *ex vivo* in the 6 mini-pigs.

	T1/T2	**MRE 50 Hz**	**MRE 80 Hz**	**MRE 100 Hz**	**MRE 125 Hz**	**MRE 200 Hz**	**MRE 300 Hz**
In vivo	19	11	2	10	3	-	-
Ex vivo	6	-	1	5	2	6	6

MRE data were phase-unwrapped using open-source software FSL Prelude [104]. Voxels in the MRE volume were fitted to a model of rigid-body displacement and these rigid-body effects were removed to isolate displacements due to wave motion [32].

3.3.2 *Ex vivo* Scanning

Ex vivo scanning of tissue from the same six Yucatan mini-pig brains was performed on an Agilent/Varian DirectDrive 4.7T small-bore animal MRI scanner at room temperature (~21°C). Once all *in vivo* scanning was complete, the mini-pigs (aged 6-9 months) were euthanized by barbiturate overdose. (Note: ages differ from *in vivo* scans because multiple *in vivo* scans were performed on each mini-pig over 2-4 months; 0-2 weeks elapsed between the last *in vivo* scan and the *ex vivo* scan). The brain was immediately extracted following euthanasia and dissected to expose the inferior section of the corpus callosum. A cylindrical sample containing the corpus callosum and superior gray matter, 42 mm in diameter, was extracted from the brain using a cylindrical punch. The sample was embedded in gelatin made with 2:1:1 glycerol, water, and pre-buffered saline (PBS) in a 45 mm cylindrical container [30] (Figure 3.1E). Ex vivo scans began within 2 hours post-mortem.

Ex vivo samples were vibrated at frequencies of 80 Hz, 100 Hz, 125 Hz, 200 Hz, and 300 Hz (Table 1). Shear waves were excited by a central actuation rod of 3 mm diameter that punctured the center of the sample (Figure 3.1E). This rod was driven harmonically by an MR-compatible piezoelectric actuator (APA150M, Cedrat Technologies, Meylan, France). Anatomical images were taken at 1 mm isotropic resolution with a field of view of 48 x 48 x 25 mm^3 (Figure 3.1F, Figure 3.2B). Images were obtained at TE of 60 ms. MRE data were acquired with a modified 2D multi-slice spin-echo sequence with 1 mm isotropic voxels, TR = 1000-1200 ms, and TE = 28-40 ms covering

a volume of 48 x 48 x 25 mm^3 (Figure 3.1F). Sinusoidal motion-encoding gradients (1-3 cycles) of amplitude 100-120 mT/m were synchronized with motion to induce phase contrast proportional to displacement (7.48 microns/rad at 80 Hz (n=1), 100 Hz (n=2), 200 Hz (n=5), and 300 Hz (n=5) and 9.35 microns/rad at 100 Hz (n=3), 125 Hz (n=2), 200 Hz (n=1), and 300 Hz (n=1)). MRE data were phase-unwrapped and rigid-body motion effects were removed using the methods detailed in section 2.1.

3.3.3 Local Direct Inversion

Local direct inversion (LDI) was performed on both the *in vivo* and *ex vivo* MRE displacement fields to estimate the mean complex shear modulus of the mini-pig brain sample at each of the measured frequencies using the viscoelastic analog to the Navier equation [1]:

$$(\mu' + i\mu")\nabla^2 \boldsymbol{U}(x,y,z) = -\rho\omega^2 \boldsymbol{U}(x,y,z)\,, \tag{1}$$

where the complex vector $\boldsymbol{U}(x,y,z)$ contains the Fourier coefficients of the fundamental harmonic of the 3D displacement field, $\boldsymbol{u}(x,y,z,t)$. The parameter μ' is the storage modulus, and $\mu"$ is the loss modulus. This equation assumes that the material is linear, isotropic, and locally homogeneous.

Estimates of storage and loss moduli were obtained for the entire brain *in vivo* and the entire sample of *ex vivo* brain and gelatin. Voxel-wise estimates were averaged over a region of interest (ROI) corresponding to the location and dimensions of the *ex vivo* brain samples. Storage modulus maps were further eroded using a 7x7x7 kernel to remove the possible effects of neighboring gelatin on the averaged storage modulus estimates in the *ex vivo* tissue.

3.4 Results

3.4.1 *In vivo*

Figure 3.3 shows examples of wave displacement, shear strain, and curl for one axial slice of the porcine brain *in vivo*. Although displacement components exist in all three directions, the out-of-plane, anterior-posterior (AP, z) component of motion (u_z) is the dominant component excited by the custom actuator. The displacement amplitude is ~1.5 μm. The curl of the wave field, which isolates the contribution of shear waves, is dominated by the component along the right-left (RL, x) axis, $\Gamma_x = \frac{\partial u_y}{\partial z} - \frac{\partial u_z}{\partial y}$. Shear strain and curl have similar magnitude (~2×10^{-4}); the most prominent component of the strain tensor is $\varepsilon_{zy} = \frac{\partial u_y}{\partial z} + \frac{\partial u_z}{\partial y}$.

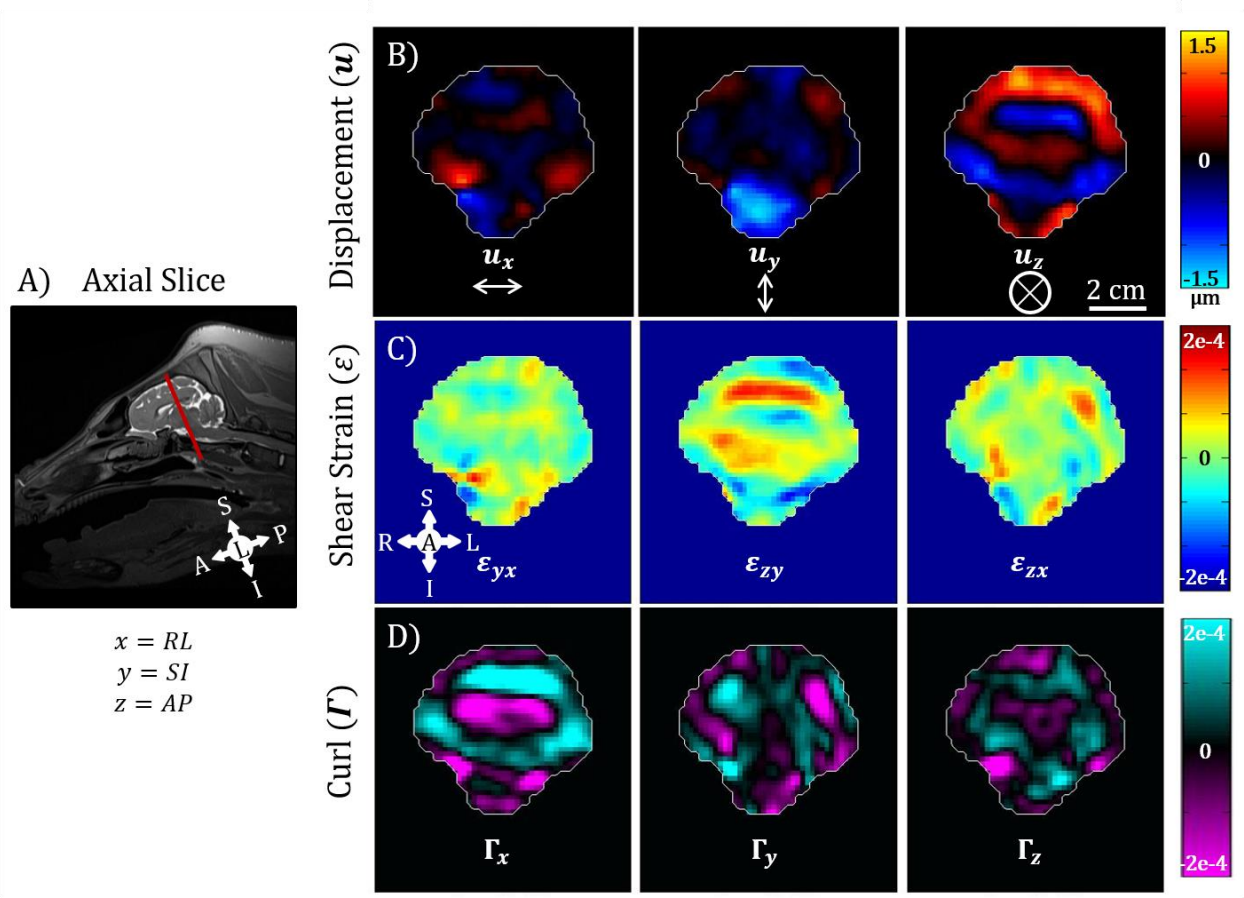

Figure 3.3: *In vivo* MRE results for one axial slice of mini-pig brain at 100 Hz imaged while positioned in dorsal recumbency. (A) Image slice location. (B) Three components of displacement. (C) Three components of shear strain. (D) Three components of curl.

Figure 3.4 shows examples of displacement, shear strain, and curl maps for one coronal slice of porcine brain tissue *ex vivo*. The dominant displacement component (~15 μm amplitude) during shear wave propagation is in the out-of-plane (u_z) direction, which is the inferior-superior (IS) direction with respect to the brain. The curl of the wave field shows that the propagation of the waves occurs radially outward in the *xy*-plane. The largest components of curl and strain are ~2×10^{-3} mm/mm, which are well within the small-deformation regime.

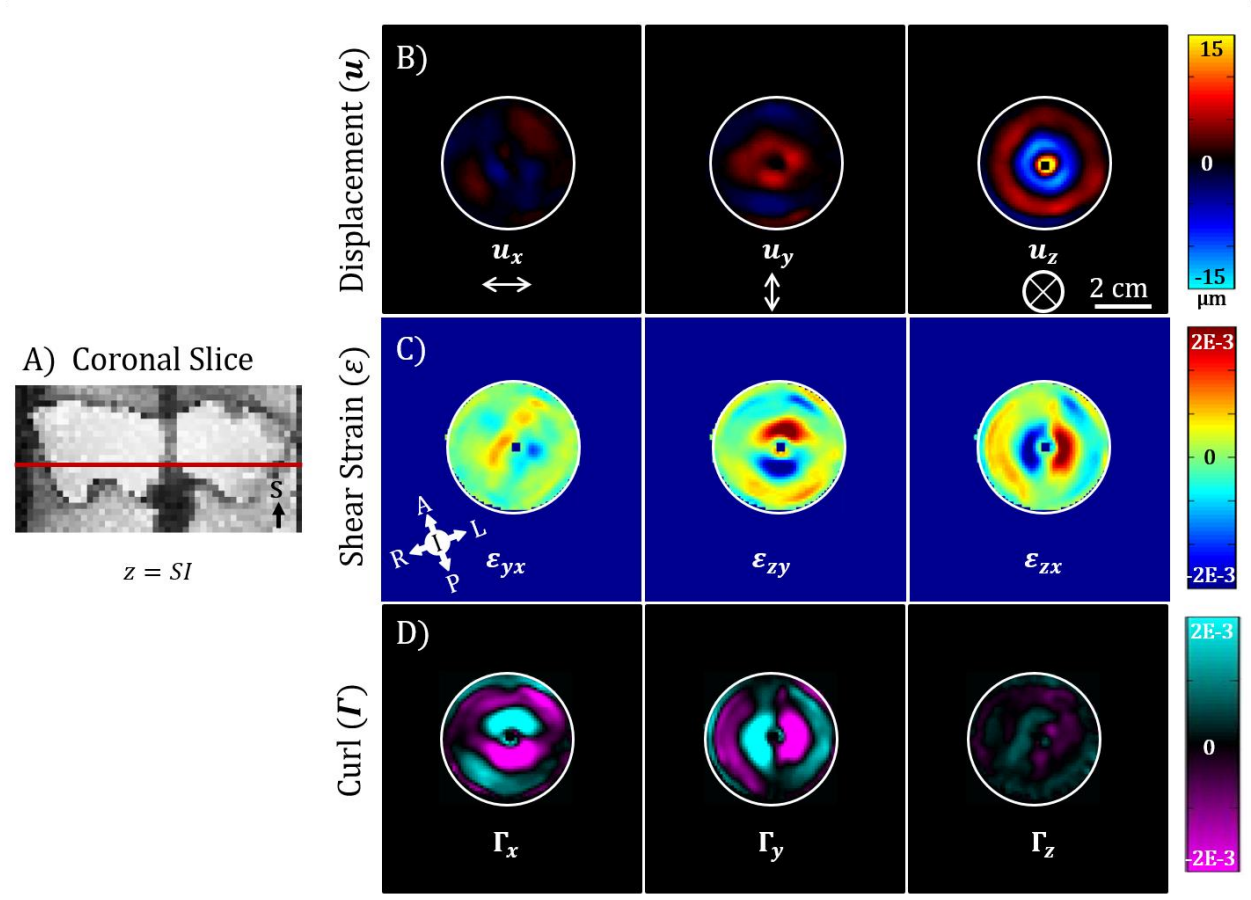

Figure 3.4: *Ex vivo* MRE results for one axial slice of brain tissue at 100 Hz. A) Image slice location. Images are from the same mini-pig shown in Figure 3.3. B) Three components of displacement. C) Three components of shear strain. D) Three components of curl. Note orientations and scale bars are different from Figure 3.3.

Figure 3.5 displays storage modulus estimates for four representative *in vivo* axial slices spaced 7.5 mm apart and one representative *ex vivo* coronal slice estimated using LDI for the data taken at 100 Hz. The *ex vivo* sample is surrounded by the gelatin, which is represented by the less stiff (~1 kPa) estimates in the image.

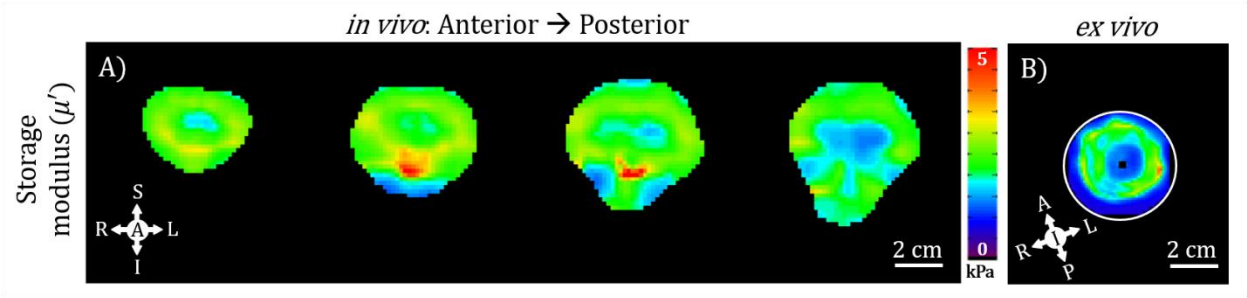

Figure 3.5: A) Storage modulus (μ') at 100 Hz *in vivo* estimated using LDI. The AP component of motion is shown for the same image slices as in Figure 3.3 A and B. μ' was only estimated for voxels where >50% of the 7x7x7 fitting kernel was inside the brain. B) Storage modulus (μ') at 100 Hz *ex vivo* estimated using LDI. The SI component of motion is shown for the same image slice as in Figure 3.3 C and D. μ' was only estimated for voxels where >50% of the 7x7x7 fitting kernel was inside the sample. Note: Image scales are the same in each panel (scale bars = 2 cm), but image slice orientations differ between panels A and B.

To compare property estimates *in vivo* and *ex vivo*, an ROI was defined in the *in vivo* image volume to match the dissected sample used in *ex vivo* scanning. The ROI (Figure 3.6) is a 42 mm cylinder that includes the corpus callosum and superior regions. To remove the effects of the gelatin surrounding the *ex vivo* sample and the estimates near the actuator rod, the ROI for the *ex vivo* stiffness data was eroded using the MATLAB *imerode* command (2014a, MathWorks, Natick, MA) with a 7x7x7 kernel.

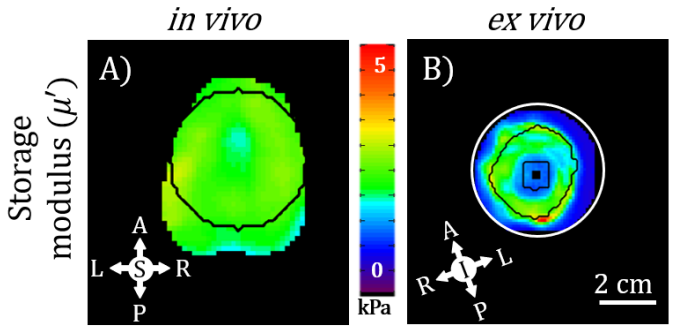

Figure 3.6: LDI-estimated storage modulus (μ') for one *in vivo* (A) and one *ex vivo* (B) mini-pig coronal brain slice using 7x7x7 kernel for LDI. Black outlines denote the area used in the comparison between *in vivo* and *ex vivo* samples. The *ex vivo* sample was eroded using a 7x7x7 kernel to remove the influence of gelatin on μ' estimates.

Figure 3.7 displays histograms of LDI estimates of storage modulus (μ') values for all voxels from the ROI of the *in vivo* image volume and from the eroded ROI of the *ex vivo* sample from all scans

performed at 100 Hz and 125 Hz. The mean for each data set is depicted by the dashed line. These histograms show (i) higher stiffness at the higher frequency, and (ii) *in vivo* tissue is stiffer than *ex vivo* tissue. The effect of orientation (dorsal or ventral) *in vivo* on brain stiffness was checked, and found to be small (voxelwise mean ± std.: 0.779 ± 0.347 kPa dorsal vs. 0.777 ± 0.468 kPa ventral for 50 Hz; 2.264 ± 0.649 kPa vs. 2.381 ± 0.820 kPa for 100 Hz).

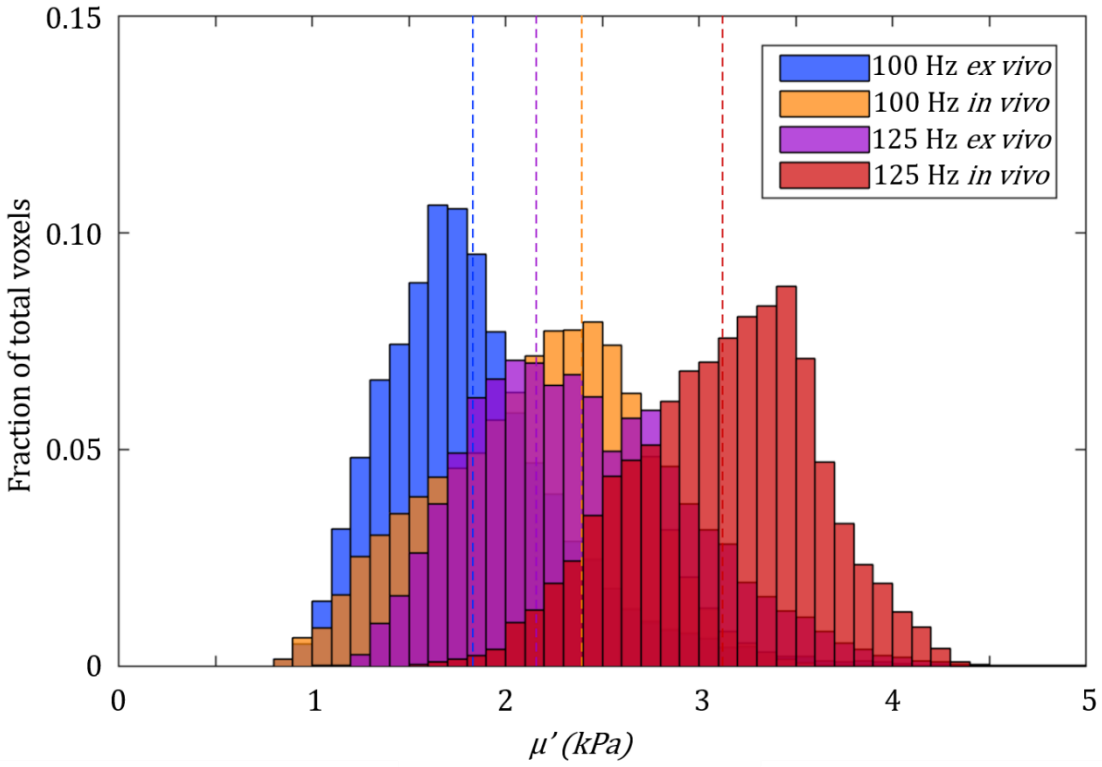

Figure 3.7: Histogram of LDI-estimated storage modulus (μ') values of all pixels for *in vivo* (orange and red) and *ex vivo* (blue and purple) calculated at 100 and 125 Hz using a 7x7x7 kernel for all of the scanned mini-pigs. Dotted lines represent the mean μ' value. *In vivo* voxels are from the cylindrical ROI shown in Figure 3.6A. *Ex vivo* voxels are from the eroded ROI shown in Figure 3.6B.

At each frequency, the mean storage and loss moduli from the ROI of the *in vivo* image volume were estimated, along with the corresponding mean storage and loss moduli in the eroded ROI of the *ex vivo* image volume. The means and standard deviations of these parameters are plotted versus frequency in Figure 3.8. Both *in vivo* and *ex vivo* estimates of storage modulus increase

with frequency. Notably, estimates of storage modulus are higher for the *in vivo* data than for the *ex vivo* data at all common frequencies. Multivariate regressions of storage and loss moduli were performed using a linear mixed-effects model with random subject effects. Group (*in vivo* vs. *ex vivo*), frequency, and their interaction were the independent predictors (Appendix B). For storage modulus, the slopes between *in vivo* and *ex vivo* were significantly different ($p < 0.0001$) and frequency was a good predictor of the data ($p < 0.0001$). No significant differences were observed between loss moduli *in vivo* and *ex vivo* over this frequency range ($p = 0.285$). The linear mixed-effects model is included with mean storage and loss modulus estimates, in Figure 3.8. Storage and loss modulus estimate were also fitted to several candidate rheological models (Appendix C).

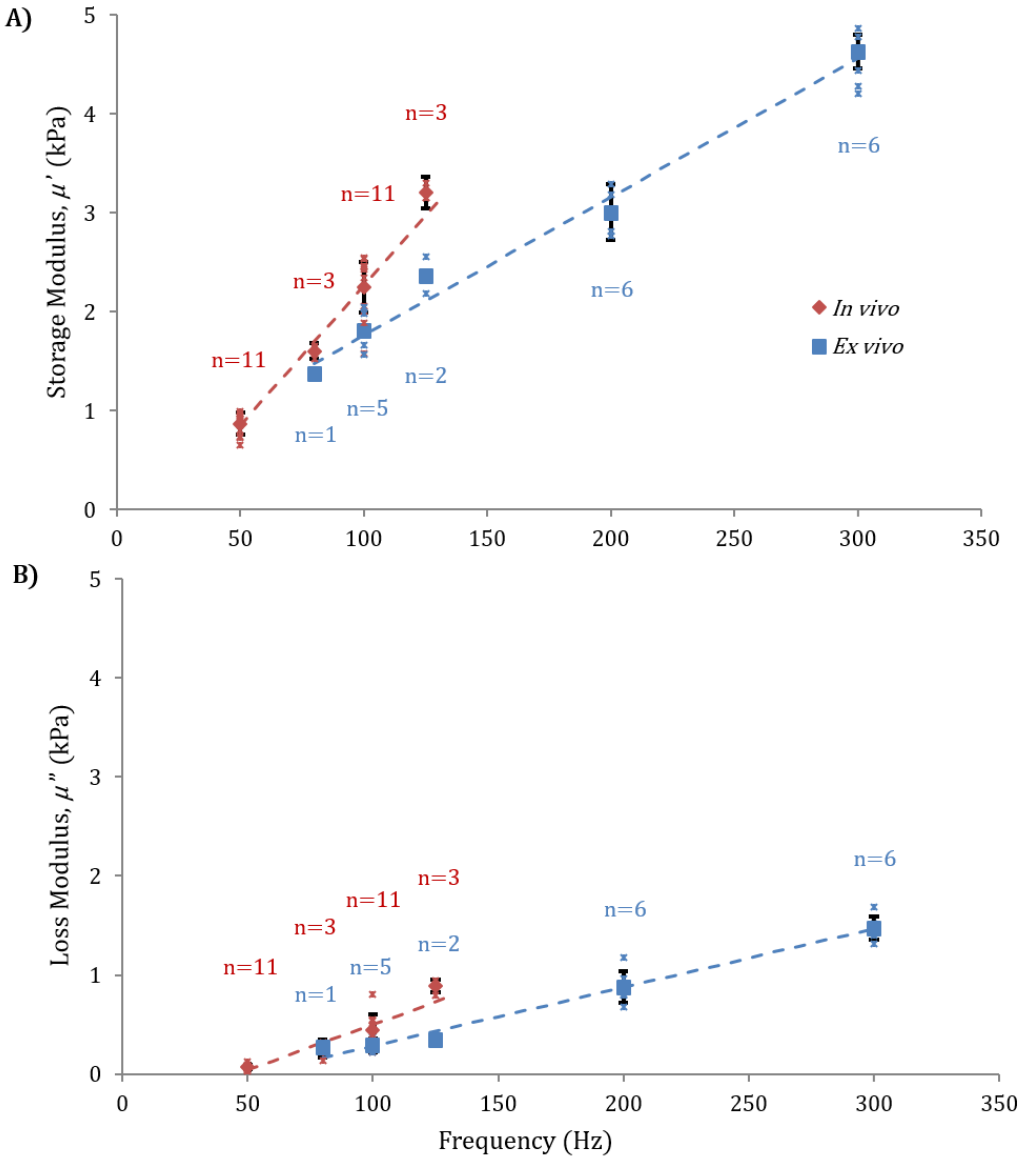

Figure 3.8: Mean storage modulus (μ') and loss modulus (μ'') of *in vivo* (red) and *ex vivo* (blue) mini-pig brain tissue estimated by LDI at frequencies from 50-300 Hz for N=6 animals. Each small asterisk (*) represents the mean μ' or μ'' for one mini-pig scanned at the specified frequency. Each larger marker (blue □ and red ◊) represents the mean μ' or μ'' for all mini-pigs scanned at the specified frequency. Notations above/below markers provide the number of scans represented by the mean value. Standard deviations were only provided for data sets with n ≥ 3. For *in vivo* data, each marker shows the average modulus estimate in a cylindrical ROI of dimensions matching that of the *ex vivo* cylindrical sample (Figure 3.1B). Multivariate linear regressions of μ' and μ'' were performed using a linear mixed-effects model with subject as a random effect (dashed lines; see Appendix B). *In vivo*: $\mu' = 0.85 + 0.0283(f - 50)$; $\mu'' = 0.041 + 0.00916(f - 50)$. *Ex vivo*: $\mu' = 1.48 + 0.0140(f - 80)$; $\mu'' = 0.164 + 0.00592(f - 80)$. (A) Estimates of μ' increase with frequency due to viscoelasticity. At the common frequencies, 80, 100, and 125 Hz, μ' estimates are higher for brain tissue *in vivo* than for brain tissue samples *ex vivo*. (B) Estimates of μ'' increase with frequency due to viscoelasticity.

3.5 Discussion and Conclusions

This study provides the first comparison of *in vivo* and *ex vivo* material properties throughout a volume of brain tissue in the same large animal using MRE. MRE was performed on brain tissue both *in vivo* and *ex vivo* at multiple frequencies, illuminating the viscoelastic behavior of brain tissue under both conditions. MRE estimates of storage modulus suggest that tissue in the intact, living brain is stiffer than in *ex vivo* samples. Direct comparison was possible at overlapping frequencies of 80 Hz, 100 Hz, and 125 Hz. Estimates in *ex vivo* tissue at other frequencies (200 Hz, and 300 Hz) support this general observation.

MRE in pigs is quantitatively similar to MRE in humans. In Figure 3.3 the magnitude of wave displacement *in vivo* is on the order of 1-2 microns, similar to magnitudes observed in human studies *in vivo* using a "pillow" actuator [32] or "paddle" actuator [105]. The largest component of wave motion in the current *in vivo* studies is in the AP direction. Larger amplitudes are achieved in the *ex vivo* sample since waves are excited by direct vibration of the tissue; the largest component of wave motion is in the SI direction.

Our estimates of storage modulus *ex vivo* at 80 Hz are within 15% of several estimates from the literature on the porcine brain taken using MRE [17] or oscillatory shear strain at 2.5% [101, 106]. At higher frequencies, the current *ex vivo* estimates of storage modulus are greater than prior estimates in porcine brain and exhibit a steeper dependence on frequency [17, 101, 106]. Current estimates of loss modulus for *ex vivo* are lower than prior estimates [17, 101, 106].

What might explain the observed mechanical differences between *in vivo* and *ex vivo* brain tissue? *Ex vivo* tissue experiences neither perfusion nor metabolic activity, and any residual stress in *ex*

vivo tissue is relieved by dissection. More comprehensive studies are needed to determine which factors might explain observed stiffness differences.

It is possible that anisotropy of white matter might have contributed to differences between *in vivo* and *ex vivo* parameter estimates [30, 31, 83]. Anderson et al. found ~20% differences in estimated storage modulus of white matter between areas where displacements were primarily parallel vs. perpendicular to the dominant fiber direction [83]. In the current study, although the dominant tissue motions were in different anatomical directions *in vivo* and *ex vivo*, in both cases tissue displacements were perpendicular to the dominant (right-left) fiber direction. Tissue motion *in vivo* was primarily anterior-posterior (Figure 3.3) and tissue motion *ex vivo* was primarily superior-inferior (Figure 3.4); both are perpendicular to the fiber axis. Also, differences between *in vivo* and *ex vivo* estimates diminish at low frequencies. Thus, anisotropy is unlikely to explain the observed differences.

Temperature affects tissue properties. We did not monitor the sample temperature in the current *ex vivo* studies, but in prior studies with gelatin samples [1] sample temperature during MRE was ~21°C, which is substantially lower than *in vivo* (~37°C). However, in viscoelastic tissue lower temperatures are typically associated with higher storage modulus [13], which would tend to mask observed differences.

The pig brain *in vivo* is surrounded by CSF and skull; *ex vivo* tissue was encased in gelatin in a plastic container. Boundaries should have minimal effects in both cases because we analyzed only interior ROIs removed from the boundaries. Also, differences in estimated properties are greater

at higher frequencies, at which the effects of boundaries are likely less important, due to shorter wavelengths.

Future studies could investigate *ex vivo* brain tissue *in situ* (i.e., in the intact head post mortem) to account for factors related to tissue extraction. However, the logistical challenges of doing *in vivo*, *in situ*, and *in vitro* MRE in the same animal are substantial.

Other limitations exist for both *in vivo* and *ex vivo* experiments. Since the porcine brain is small (~100 g), images are at a lower resolution, relative to brain anatomical structures, than typical human scans. Due to differences in actuation and sample geometry, the frequency ranges for *in vivo* and *ex vivo* studies did not overlap completely. The mini-pig head *in vivo* has thick layers of bone, fat and muscle, so that frequencies above 125 Hz dissipated before reaching the brain. In the *ex vivo* sample, below 80 Hz, insufficient wavelengths were obtained for accurate parameter estimation. Strain amplitudes were higher in *ex vivo* experiments, though in both *in vivo* and *ex vivo* samples strains were < 0.2%, well within the small-strain (linear) regime. Differences between *in vivo* and *ex vivo* studies and data characteristics are summarized in Appendix A.

3.6 Summary

This study shows notable differences between material properties estimated by MRE *in vivo* and *ex vivo* in similar volumes of brain tissue from the same animal, over multiple frequencies. Although many *ex vivo* measurements of brain tissue mechanical properties are available, only limited data have been obtained *in vivo*. Thus, most TBI simulations incorporate material parameters measured *ex vivo*. The current results thus represent progress toward accurate simulation of TBI in the intact, living brain.

Although this study provided insight into the differences between *in vivo* and *ex vivo* mechanical properties of the brain, the approach is fundamentally limited by the assumptions of conventional MRE. MRE assumes that the material is locally homogeneous and isotropic, while brain tissue is heterogeneous (with dimensions of heterogeneous structures shorter than the wavelength of shear waves in MRE) and white matter in the brain is anisotropic. Therefore, as described in the following chapters, I explored how MRE could be used to estimate parameters of an anisotropic material model.

Chapter 4:Contributions of shear and tensile anisotropy to mechanical properties estimated by MRE with boundary excitation

4.1 Overview

Accurate mechanical properties are essential for modeling traumatic brain injury. White matter (WM) in the brain is structurally anisotropic, consisting of variably aligned, myelinated, axons, but there is limited data on whether it is also mechanically anisotropic [107]. In MRE, shear waves are imaged with MRI and fitted to a material model; however, most models used in MRE are isotropic. The simplest anisotropic model for fibrous tissue is the incompressible, transversely isotropic (ITI) material, parameterized by baseline shear modulus (μ), shear anisotropy ($\phi = \mu_1/\mu - 1$), and tensile anisotropy ($\zeta = E_1/E_2 - 1$). To assess shear and tensile anisotropy, shear wave propagation and polarization directions, relative to fiber direction, must be considered [108]. In this chapter, the WM of the minipig brain is mechanically characterized using the ITI material model; data from simulations of shear waves in a cube of ITI material are used to demonstrate and evaluate the estimation approach.

4.2 Objective

MRE is an important imaging tool used to noninvasively estimate material properties of tissue [51]. However, its estimates are dependent on the assumptions used for the material model. Brain tissue is a complex material, composed of gray and white matter. Gray matter, which contains neuronal and glial cell bodies, is considered mainly isotropic, however white matter is composed

of aligned axonal fibers, resulting in structural anisotropy. This anisotropy may be important in the understanding and diagnosis of the numerous brain injuries and neurological diseases associated with axons [25, 109-115]. Specifically, traumatic brain injury (TBI) is often the result of diffuse axonal injury caused by the shearing of white matter, and multiple sclerosis (MS) is associated with loss of myelin from axons.

Despite the importance of white matter, brain tissue has commonly been modeled as an isotropic material. A few recent studies have begun to consider anisotropy of soft tissue. The anisotropic material models vary in the number of parameters estimated. One anisotropic model includes two parameters, accounting only for the shear anisotropy of breast tissue [75] and skeletal muscle [76]. Others [82] include five or more material parameters to model brain tissue as either a transversely isotropic (TI) or orthotropic, linear, elastic material. Another anisotropic model used considers white matter to be an *incompressible* transversely isotropic (ITI) material containing both shear and tensile anisotropy [30, 58, 81, 116].

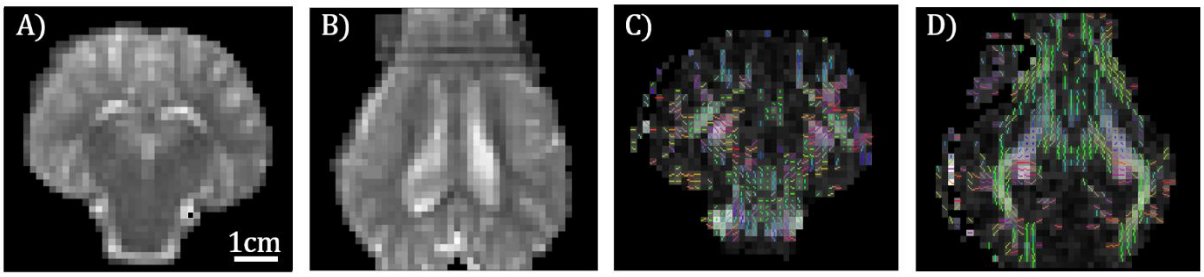

Figure 4.1: (A,B) MRE magnitude images of mini-pig brain (coronal and axial planes). (C,D) Principal eigenvectors of the diffusion tensor, encoded by color, showing regions of anisotropy in the white matter for an coronal and axial slice. Red = left-right (LR); Green = anterior-posterior (AP); Blue = inferior-superior (IS).

For this study, the ITI model was used to investigate brain anisotropy. As shown in Chapter 2 and references [30, 31] the ITI material can be described by 3 parameters: baseline shear modulus (μ),

shear anisotropy (ϕ), and tensile anisotropy (ζ). These parameters are based on the shear and tensile moduli of the material parallel (μ_1 and E_1) and perpendicular (μ_2 and E_2) to the fiber direction of the material. The parameters are defined as

$$\mu = \mu_2 \tag{4.1}$$

$$\phi = \frac{\mu_1}{\mu_2} - 1 \tag{4.2}$$

$$\zeta = \frac{E_1}{E_2} - 1 \tag{4.3}$$

The three parameters of this model can be estimated using shear wave speed, propagation direction, polarization direction, and fiber direction (see Chapter 2 and references [30, 31] for details). Shear waves traveling through an ITI material can be characterized as either slow shear waves ($\boldsymbol{m_s}$) or fast shear waves ($\boldsymbol{m_f}$). The polarization directions are determined by the cross product of the shear wave propagation direction ($\boldsymbol{n}$) and the material fiber direction ($\boldsymbol{a}$), as shown in the following equations.

$$\boldsymbol{m_s} = \boldsymbol{n} \times \boldsymbol{a} / |\boldsymbol{n} \times \boldsymbol{a}| \tag{4.4}$$

$$\boldsymbol{m_f} = \boldsymbol{n} \times \boldsymbol{m_s} \tag{4.5}$$

Slow shear waves do not stretch the fibers in the ITI material. Therefore, the slow shear wave speed (c_s) depends only on μ, density (ρ), ϕ, and the angle between the fiber direction and the propagation direction (θ).

$$c_s^2 = \frac{\mu}{\rho}[1 + \phi \cos^2(\theta)] \tag{4.6}$$

Fast shear waves stretch the fibers in the material, so the fast shear wave speed (c_f) is also dependent on ζ.

$$c_f^2 = \frac{\mu}{\rho}[1 + \phi \cos^2(2\theta) + \zeta sin^2(2\theta)] \tag{4.7}$$

These equations can be multiplied by density to give the apparent shear modulus for slow and fast waves.

$$\rho c_s^2 = \mu[1 + \phi \cos^2(\theta)] = \mu_s \tag{4.8}$$

$$\rho c_f^2 = \mu[1 + \phi \cos^2(2\theta) + \zeta sin^2(2\theta)] = \mu_f \tag{4.9}$$

Apparent shear modulus can be estimated using shear waves. This chapter will introduce a three-parameter anisotropic analysis using surface-generated shear waves. This method will be used to estimate material properties in two fibrous cube simulations and the mini-pig brain.

4.3 Methods

4.3.1 Simulation

Finite element model (COMSOL Multiphysics; v. 5.3a, Stockholm, Sweden) of a nearly-incompressible transversely isotropic (NITI) cube and a cube with two main fiber directions that cross in the center (referred to as "X-Box") were used to represent MRE in anisotropic tissues of varying complexity. The data from these ideal situations were used to validate and assess methods for anisotropic parameter estimation.

The simulation domain was a linear, elastic, nearly incompressible cube of 0.05 m side length. The solution for the steady state frequency response was found using COMSOL's frequency domain solver. The boundaries of the cube were rigid. Displacement data from the simulation were exported into MATLAB and interpolated onto a 3D grid with 1 mm^3 voxel resolution for analysis using the LiveLink feature of COMSOL ("*mphinterp*" command).

4.3.1.1 Cube Domains

The given material parameters for the NITI cube model were $\mu = 1000$ Pa, $\phi = 1, \zeta = 2$, with a bulk modulus, $\kappa = 1000\ kPa$. A harmonic (sinusoidal) boundary load of 5 N/m^2 at 100 Hz was applied to the top surface of the cube (surface normal to the *z*-axis) along the *y*-direction. For each simulation, the cube material was homogenous with one fiber direction at an angle of $\alpha = 0°, 15°, 30°, 45°,$ or $90°$ to either the *x*-axis or *y*-axis, creating a total of 10 models. The simulation domain consisted of 16,250 quadratic Lagrange elements, corresponding to 431811 degrees of freedom.

Figure 4.2 shows the ten cubes used in the simulation. The fiber direction of each cube is shown by the colormap. While the fiber direction varies from 0° to 90°, all ten cases have the same shear wave propagation direction ($\boldsymbol{n}$). The shear wave polarization directions depend on the orientation of the fiber direction and propagation direction, calculated using equations 4.4 and 4.5. All cases with fibers along the *x*-axis (Figure 4.2 A) have a slow polarization direction ($\boldsymbol{m_s}$) along the *y*-axis and a fast polarization direction ($\boldsymbol{m_f}$) along the *x*-axis. All cases with fibers along the *y*-axis (Figure 4.2 B) have the opposite slow and fast polarization directions, with a slow polarization direction ($\boldsymbol{m_s}$) along the *x*-axis and a fast polarization direction ($\boldsymbol{m_f}$) along the *y*-axis.

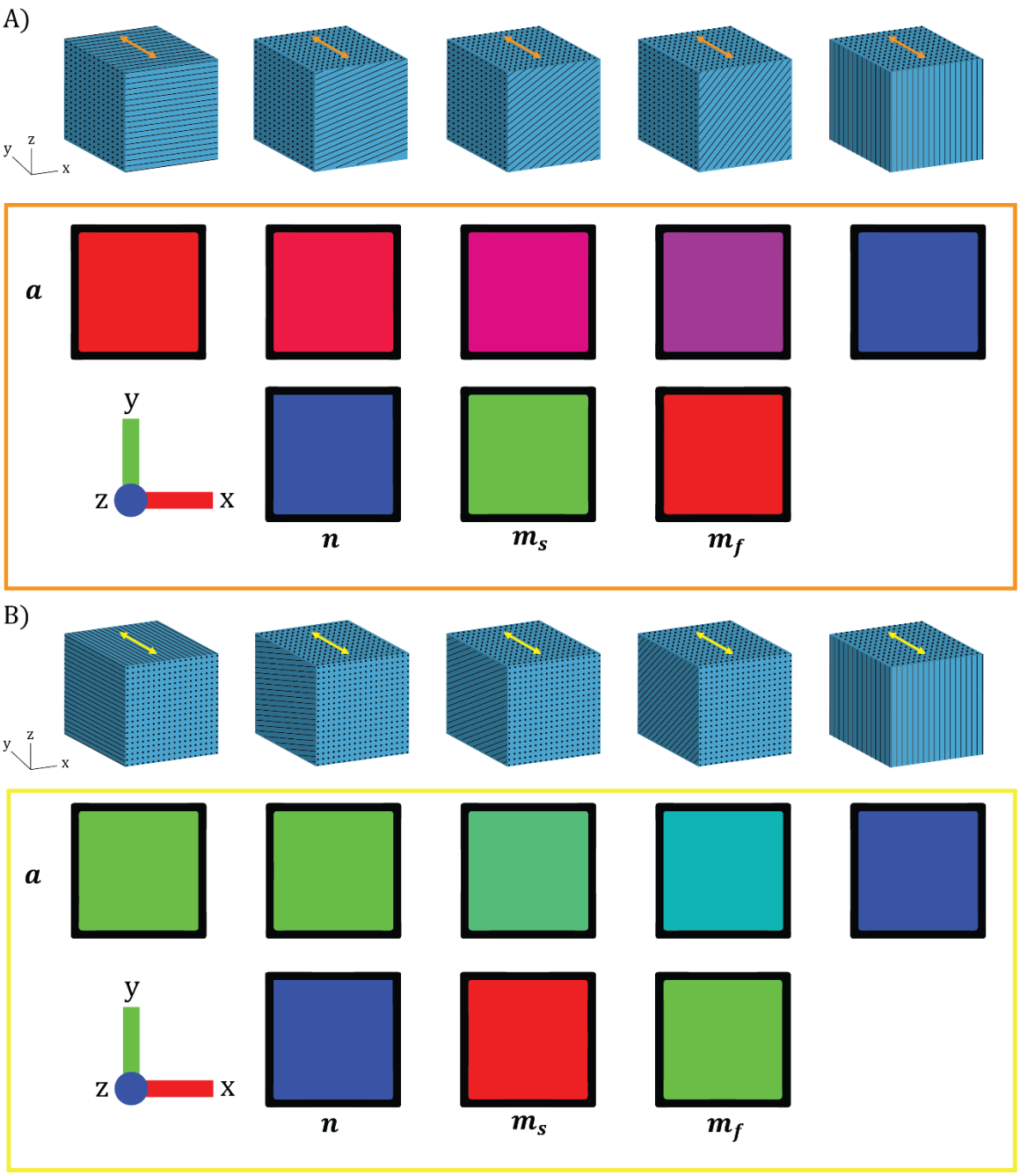

Figure 4.2: Ten NITI cubes of various fiber directions were vibrated at 100 Hz on the top surface along the *y*-axis. (A) Five cubes with fibers at $\alpha = 0°, 15°, 30°, 45°,$ or $90°$ (left to right) to the *x*-axis. Black lines represent the fibers of the material. Black dots represent the fiber ends. A boundary load of 5 N/m^2 was applied to the top surface in the *y*-direction at 100 Hz. The fiber directions ($\boldsymbol{a}$) of the five cubes are shown below by color, where red is along the *x*-axis, green is along the *y*-axis, and blue is along the *z*-axis. The third row depicts the propagation direction ($\boldsymbol{n}$), slow polarization direction ($\boldsymbol{m_s}$), and fast polarization direction ($\boldsymbol{m_f}$) for all five cases by color. (B) Five cubes with fibers at $\alpha = 0°, 15°, 30°, 45°,$ or $90°$ (left to right) to the *y*-axis. Black lines represent the fibers of the material. Black dots represent the fiber ends. A boundary load of 5 N/m^2 was applied to the top surface in the *y*-direction at 100 Hz. The fiber directions ($\boldsymbol{a}$) of the five cubes are shown below by color, where red is along the *x*-axis, green is along the *y*-axis, and blue is along the *z*-axis. The third row depicts the propagation direction ($\boldsymbol{n}$), slow polarization direction ($\boldsymbol{m_s}$), and fast polarization direction ($\boldsymbol{m_f}$) for all five cases by color.

4.3.1.2 X-Box Domains

The given parameters for the two NITI fiber tracks of the "X-Box" cube were $\mu = 1000$ Pa, $\phi = 1$, and $\zeta = 2$. The fiber tracts were at $\alpha = 0°, \pm 15°, \pm 30°,$ or $\pm 45°$ to the *y*-axis. The cube section that did not contain fibers is an isotropic material with $\mu = 1000$ Pa. A harmonic (sinusoidal) boundary load of 5 N/m^2 at 100 Hz was applied to either the *x*-*y* plane, *y*-*z* plane, or *x*-*z* plane surface in different directions to create a variety of shear waves through the cube. The domain consisted of 45,671-83,811 quadratic Lagrange elements, corresponding to 329,062-371,160 degrees of freedom. Figure 4.3 shows the four different cubes with all the actuation directions, making a total of 18 different simulation cases.

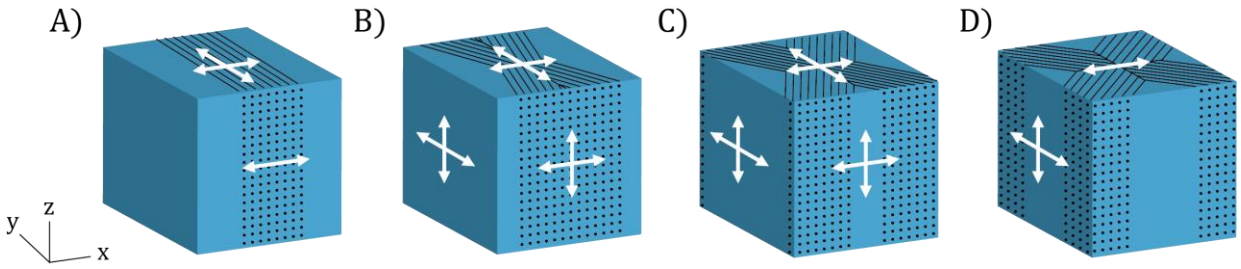

Figure 4.3: Four cube layouts with fiber tracts at $\alpha = 0°, \pm 15°, \pm 30°,$ or $\pm 45°$ (left to right) to the *y*-axis. One boundary load was applied to either the x, y, or z plane to produce a variety of shear waves through the cubes. The white arrows demonstrate all the different possible actuation directions for each cube, resulting in a total of 18 different models. Black lines represent the fibers of the material. Black dots represent the fiber ends.

For simplicity, all further images for the NITI cube will reference only the 45° cube and its three different actuation directions. Figure 4.4 shows this case and the three directions of displacement ($Re(u), Re(v),$ and $Re(w)$) along an *x*-y plane in the center of the 45° cube.

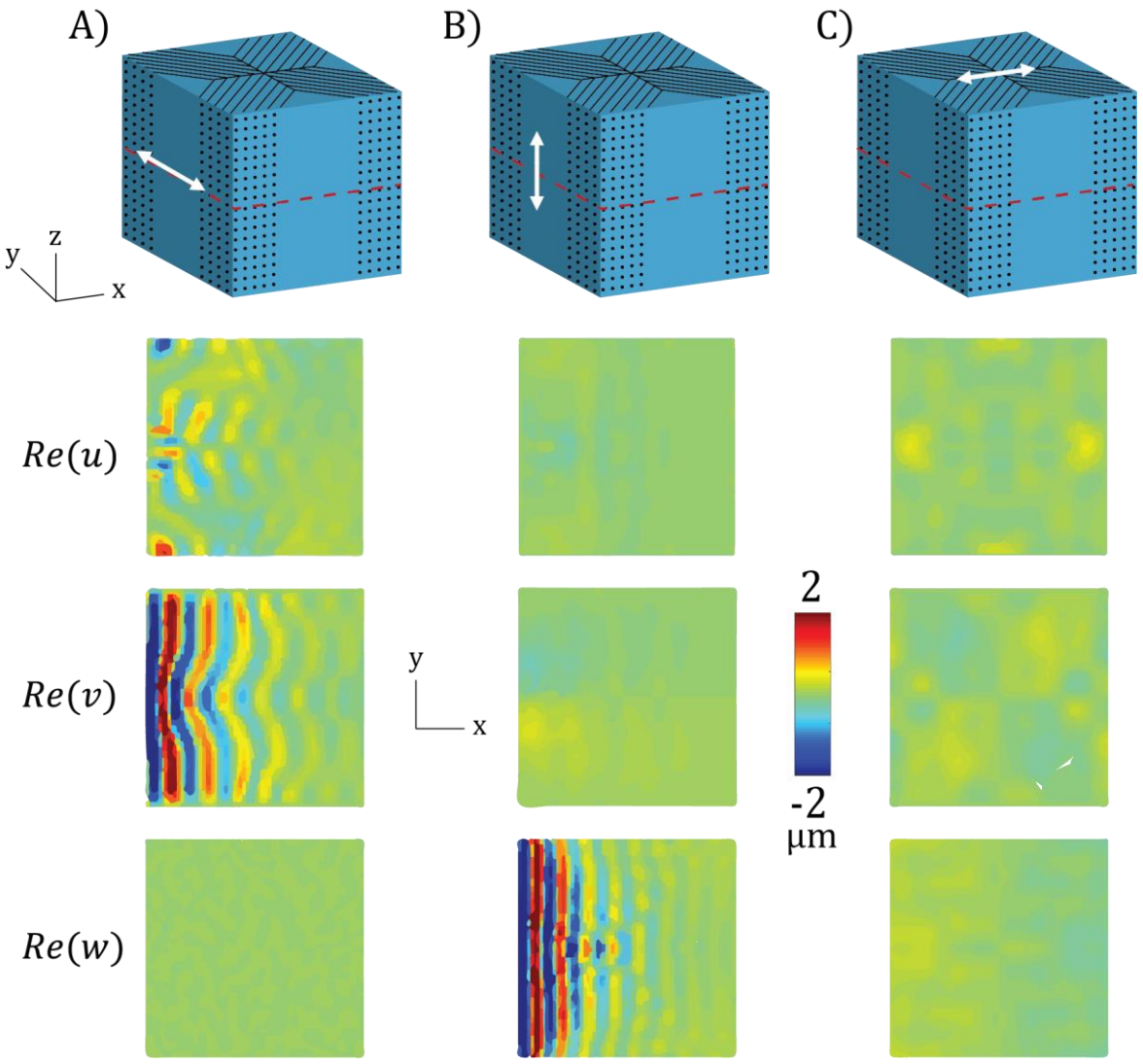

Figure 4.4: Shear wave displacement components in three directions, imaged on the center *x*-y plane of the cube for the 45° cube and its three actuation cases. The red dotted line shows the position of the slice in the cube. (A) 45° cube with actuation along the *y*-axis on the face perpendicular to the *x*-axis. The greatest displacement component is $Re(v)$. (B) 45° cube with actuation along the *z*-axis on the face perpendicular to the *x*-axis. The greatest displacement component is $Re(w)$. (C) 45° cube with actuation along the *x*-axis on the face perpendicular to the *z*-axis. The greatest displacement component is $Re(u)$, but no waves can be seen along the *x*-y central plane due to dissipation.

Figure 4.5 shows the three 45° X-Box cases and their fiber direction ($\boldsymbol{a}$), shear wave propagation direction ($\boldsymbol{n}$), and polarization directions ($\boldsymbol{m_s}$ and $\boldsymbol{m_f}$). The shear waves propagate in the *x*-direction for the two cases with actuation on the *y*-*z* face (Figure 4.5 A and B). The shear waves propagate in the *z*-direction when the actuation is on the *x*-*y* face (Figure 4.5 C). The shear wave polarization directions depend on the orientation of the fiber direction and propagation direction,

calculated using equations 4.4 and 4.5. The cases actuated on the *y*-*z* face (Figure 4.5 A and B) have a slow polarization direction ($\boldsymbol{m_s}$) along the *z*-axis and a fast polarization direction ($\boldsymbol{m_f}$) along the *y*-axis. The case actuated on the *x*-*y* face (Figure 4.5 C) has a slow polarization direction ($\boldsymbol{m_s}$) and a fast polarization direction ($\boldsymbol{m_f}$) along the fiber direction.

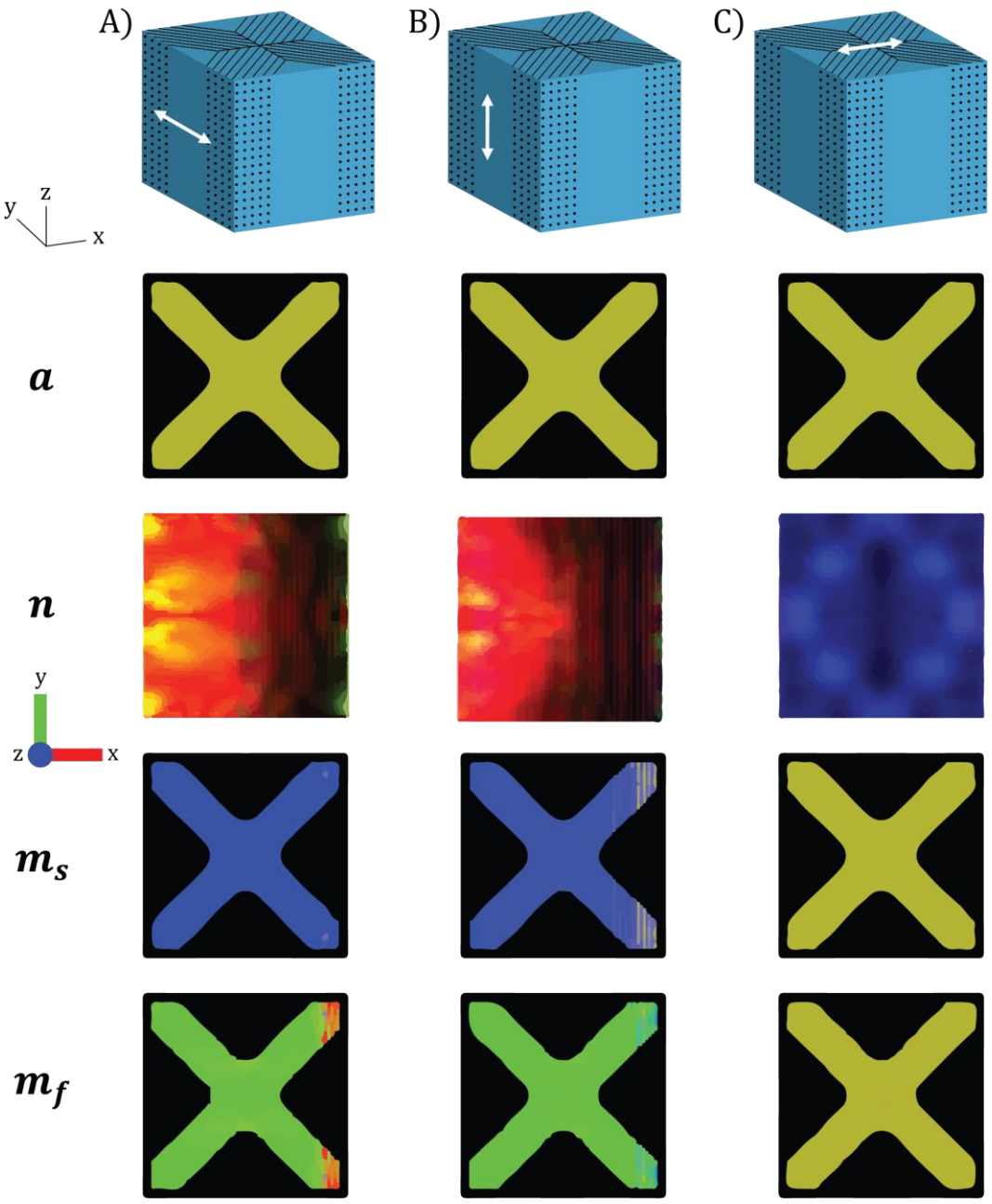

Figure 4.5: Shear wave displacements in three directions, imaged on the center *x*-*y* plane of the cube for the 45° cube and its three actuation cases. Black lines represent the fibers of the material. Black dots represent the fiber ends. The second row is the fiber direction ($\boldsymbol{a}$) of the cubes shown below by color, where red is along the *x*-axis, green is along the *y*-axis, and blue is along the *z*-axis. The third row depicts the shear wave propagation direction ($\boldsymbol{n}$). The fourth and fifth row depict slow polarization direction ($\boldsymbol{m_s}$), and fast polarization direction ($\boldsymbol{m_f}$) for the cases by color. (A) 45° cube with actuation along the *y*-axis on the face perpendicular to the *x*-axis. $\boldsymbol{n}$ is in the *x*-direction, $\boldsymbol{m_s}$ is in the *z*-direction, and $\boldsymbol{m_f}$ is in the *y*-direction. (B) 45° cube with actuation along the *z*-axis on the face perpendicular to the *x*-axis. $\boldsymbol{n}$ is in the *x*-direction, $\boldsymbol{m_s}$ is in the *z*-direction, and $\boldsymbol{m_f}$ is in the *y*-direction. (A) 45° cube with actuation along the *x*-axis on the face perpendicular to the *z*-axis. $\boldsymbol{n}$ is in the *z*-direction, $\boldsymbol{m_s}$ is in the fiber direction, and $\boldsymbol{m_f}$ is in the fiber-direction.

4.3.2 Experimental

MRE and diffusion tensor imaging (DTI) were performed on six (6) healthy Yucatan mini-pigs *in vivo* on a Siemens Prisma® 3T MRI scanner. Mini-pigs ranged between 4 and 8 months. Animals were anesthetized during scanning with isoflurane 1-2% in air. A total of 13 scans (13 DTI and 26 MRE) were used for this study. (The MRE data were also used for the *in vivo / ex vivo* study of Chapter 3).

Mini-pigs were scanned positioned in either ventral or dorsal recumbency using a Siemens 18-Channel Body Matrix Coil or an open Siemens Head/Neck 20 coil. A combination of bean bags, rolled towels, and Velcro straps were used to secure the head of the mini-pig to limit bulk ("rigid-body") motion.

4.3.2.1 MRE

Shear waves were excited at 50 (n=11), 80 (n=2), 100 (n=10), and 125 (n=3) Hz using a multi-directional jaw actuator driven by the Resoundant™, a commercially available pneumatic diver [89]. The layout can be seen in Figure 4.6.

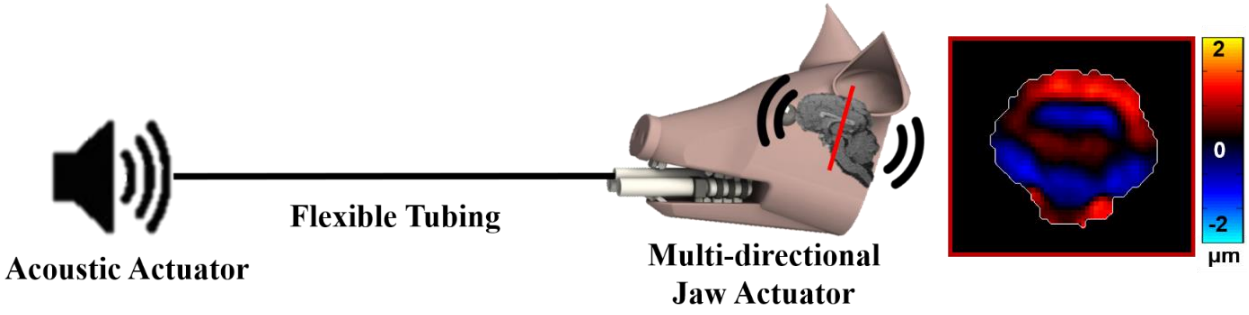

Figure 4.6: Schematic of setup for MRE scans. Acoustic actuator pneumatically drives multidirectional jaw actuator. They are connected by flexible plastic tubing. Jaw actuator is securely between the back molars of the mini-pig jaw. It vibrates the teeth and skull of the mini-pig, which vibrates the brain. The right image shows the shear wave displacements of the coronal slice (red line) at 50 Hz actuation.

MRE data with 3D displacements encoded as phase were acquired using a 2D multi-shot sequence [103]. The scan used 1.5 mm isotropic voxels that covered a volume of 180 x 180 x 60 mm^3. Each scanning session collected MRE data for 1-3 different actuation frequencies. Shear wave displacements ($\boldsymbol{u}$) were calculated after removing bulk motion from the MRE data. Amplitude-weighted propagation direction ($\boldsymbol{n}$) was determined by directionally filtering the MRE displacement field in 92 directions (Chapter 2.3.4 [6]).

4.3.2.2 DTI

Diffusion tensors were estimated using 20 (n=1) or 30 (n=12) diffusion-weighted directions, with 2-4 scan averages. The DTI scan used the same 1.5 mm isotropic voxel resolution and center of slice groups as the MRE scan but imaged a larger imaging volume of 192 x 192 x 72 mm^3. Fractional anisotropy (FA) was estimated from diffusion tensor eigenvalues, and fiber direction ($\boldsymbol{a}$) from the first principal eigenvector (Eq. 2.58).

4.3.3 Approach to Anisotropic Property Estimation

4.3.3.1 Overview of Approach to Anisotropic Property Estimation

Directional filtering with local direct inversion (DF-LDI) was used to estimate the material properties of the samples. This approach separated the waves by their polarization direction and classified as either “slow” or “fast” shear waves and approximated the apparent shear modulus (ρc^2) for both wave types. The three unknown parameters of the NITI material were estimated from the equations for slow and fast shear waves using a multiple linear regression model.

4.3.3.2 Classification of Voxels as "Slow" or "Fast"

To be included in the analysis, voxels had to meet multiple conditions to ensure they matched the approximations and assumptions for the analysis. A voxel was only included if (i) it experienced a wave amplitude above a threshold and (ii) the voxel had a fractional anisotropy above a threshold. Table 4.1 outlines the inclusion criteria for the analysis.

Table 4.1: Inclusion criteria for analysis of anisotropic parameter estimation for both simulations and experiments. Parameters were chosen based on brain data, which had lower wave amplitude and FA.

Inclusion Criteria	Equation	Parameter
Amplitude	$\lvert u\rvert > A\,\lvert \boldsymbol{U}\rvert_{median}$	$A = 1$
Fraction Anisotropy	$FA > FA_{thresh}$	$FA_{thresh} = 0.6$

After voxels are masked out based on the inclusion criteria, they were then sorted and further masked by the classification criteria used to sort them as either a "slow" or "fast" voxel. To be included in the analysis, the voxel must have a dominant shear wave polarization (be dominated by either a slow or fast shear wave – not both). A voxel was classified as a fast or slow shear wave voxel if the normalized displacement in the fast or slow polarization direction exceeded a minimum "polarization threshold" (pol_{thresh}) and the other component was below a corresponding maximum value ($1 - pol_{thresh}$). The normalized fast and slow shear wave displacement components are:

$$\widehat{\boldsymbol{U}}_{\boldsymbol{f}} = \frac{\boldsymbol{U}\cdot\boldsymbol{m_f}}{|\boldsymbol{U}|}, \tag{4.10}$$

$$\widehat{\boldsymbol{U}}_{\boldsymbol{s}} = \frac{\boldsymbol{U}\cdot\boldsymbol{m_s}}{|\boldsymbol{U}|}. \tag{4.11}$$

Thus a voxel would be designated as "fast" if $\widehat{U}_f > pol_{thresh}$ and $\widehat{U}_s < 1 - pol_{thresh}$, and a voxel is classified as "slow" if $\widehat{U}_s > pol_{thresh}$ and $\widehat{U}_f < 1 - pol_{thresh}$.

Voxels that did not meet either of these criteria were excluded from the anisotropic analysis. Table 4.2 outlines the classification criteria used for DF-LDI.

Table 4.2: Classification criteria for DF-LDI analysis

Classification Criteria for DF-LDI	Equation	Parameter
Polarization direction - slow	$\left\|\widehat{U}_s\right\| > pol_{thresh}$ $\left\|\widehat{U}_f\right\| < 1 - pol_{thresh}$	$pol_{thresh} = 0.7$
Polarization direction - fast	$\left\|\widehat{U}_f\right\| > pol_{thresh}$ $\left\|\widehat{U}_s\right\| < 1 - pol_{thresh}$	$pol_{thresh} = 0.7$

4.3.3.3 Directional Filtering with LDI (DF-LDI)

The apparent shear modulus ($\mu_{app} = \rho c^2$) was calculated using local direct inversion (LDI). The mean complex shear modulus ($\mu' + i\mu''$) for the simulations and mini-pig brain was estimated from the shear wave displacements using a viscoelastic analog of the Navier equation [1].

$$(\mu' + i\mu'')\nabla^2 \boldsymbol{U}(x, y, z) = -\rho\omega^2 \boldsymbol{U}(x, y, z) \qquad (4.12;\ \text{cf } 2.63)$$

This equation assumes that the material is linear, isotropic, and locally homogenous. The inversion was performed using a total-least squares fitting method where data was fit using a kernel size of $5 \times 5 \times 5$ voxels. Apparent shear modulus $\mu = |\mu' + i\mu''|$ was found at each voxel throughout the entire data set, and then classified as either slow ($\mu = \mu_s$) or fast ($\mu = \mu_f$) based on the slow and fast shear wave classification criteria for that voxel.

After LDI analysis, shear wave data were characterized by shear wave polarization, with each voxel classified as either slow or fast based on the slow and fast shear wave criteria. Directional filtering (using 192 filter directions) was used to identify average propagation direction, $\boldsymbol{n}$. Fiber direction, $\boldsymbol{a}$, was obtained from DTI and the angle θ between $\boldsymbol{n}$ and $\boldsymbol{a}$ was found. Polarization directions $\boldsymbol{m}_s = (\boldsymbol{n} \times \boldsymbol{a})/|\boldsymbol{n} \times \boldsymbol{a}|$ and $\boldsymbol{m}_f = \boldsymbol{n} \times \boldsymbol{m}_s$ were calculated, and the normalized slow and fast displacement ($\widehat{U}_s$ and $\widehat{U}_f$) components were used to classify voxels as either "slow" or "fast." The apparent shear moduli, μ_{app}, and angle, θ, can then be used in the multiple linear regression to estimate μ, $\mu\phi$ and $\mu\zeta$.

4.3.3.4 Parameter Estimation Using Multiple Linear Regression

Data from each classified voxel should satisfy either the slow or fast shear wave equation, which relates the apparent shear modulus for the slow or fast voxel to the material parameters of the NITI model.

$$\rho c_s^2 = \mu_s = \mu(1 + \phi \cos^2 \theta) \tag{4.13}$$

$$\rho c_f^2 = \mu_f = \mu + \mu\phi \cos^2 2\theta + \mu\zeta \sin^2 2\theta \tag{4.14}$$

The three unknown material parameters of an NITI model were estimated with the above equations for slow and fast shear waves using a multiple linear regression model of the form:

$$y = \beta_0 + \beta_1 x_1 + \beta_2 x_2. \tag{4.15}$$

The unknown parameters are $\beta_0 = \mu$, $\beta_1 = \mu\phi$ and $\beta_2 = \mu\zeta$. The dependent variable is the apparent shear modulus: $y = \mu_{app}$ ($\mu_{app} = \mu_s$ for slow waves and $\mu_{app} = \mu_f$ for fast shear waves). The independent variables in the multiple regression are defined in terms of the angle θ as follows:

$$x_1 = \begin{cases} \cos^2\theta & \text{("slow" voxels)} \\ \cos^2 2\theta & \text{("fast" voxels)} \end{cases} \text{ and } x_2 = \begin{cases} 0 & \text{("slow" voxels)} \\ \sin^2 2\theta & \text{("fast" voxels)} \end{cases}. \tag{4.16}$$

For the two simulations (NITI Cube and X-Box), all slow and fast voxels from all the cases in that simulation group were used to solve for the three unknowns. For the mini-pig data, each MRE dataset (one frequency in one animal) was used to estimate the baseline shear modulus (μ) for that set. The apparent shear modulus equations (Eq. 4.13 and 4.14) were divided by the baseline shear modulus and all data from one scan date (1-3 MRE datasets) were combined to solve for the shear anisotropy (ϕ) and tensile anisotropy (ζ). Final values for the anisotropic parameters were averaged between all cases. Because the brain displays viscoelastic behavior, appearing stiffer at higher strain rates, the shear modulus had to be estimated separately at each excitation frequency. A flow chart in Figure 4.7 outlines the main steps of DF-LDI.

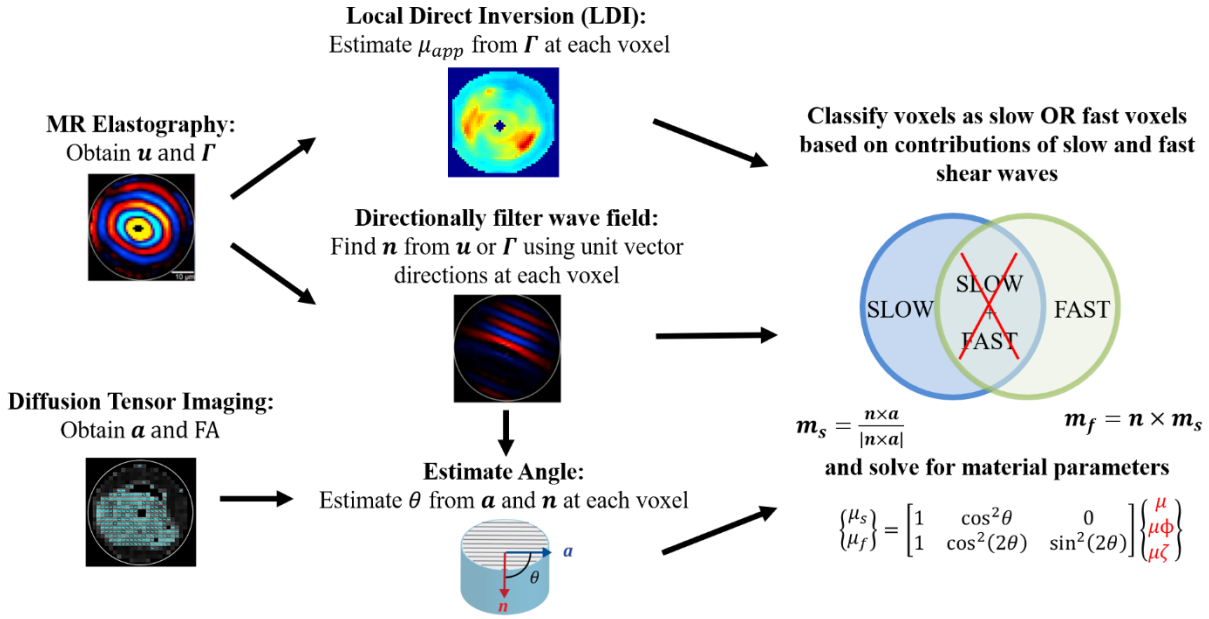

Figure 4.7: Flow chart outlining the steps of shear wave separation and anisotropic parameter estimation using DF-LDI.

4.4 Results

4.4.1 NITI Cube Results

The NITI Cube simulation output was shear wave displacement, which is like the output from an MRE scan. The fiber direction, $\boldsymbol{a}$, was treated as a known parameter. Figure 4.8 B and F depict the shear wave displacements of two cases where the fibers are at a 0° angle to the *x*-axis or *y*-axis. The classification of shear waves by polarization direction is also shown in Figure 4.8 C-D (*x*-axis) and G-H (*y*-axis). For all cases where the fiber direction is in the *x*-*z* plane and the actuation of the cube surface is along the *y*-axis, the resulting waves will be only slow shear waves (Figure 4.8 A-D). The opposite is true for all cases where the fiber direction is in the *y*-*z* plane and the actuation of the cube surface is along the *y*-axis, which results in only fast shear waves (Figure 4.8 E-H).

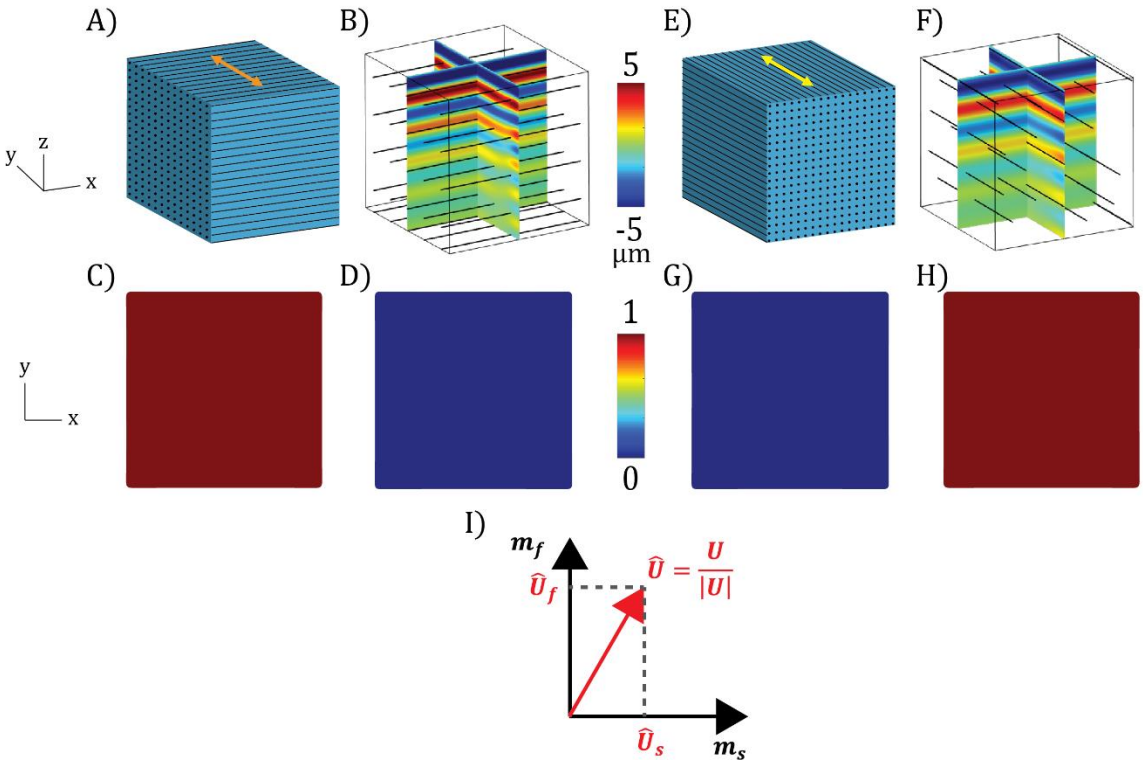

Figure 4.8: Simulation of NITI cube with fibers along the *x*-axis (A-D) and *y*-axis (E-H) at 100 Hz actuation. (A) Cube with fibers along the *x*-axis. Black lines represent the fiber direction. Actuation is along the *y*-direction on the top surface. (B) Shear wave displacements (w-component) on two perpendicular planes through the center of the cube. The black lines represent the fiber direction. (C) The normalized component of displacement in the slow polarization direction, $\hat{U}_s$, masked by displacement amplitude. The slice shown is the center slice along the *z*-axis. All the displacement for this simulation case is due to slow shear waves. (D) The normalized component of displacement in the fast polarization direction, $\hat{U}_f$, masked by displacement amplitude. Fast shear waves do not contribute much to the displacement field. (E) Cube with fibers along the *y*-axis. Black lines represent the fiber direction. Actuation is along the *y*-direction on the top surface. (F) Shear wave displacements (w-component) on two perpendicular planes through the center of the cube. The black lines represent the fiber direction. (G) The normalized component of displacement in the slow polarization direction, $\hat{U}_s$, masked by displacement amplitude. The slice shown is the center slice along the *z*-axis. Slow shear waves do not contribute to the displacement field for this case. (H) The normalized component of displacement in the fast polarization direction, $\hat{U}_f$, masked by displacement amplitude. All the displacement for this simulation case is due to fast shear waves. (I) Demonstration of the separation of vector $\hat{\boldsymbol{U}}$ into slow ($\hat{U}_s$) and fast ($\hat{U}_f$) shear wave components.

The angle between the propagation direction and the fiber direction, θ, was calculated for the simulation sets. Apparent shear modulus, μ_{app}, was calculated for the entire volume using LDI. All voxels were categorized as slow or fast (or neither) based on the criteria stated in Section 4.3.3 (Table 4.1 and Table 4.2). Figure 4.9 depicts θ and μ_{app} for all cases for either slow or fast waves. Since the case with fibers along the *x*-axis only has slow shear waves (shown in Figure 4.8 C-D) and the case with fibers along the *y*-axis only has fast shear waves (shown in Figure 4.8 G-H), only

the slow or fast components are shown for θ and μ_{app} for the cases in Figure 4.9. θ is consistent between the two groups (fibers in *x*-*z* plane and fibers in *y*-*z* plane) because all simulation cases have the same propagation direction. The weighting of θ for fibers in the *x*-*z* plane shows the effects of lower amplitude waves that did not match the inclusion criteria. The apparent shear modulus is larger for the cases where the fibers are in the *y*-*z* plane because the fibers (which are stiffer than the matrix) are being stretched by the wave motion.

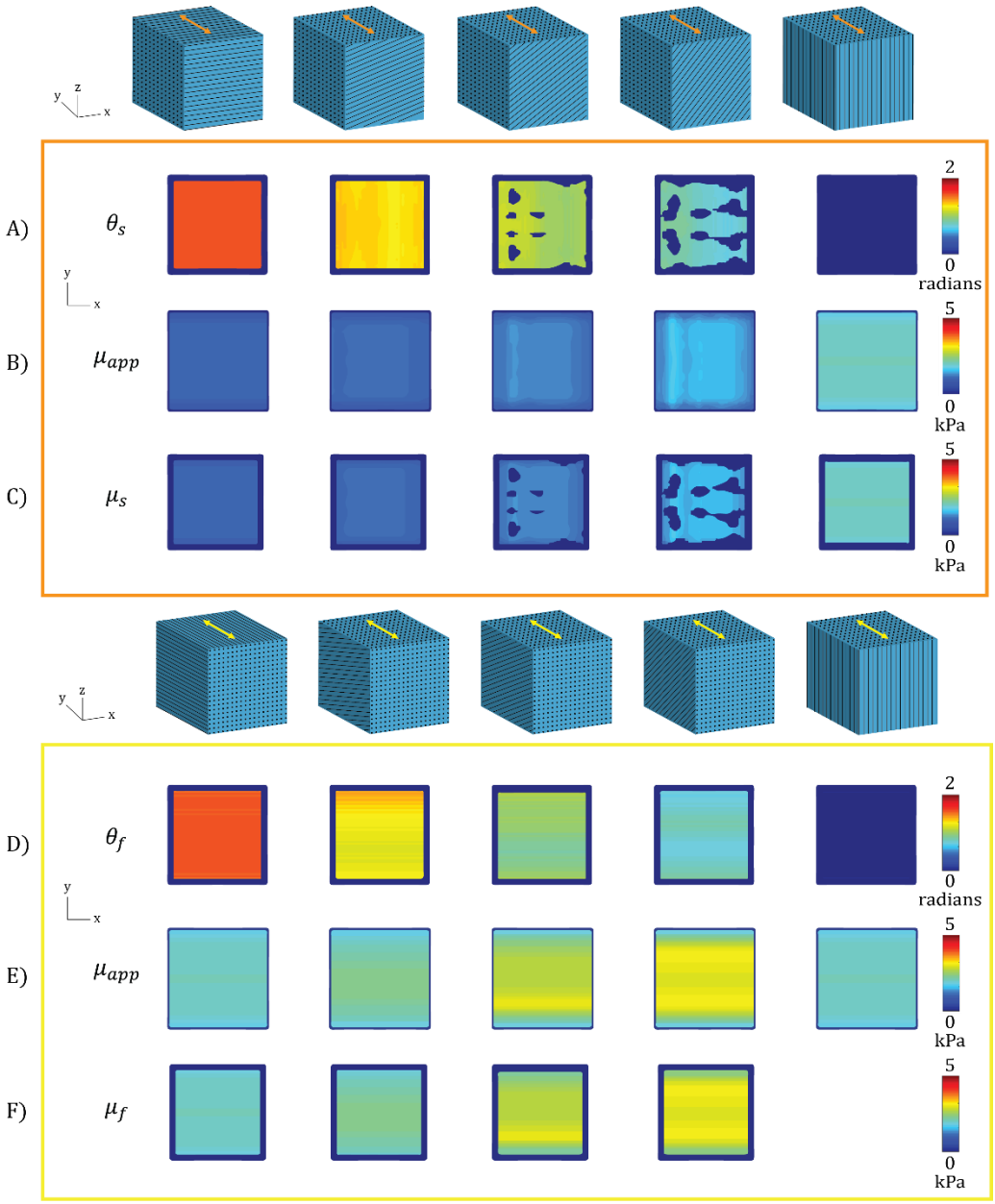

Figure 4.9: The angle between the propagation direction and fiber direction, θ, and the apparent shear modulus, μ_{app} for all NITI cube simulations. (A-C) Cubes with fibers along the *x*-axis. As shown in Figure 4.8, these cases only have slow shear waves. (A) Estimates of θ in voxels that were classified as slow based on the criteria (θ_s) are shown. All voxels that were not classified as slow are masked out (shown as dark blue). (B) The apparent shear modulus (μ_{app}) estimated using isotropic viscoelastic LDI. (C) Estimates of μ_{app} in voxels that were classified as slow (μ_s). All voxels not classified as slow were masked out (shown as dark blue). (D-F) Cube with fibers along the *y*-axis. As shown in Figure 4.8, these cases only have fast shear waves. (A) Estimates of θ in voxels that were classified as fast based on the criteria (θ_f) are shown. All voxels that were not classified as fast are masked out (shown as dark blue). (B) The apparent shear modulus (μ_{app}) estimated using isotropic viscoelastic LDI. (C) Estimates of μ_{app} in voxels that were classified as fast (μ_f). All voxels not classified as fast were masked out (shown as dark blue).

Once the voxels were classified as slow, fast, or eliminated, they were used to estimate the material properties using the linear regression model (Eq. 4.15) and statistics were performed using MATLAB's built-in linear regression model ("*fitlm*"). Figure 4.10 A depicts the apparent shear modulus in voxels classified as slow for all cases and Figure 4.10 B depicts apparent shear modulus in the voxels classified as fast for all cases.

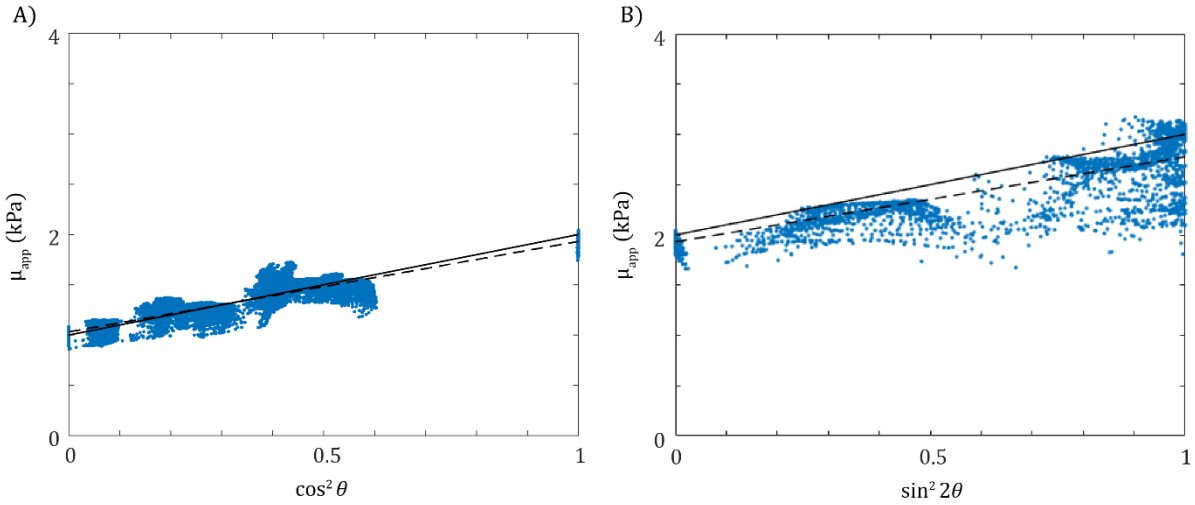

Figure 4.10: Apparent shear modulus of all voxels classified as "slow" (A) and "fast" (B) for all cases of the NITI cube. Each dot represents one voxel that met slow (A) or fast (B) criteria for DF-LDI analysis. The black solid line represents the linear relationship expected for the input parameters: $\mu = 1$ kPa, $\phi = 1, \zeta = 2$. The black dashed line represents the linear regression model for the estimated material parameters found using DF-LDI. (A) Apparent shear modulus in slow voxels for all simulation cases of the NITI cube. (B) Apparent shear modulus in fast voxels for all simulation cases of the NITI cube.

Table 4.3 shows the DF-LDI results of the anisotropic parameter estimation method for the cube. The input values are the simulation material parameter inputs. The estimated value is from the anisotropic estimation method.

Table 4.3: Comparison between exact values of the simulation parameters and the values estimated by DF-LDI for the NITI cubes using multiple linear regression. 367,635 voxels were used in the linear model fit (R^2=0.945). The p-value was less than machine precision. $\mu, \mu\phi,$ and $\mu\zeta$ are in units of kPa; ϕ and ζ are unitless. All standard errors were less than 0.08%.

	Input	**Estimated**	**% Error**
μ	1.00	1.03	3
$\mu\phi$	1.00	0.90	10
$\mu\zeta$	2.00	1.75	13
ϕ	1.00	0.87	13
ζ	2.00	1.69	15

4.4.2 X-Box Results

The X-Box Cube simulation output was shear wave displacement, which is like the output from an MRE scan. The fiber direction, $\boldsymbol{a}$, was treated as a known parameter. Figure 4.11 depicts the shear wave displacements of the three cases where the fibers are at a 45° angle. For X-Box all cases where the fibers undergo stretching during the actuation of the cube face, the resulting shear waves will be fast. This is seen in Figure 4.11 for the 45° case where the side face is actuated in the *y*-direction. For all X-Box cases where the fibers are unstretched during actuation, the resulting shear waves will be slow. This is seen in Figure 4.11 for the 45° case where the side face is actuated in the *x*-direction. When the top face is actuated in either the *x*- or *y*-direction, fibers in the X-Box cube will be both stretched and unstretched, resulting in a combination of slow and fast shear waves.

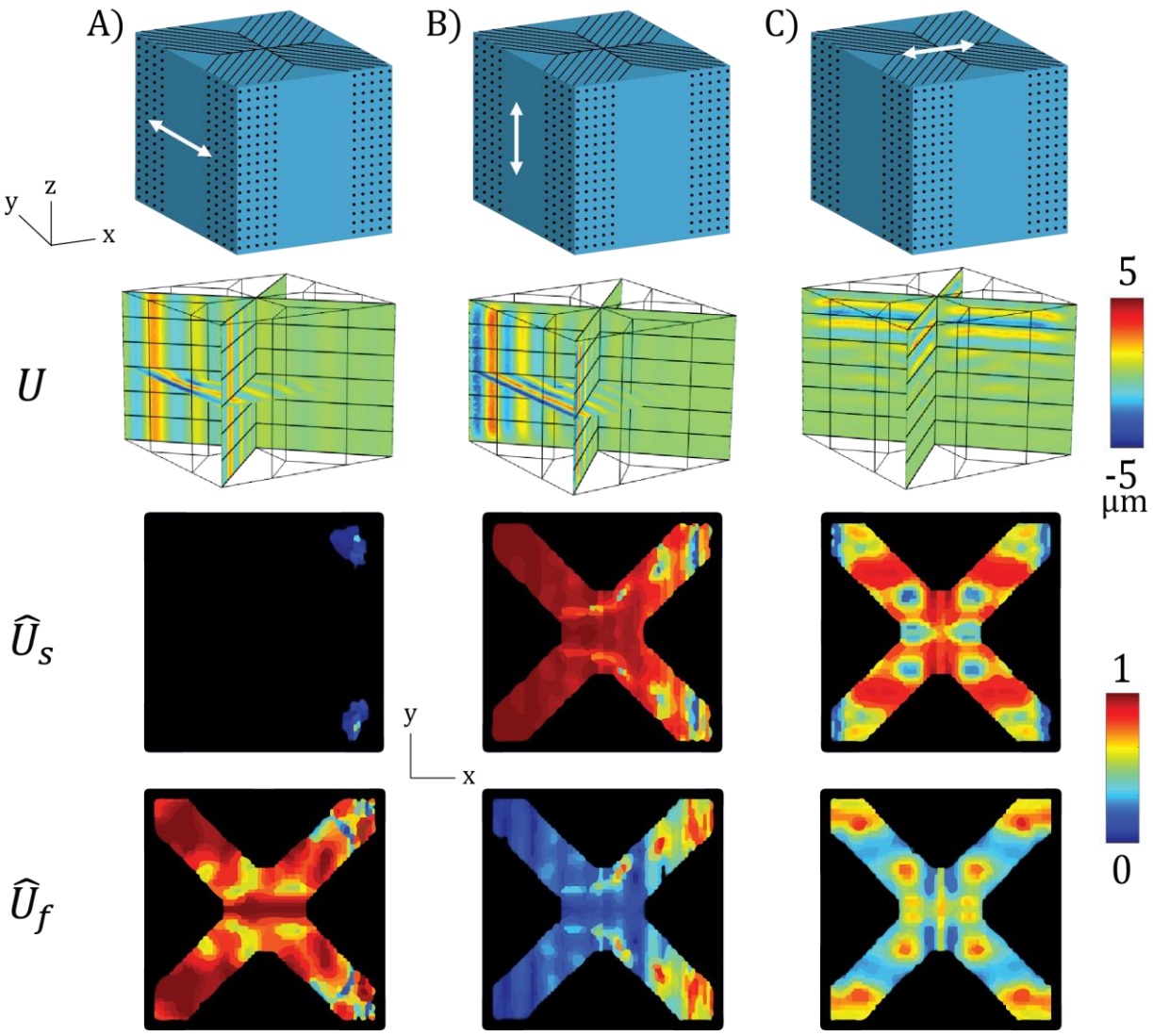

Figure 4.11: Shear wave displacement component in the x-direction (U) and normalized displacement component of slow and fast shear waves ($\widehat{U}_s$ and $\widehat{U}_f$) along planes for the three actuation directions of the 45° fiber X-Box case. (A) Actuation along the *y*-direction on the *y*-*z* face. (B) Actuation along the *z*-direction on the *y*-*z* face. (C) Actuation along the *x*-direction on the *x*-y top face. The top row shows the actuation directions on the 45° fiber X-Box simulation schematic. The second row shows the shear wave displacements (w-component) on perpendicular planes through the center of the cubes. The third row shows the normalized component of displacement in the slow polarization direction, $\widehat{U}_s$, masked by displacement amplitude. The slice shown is the center slice along the *z*-axis. Voxels that do not meet the inclusion and categorization criteria (Table 4.1 and Table 4.2) are shown in black. The fourth row shows the normalized component of displacement in the fast polarization direction, $\widehat{U}_f$, masked by displacement amplitude. The slice shown is the center slice along the *z*-axis. Voxels that do not meet the inclusion and categorization criteria (Table 4.1 and Table 4.2) are shown in black.

Figure 4.12 shows the angle between the propagation direction and fiber direction, θ, and the apparent shear modulus, μ_{app}, for the 45° case of the X-Box. Both the angle and apparent shear

modulus are also shown classified by shear wave polarization and masked by the inclusion criteria from Table 4.1. For this simulation, waves were only able to penetrate approximately half way through the cube before the amplitude was attenuated below the amplitude threshold. The two side-actuation cases produced either only slow or only fast shear waves, as shown in Figure 4.11. The top actuation causes a combination of slow and fast shear waves, so no voxels in that case met the classification criteria (Table 4.2).

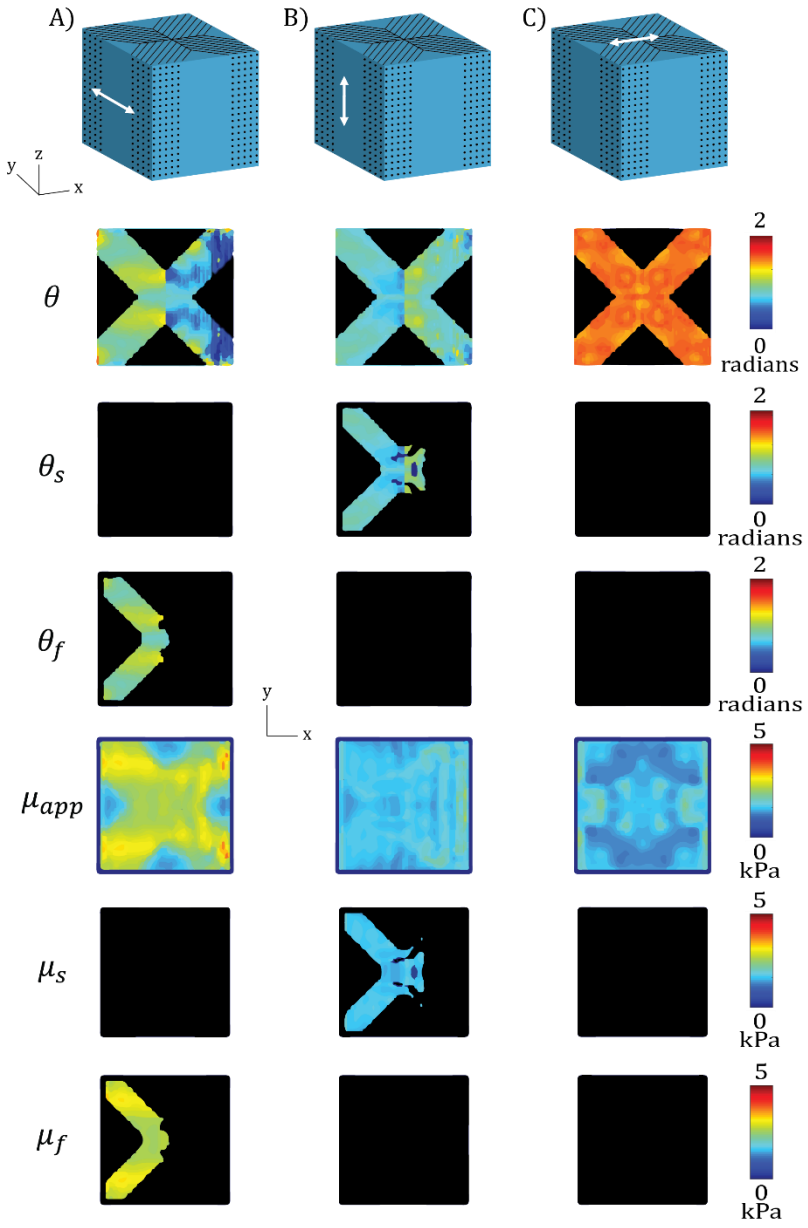

Figure 4.12: Angle and apparent shear modulus on central slice for the three actuation directions of the 45° fiber X-Box case. (A) Actuation along the *y*-direction on the *y*-*z* face. (B) Actuation along the *z*-direction on the *y*-*z* face. (C) Actuation along the *x*-direction on the *x*-y top face. The top row shows the actuation directions on the 45° fiber X-Box simulation schematic. The second row shows the angle between the propagation direction and fiber direction (θ). Voxels that do not meet the inclusion (Table 4.1) are shown in black. The third row shows estimates of θ in voxels that were classified as slow based on the criteria (θ_s). All voxels that were not classified as slow are masked out (shown as black). The fourth row shows estimates of θ in voxels that were classified as fast (θ_f). All voxels that were not classified as slow are masked out (shown as black). The fifth row shows the apparent shear modulus (μ_{app}) estimated using isotropic viscoelastic LDI. The sixth row shows the estimates of μ_{app} in voxels that were classified as slow (μ_s). All voxels not classified as slow were masked out (shown as black). The seventh row shows the estimates of μ_{app} in voxels that were classified as fast based on the inclusion criteria (μ_f). All voxels not classified as slow were masked out (shown as black).

Figure 4.13 depicts the apparent shear modulus in voxels classified as slow (A) and fast (B) for all X-Box cases. The black solid line represents the linear relationship expected for the input parameters: $\mu = 1$ kPa, $\phi = 1, \zeta = 2$. The black dashed line represents the linear regression model for the estimated material parameters found using DF-LDI.

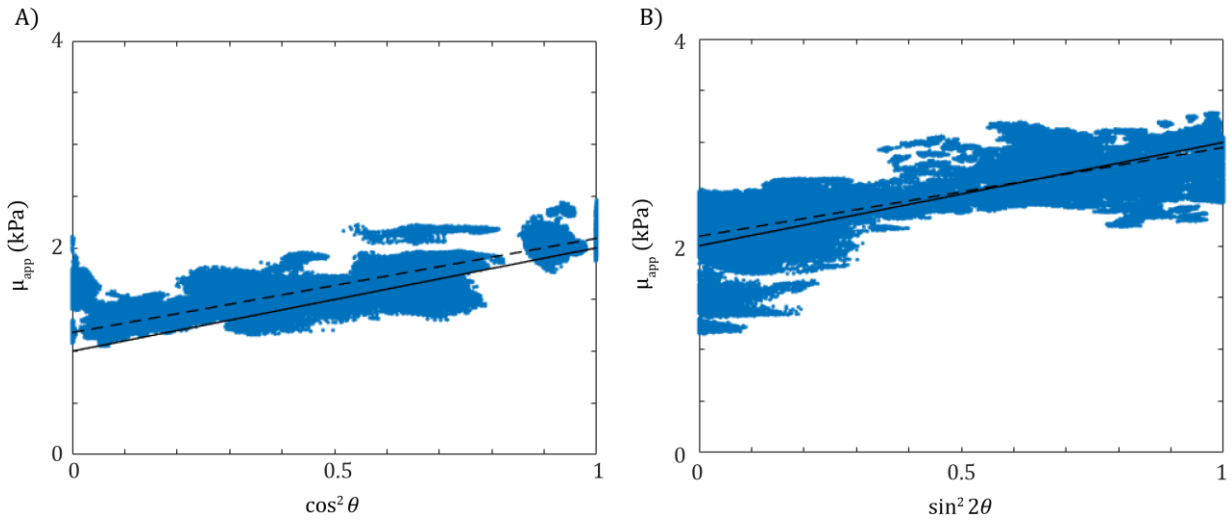

Figure 4.13: Apparent shear modulus of all voxels classified as "slow" (A) and "fast" (B) for all cases of the X-Box cube anisotropic material. Each dot represents one voxel that met slow (A) or fast (B) criteria for DF-LDI analysis. The black solid line represents the linear relationship expected for the input parameters: $\mu = 1$ kPa, $\phi = 1, \zeta = 2$. The black dashed line represents the linear regression model for the estimated material parameters found using DF-LDI. (A) Apparent shear modulus in slow voxels for all simulation cases of the NITI cube. (B) Apparent shear modulus in fast voxels for all simulation cases of the NITI cube.

Table **4.4** shows the results of the anisotropic parameter estimation method for the X-Box cube. The input values are the simulation material parameter inputs. The estimated value is from DF-LDI anisotropic estimation method.

Table 4.4: Comparison between exact values of the simulation parameters and the values estimated by DF-LDI for the X-Box using multiple linear regression. 629,269 voxels were used in the linear model fit (R^2=0.89). The p-value was less than machine precision. $\mu, \mu\phi,$ and $\mu\zeta$ are in units of kPa; ϕ and ζ are unitless. All standard errors were less than 0.075%.

	Input	**Estimated**	**% Error**
μ	1.00	1.18	18
$\mu\phi$	1.00	0.91	8
$\mu\zeta$	2.00	1.77	11
ϕ	1.00	0.77	23
ζ	2.00	1.50	25

4.4.3 Mini-pig Results

Shear wave displacement fields were calculated from the phase images from the MR-HUM scan (Chapter 2.3.1). Eigenvalues and eigenvectors of the diffusion tensor, which correspond principal diffusivity values and directions, were obtained from the DTI scan and used to estimate the fractional anisotropy (FA) (Eq. 2.58) and fiber direction ($\boldsymbol{a}$) in each voxel of the brain. Voxels were excluded from the estimation if they did not meet the inclusion criteria (Table 4.1). Voxels were classified as slow or fast, using the criteria defined in Table 4.2. Figure 4.14 A shows a sagittal anatomical slice of a porcine head that underwent MRE at 50 Hz and 100 Hz. The red line depicts the location of the coronal brain slice used in Figure 4.14 B-I and Figure 4.15. Figure 4.14 B shows the anatomical coronal slice and Figure 4.14 C depicts the fiber direction ($\boldsymbol{a}$) of the brain. Figure 4.14 D and G depict the amplitude-weighted propagation direction ($\boldsymbol{n}$) at 50 and 100 Hz. Figure 4.14 E-F show the slow (E) and fast (F) polarization directions at 50 Hz. Figure 4.14 H-I show the slow H) and fast (I) polarization directions at 100 Hz. All the waves are propagating from the skull to the inner part of the brain. There is a slight difference in propagation direction between

the 50 Hz and 100 Hz cases. This is slightly more pronounced in the slow and fast polarization directions. The different shear wave directions among the different frequencies enabled the anisotropic estimation.

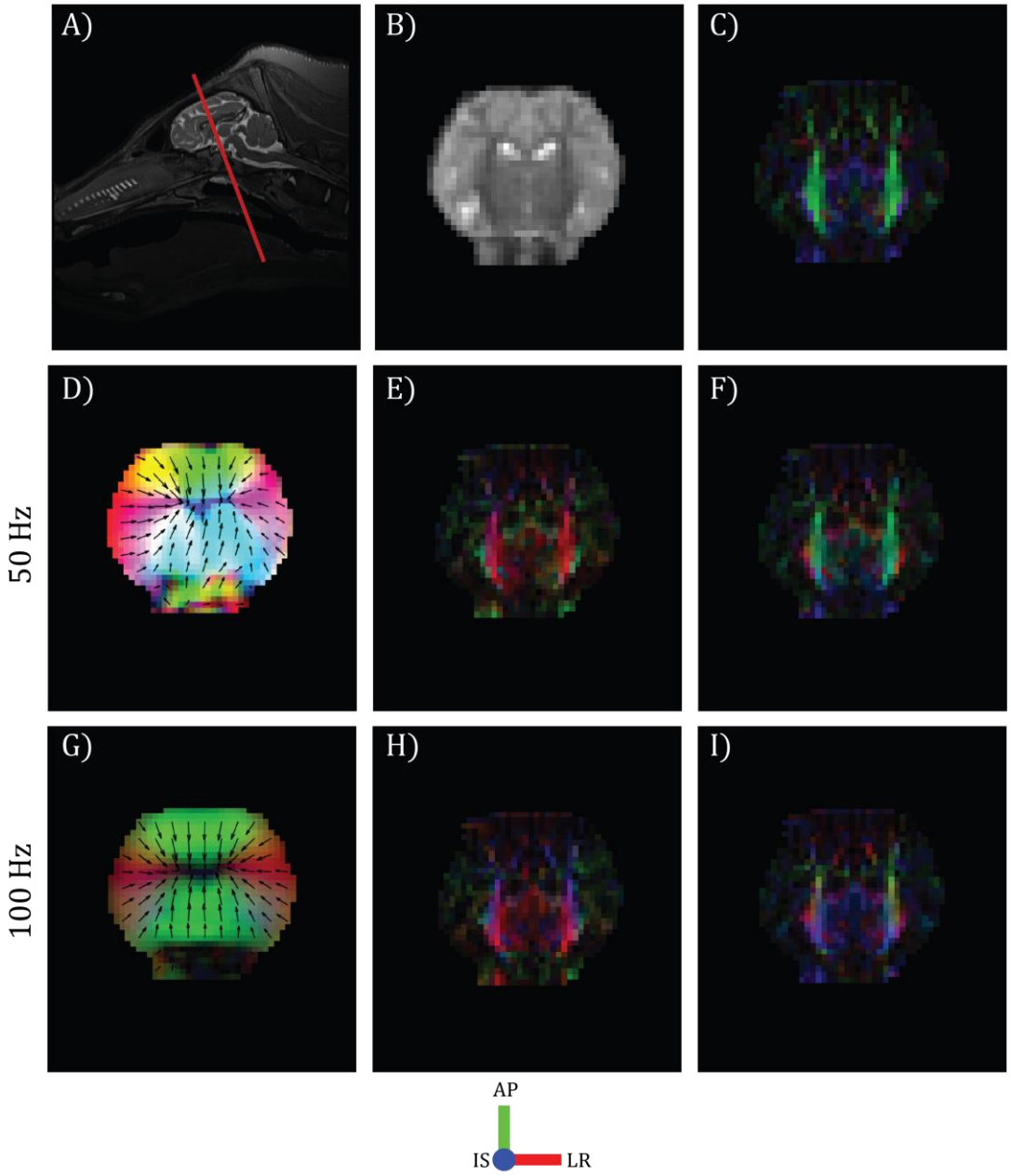

Figure 4.14: Experimental measurements of fiber direction, propagation direction and slow / fast shear wave polarization directions from mini-pig data. In panels (C-I) colors represent directions, where red = left-right (LR); green = anterior-posterior (AP); blue = inferior-superior (IS). (A) Sagittal anatomical slice of a porcine head that underwent MRE at 50 Hz and 100 Hz. The red line depicts the location of the coronal brain slice used in B-I and Figure 4.15. (B) MRE magnitude coronal slice of the mini-pig brain. (C) Fiber direction ($\boldsymbol{a}$) calculated using DTI. (D) Amplitude-weighted propagation direction ($\boldsymbol{n}$) at 50 Hz for coronal slice.). (E) Slow wave polarization direction at 50 Hz for coronal slice. (F) Fast wave polarization direction at 50 Hz for coronal slice. (G) Amplitude-weighted propagation direction ($\boldsymbol{n}$) at 100 Hz for coronal slice. (H) Slow wave polarization direction at 100 Hz for coronal slice.). (I) Fast wave polarization direction at 100 Hz for coronal slice.

Figure 4.15 A-B and D-E show the contributions of slow versus fast shear waves for one coronal slice of a mini-pig brain at 50 and 100 Hz. For this slice, there are more voxels classified as slow shear wave voxels at 100 Hz and more voxels classified as fast shear wave voxels at 50 Hz. Figure 4.15 C and F show the apparent shear modulus (μ_{app}) for the same coronal slice calculated using LDI from the 50 and 100 Hz data. The brain appears to be stiffer at 100 Hz.

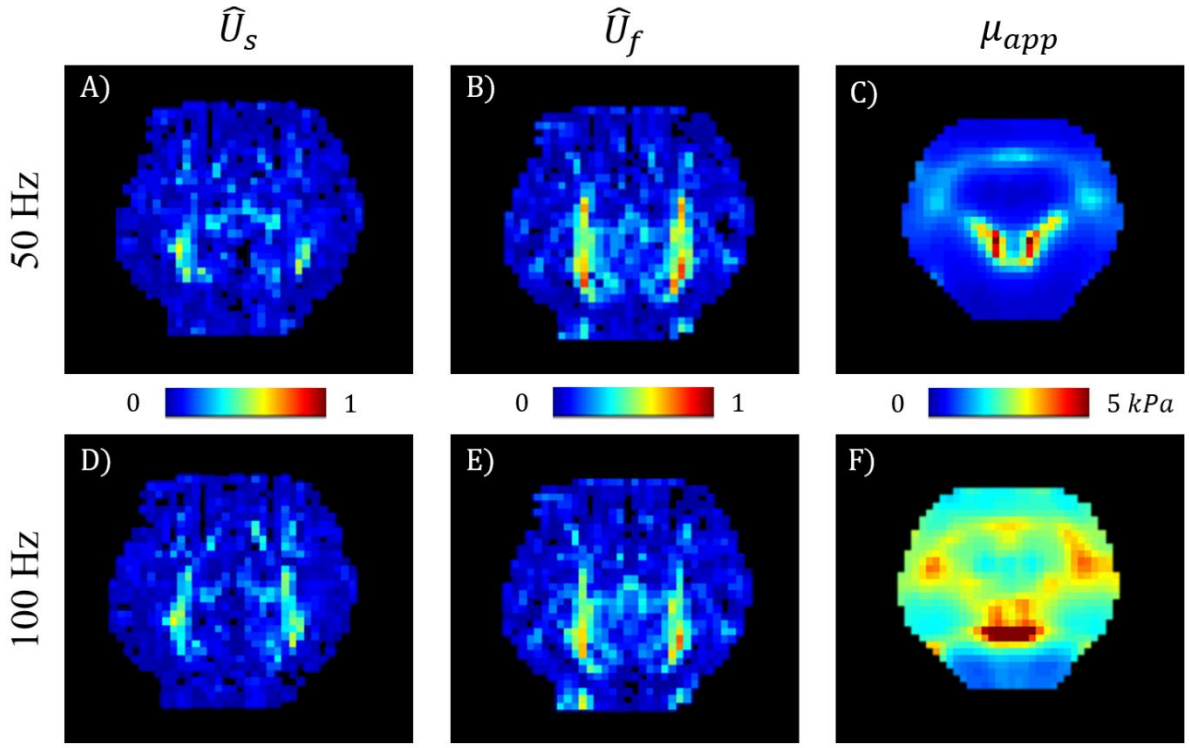

Figure 4.15: Experimental estimates of slow and fast shear wave participation, and apparent shear modulus, from mini-pig data, analyzed using DF-LDI. The coronal slice corresponds to the red line in Figure 4.14 A. Voxels that do not meet the inclusion criteria (Table 4.1) were removed during masking (black). (A) The normalized component of displacement in the slow polarization direction, $\widehat{U}_s$ for 50 Hz MRE. (B) The normalized component of displacement in the fast polarization direction, $\widehat{U}_f$ for 50 Hz MRE. (C) The apparent shear modulus (μ_{app}) calculated by isotropic viscoelastic LDI using 50 Hz MRE data. (D) The normalized component of displacement in the slow polarization direction, $\widehat{U}_s$ for 100 Hz MRE. (E) The normalized component of displacement in the fast polarization direction, $\widehat{U}_f$ for 100 Hz MRE. (F) The apparent shear modulus (μ_{app}) calculated by isotropic viscoelastic LDI using 100 Hz MRE data.

Mean values for the baseline shear modulus increased with increasing frequency (Figure 4.16 A). Mean values ($\pm\, std$) of shear anisotropy ($\phi = 0.12 \pm 0.38$) and tensile anisotropy ($\zeta = 0.17 \pm 0.27$) were positive, which means that the brain tissue appeared slightly stiffer, on average, in

shear in planes containing the fiber axis (vs the plane normal to the fiber axis) and stiffer in tension along the fiber axis (relative to tension normal to the fiber axis) (Figure 4.16 B-C). The apparent modulus of the white matter of the mini-pig brain could be described by the uniform ITI model with an RMS error of 19 ± 12%. The fraction of variance in white matter modulus explained by directional dependence (non-zero ϕ and ζ) was 4.5 ± 3.5%.

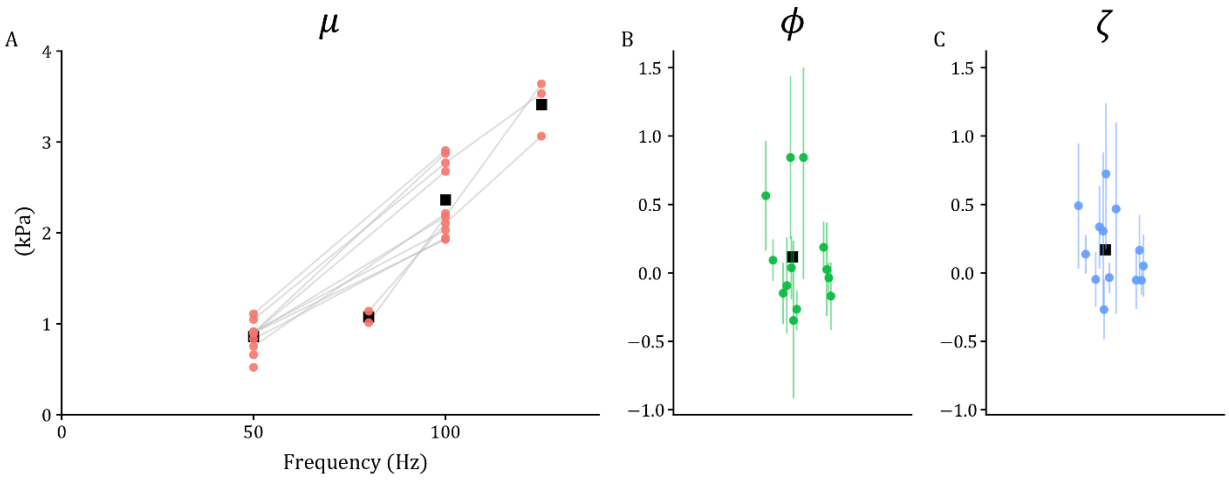

Figure 4.16: Results of DF- LDI anisotropic parameter estimation for all porcine brains. (A) Estimates of μ for MRE data performed at different frequencies. Gray lines connect the data from the MRE scans of one mini-pig on the same day. (B) Estimates of ϕ for the porcine brain from each scan days (n=13) with 95% confidence intervals. MRE data taken at different frequencies was normalized and combined to find ϕ. A black square shows the mean value. (C) Estimates of ζ for the porcine brain from each scan days (n=13) with 95% confidence intervals. MRE data taken at different frequencies was normalized and combined to find ζ. A black square shows the mean value.

4.5 Discussion and Conclusions

In this chapter I introduce a method to estimate parameters of the ITI material model and applied it to numerical data from simulations of waves in two domains (a uniform NITI Cube and a heterogeneous X-Box) and to experimental data from MRE in the mini-pig. This method is based on the theory of waves in a uniform, infinite domain. Application of the method to the NITI cube led to the best estimates because it was the only uniform domain. By adding heterogeneity

(crossing fiber tracts) to the X-Box simulation, the assumption of uniformity was directly violated. With increasing spatial complexity of fiber tracts, the accuracy of this method will decrease.

The implementation of this method in this Chapter also assumes that all fibers have identical properties, in order to include data from all voxels in the fitting process. Although this is true for the simulations, this is not necessarily true for the white matter in the mini-pig brain. To better model the mini-pig brain, a more accurate inversion method is necessary. The LDI inversion used does not account for anisotropy or heterogeneity. For example, an anisotropic, inverse finite element method, in which the parameters are updated until simulation matches experiment, could provide improved anisotropic parameter estimation.

The resolution of the mini-pig data was limited by the resolution of the wavelength estimates, which in turn depend on the wavelength itself. To improve the resolution and accuracy of MRE estimates, it would be helpful to produce shear waves with shorter wavelengths in larger, aligned white matter tracts.

All waves were induced by external excitation. Waves induced by boundary excitation generally travel inwards. It is difficult to control the generation of slow and fast shear waves to optimize the mix of wave types and angles for improved data analysis. A method to excite waves from inside the sample could provide experimental data that are better suited to estimation of anisotropic material parameters.

Mild anisotropy (small positive values of ϕ and ζ) may explain some variations in apparent modulus of WM in the mini-pig. Other factors that contribute to variations probably include true

heterogeneity of WM properties. Future work should investigate both anisotropy and heterogeneity of WM, using more sophisticated actuation strategies and inversion techniques.

4.6 Summary

This chapter introduces an anisotropic parameter estimation method and describes its application to two simulation sets of different complexity and MRE data from the mini-pig brain. Although this method shows promise in its ability to find anisotropic parameters, the approach and/or analysis could be improved. Enhanced control over the direction of wave propagation would enable control over resulting shear wave types. Localizing the wave field (exciting waves in a small region) could improve the local estimates in smaller areas of white matter or other anisotropic, heterogeneous tissues. The next chapter describes an alternative approach to anisotropic MRE that meets some of these objectives.

Chapter 5: Magnetic resonance imaging of harmonic shear waves induced by focused ultrasound

5.1 Overview

As noted in previous chapters, estimation of anisotropic material parameters is important, but challenging. While the results of anisotropic MRE in Chapter 4 are promising, a few key challenges remain. Accurate estimation of anisotropic parameters requires shear waves with multiple propagation and polarization directions [31]. Also, shear wavelengths need to be short relative to the tissue sample size. Both requirements are difficult to achieve using conventional actuation methods. The approach presented in this chapter solves some of the challenges of anisotropic parameter estimation by using focused ultrasound (FUS) to generate harmonic shear waves for anisotropic MRE.

Acoustic radiation force at the focus of the ultrasound beam can be varied harmonically to induce shear waves. These shear waves can be imaged using standard MRE pulse sequences. MR imaging of harmonic, ultrasound-induced motion (MR-HUM) enables excitation of shear waves with multiple propagation and polarization directions and excitation of short wavelengths so small areas of interest can be investigated. This chapter summarizes the development and application of MR-HUM methods, which will provide the platform for future analysis of anisotropic materials using this approach.

5.2 Objective and Significance

Despite the prevalence of anisotropy in soft tissues like brain and muscle, anisotropic mechanical properties of soft materials are still an active area of research due to the challenges of anisotropic property estimation. Anisotropic material models have been explored in theoretical studies [84], ultrasound elastography [85-88], and anisotropic MRE [29, 58, 75-82]. However, most of these studies either lack experimental data or do not consider the effects of tensile anisotropy [30].

According to prior work, to accurately estimate the three material properties for an ITI material, both slow and fast shear waves must be present with significant amplitudes and multiple directions [31]. However, obtaining both slow and fast shear waves in soft tissues and in multiple directions at reasonable amplitude is challenging. Previous experiments investigating anisotropy using slow and fast shear waves require multiple experimental setups and samples to estimate all three parameters [30]. To perform anisotropic MRE using only one sample, multiple shear waves directions can be induced by varying frequency (as seen in the previous chapter) or actuator placement [83]. However, these methods may not provide a large variety of different shear waves due to the lack of control of tissue motion provided by boundary actuation. Boundary actuation is noninvasive but produces shear waves that are generally uncontrolled in direction and vulnerable to attenuation. Direct (invasive) actuation, which uses an embedded needle or rod ("stinger") to produce shear waves, can produce higher amplitude waves in the tissue, but it is destructive, so actuating in multiple directions is not possible due to cumulative damage to the sample [30]. In principle, ultrasound elastography is noninvasive and incorporates the ability to actuate in multiple directions, but it does not provide the 3D displacement fields necessary to fully characterize material behavior.

In addition to the requirement for multiple propagation directions, it may be beneficial to perform anisotropic parameter estimation locally (within a small sample volume) and avoid issues related to heterogeneity. In some biological tissues, like white matter in the brain, the dimensions of the heterogeneous tissues are relatively small. For anisotropic MRE, accurate parameter estimation requires a small wavelength (high frequency). Boundary actuation, especially at high frequencies, is susceptible to attenuation, so tissue far from the boundary will not be vibrated at high amplitudes (as seen in the previous chapter). Ultrasound elastography, which has low resolution, is also not ideal for small sample volumes.

In summary, the problems with existing actuation methods for anisotropic parameter estimation are: (i) Boundary actuation is noninvasive, but it has uncontrolled propagation and polarization directions and high attenuation, especially at high frequencies. (ii) Direct internal actuation is invasive and does not allow for multiple propagation directions per sample. (iii) Ultrasound elastography is low resolution and does not provide a 3D displacement field. To meet the requirements of anisotropic estimation, another method of actuation is necessary.

Focused ultrasound (FUS) can be used to produce shear waves in a tissue for elastography. It can be used for acoustic radiation force imaging (MR-ARFI) [52, 62], transient MRE (t-MRE) [65], harmonic motion imaging (HMI) [48, 96], mpARFI [63], and MR imaging of harmonic ultrasound-induced motion (MR-HUM). Several of these techniques (MR-ARFI, t-MRE, mpARFI, MR-HUM) combine ultrasound-generated pulses with MRI imaging. HMI uses only ultrasound for both amplitude-modulated harmonic actuation and data recording. MR-HUM uses amplitude-modulated (AM) harmonic ultrasound for actuation and MRE sequences for data recording. AM waveforms are created from the multiplication of a carrier frequency (of the

ultrasound transducer) and modulation frequency (desired tissue harmonic motion). This time-varying, unidirectional force causes tissue displacement; force can be varied in magnitude by adjusting the power of the ultrasound device.

MR-HUM can overcome several challenges of anisotropic MRE by noninvasively producing and imaging shear waves with multiple propagation and polarization directions, with small enough wavelengths to produce local estimates of material parameters.

5.3 Methods

MR-HUM was performed on two sample types: gelatin-glycerol gel and chicken breast. The gelatin sample was used for an isotropic MRE inversion comparison between two actuation methods: conventional direct (piezoelectrically-driven) actuation [30] and MR-HUM. Chicken breast samples were used to test the ability to create multiple propagation and polarization directions in one sample. Scans were performed on an Agilent/Varian DirectDrive 4.7T small-bore animal MRI scanner at room temperature (~21°C) using a custom high intensity focused ultrasound (HIFU) system (Image Guided Therapy, Pessac, France).

5.3.1 Gelatin Sample Preparation

MR-HUM samples: Gelatin mixture, consisting of food grade gelatin (Knox) and 50:50 water:glycerol [1] was solidified in a 50 mL tube lubricated with canola oil. The sample was refrigerated between fabrication and testing. The sample was removed from the refrigerator at least 2 hours before testing to allow it to reach room temperature. Prior to imaging, the sample was removed from the 50 mL tube and inserted into a modified 50 mL tube with a cut window to allow for ultrasound penetration. A water-filled bladder provided an air-free connection between the US

transducer and the surface of the gelatin. The tube and sample were then placed in a 30 mm diameter coil for scanning. Figure 5.1A shows the schematic of the gelatin sample for MR-HUM.

Directly-excited samples: A gelatin mixture of the same proportions was solidified in a 48 mm cylinder container. The sample was refrigerated between fabrication and testing. Before testing, it was removed from the refrigerator so that it could reach room temperature. A piezoelectric actuator (Model APA100M-NM, CEDRAT Technologies, Meylan, France) powered by an amplifier (EPA 105, Piezo Systems Inc.) was used to harmonically actuate the gelatin [30] via a 1 mm diameter titanium rod, inserted in the center of the sample (axial excitation). Figure 5.1B shows the schematic of the gelatin sample for piezoelectric actuation.

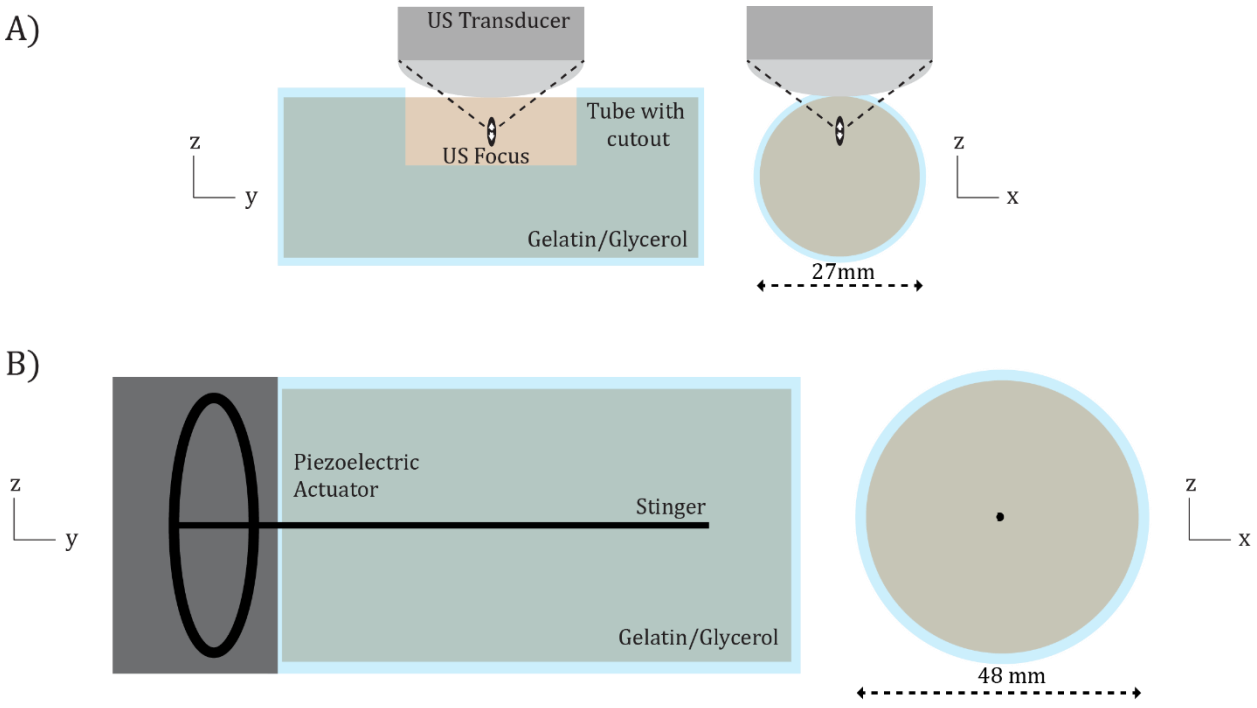

Figure 5.1: (A) Schematic of the gelatin sample for MR-HUM. The sample was placed in a tube with a cutout window to allow for US penetration. (B) Schematic diagram of the gelatin sample for with direct excitation of shear waves with embedded axial rod driven by a piezoelectric actuator.

5.3.2 Chicken Sample Preparation

Chicken breast purchased from a local grocery store was frozen within one day of purchase. For sample preparation, the chicken breast was removed from the freezer to thaw in room temperature for ~1 hour. Once the tissue was partially thawed, a 1" circular hole punch (McMaster Carr, part 3427A24) was used to cut cylindrical samples from the chicken breast (Figure 5.2A). Samples were placed in a gelatin mixture [1] inside a 50 mL tube, lubricated with canola oil (Figure 5.2B). The sample was then refrigerated until testing. Prior to testing, the chicken/gel sample was removed from the 50 mL tube and inserted into a modified 50 mL tube with a 25 x 25 mm window to allow for ultrasound penetration. This tube was then placed in a 30 mm diameter coil for scanning (Figure 5.2C). The ultrasound transducer was placed above the surface of the chicken (Figure 5.2D). A water-filled bladder attached to the transducer provided an air-free connection.

The focus of the ultrasound transducer was electronically moved to be 2 mm below the natural focus so that actuation could occur deeper into the chicken sample. Figure 5.2E shows the schematic of the setup.

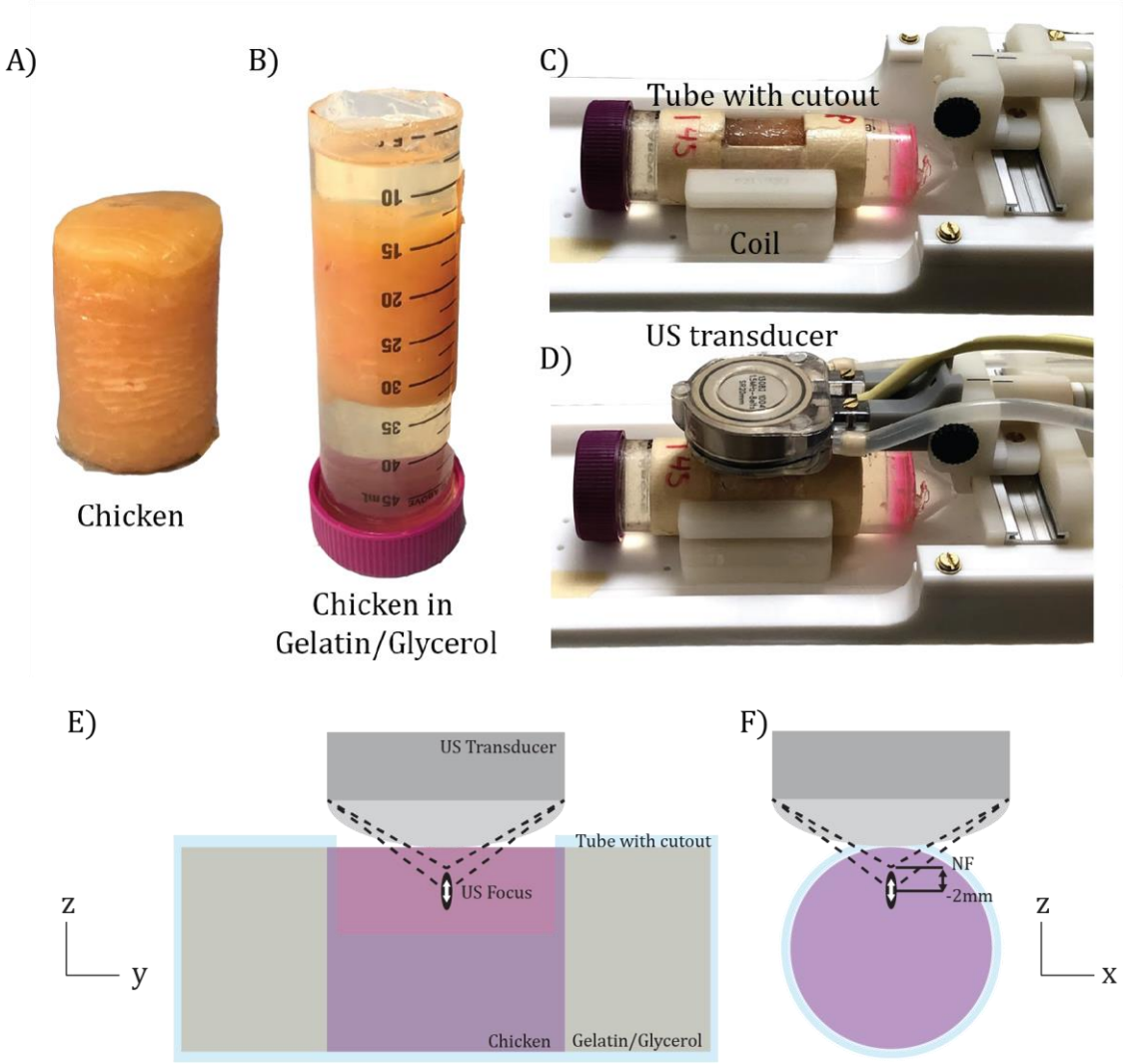

Figure 5.2: Sample preparation and schematic for MR-HUM scan setup. (A) 1" diameter cylindrical punch of chicken breast. Sample was punched after partial thawing for ~1 hour. (B) Sample embedded in gelatin/glycerol mixture for testing. (C) Chicken sample in gel is moved to a 50 mL tube with a cutout window for testing. The tube is placed in the 30 mm diameter coil with the cutout facing upwards. (D) the ultrasound (US) transducer is placed above the sample. A water bladder covering the US transducer provides a good connection to the sample. The sample can be rotated while still maintaining the connection between the US transducer and the sample. (E-F) Schematic of MR-HUM at two orientations. Focus is 2 mm down from the natural focus (NF).

During testing, the sample could be rotated in the coil while the ultrasound transducer remained stationary, as long as the water-filled bladder coupling the sample to the transducer remained in the tube cutout area (Figure 5.3). The sample rotation controlled the angle between the chicken fibers to the ultrasound actuation. For this experiment, each chicken sample underwent two MR-

HUM scans with actuation at angles approximately 45° and 90° to the fiber direction. A total of 11 samples of chicken were actuated at 400 Hz at ~1.5 W power from the ultrasound transducer.

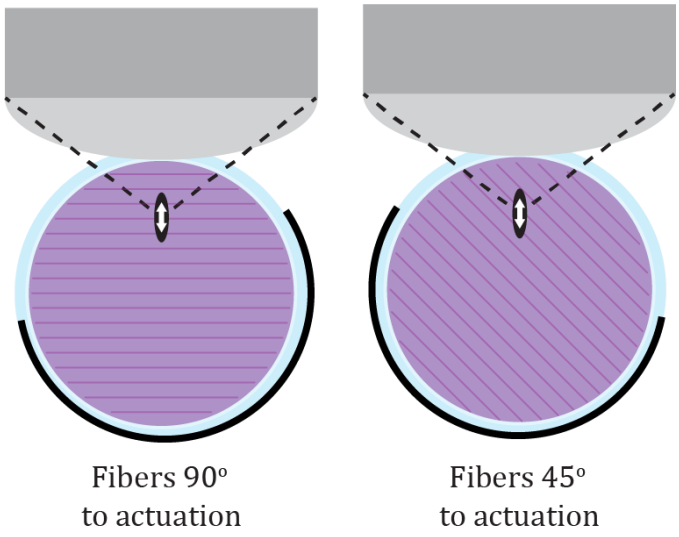

Figure 5.3: The sample could be rotated within the coil to change the angle between the fibers and direction of actuation (β). The transducer and focal region of the US beam remained stationary. Samples underwent actuation at angles approximately $\beta = 90°$ and $\beta = 45°$ to the chicken fibers.

5.3.3 Imaging

5.3.3.1 MR-HUM

Shear waves were excited at 300 Hz (gelatin) or 400 Hz (chicken) using magnetic resonance imaging of ultrasound-induced motion (MR-HUM). The tissue was harmonically oscillated by acoustic radiation force of the focused ultrasound beam. The ultrasound transducer produced a signal at 1500 kHz. This signal was modulated by a square wave at 300 Hz (gelatin) or 400 Hz (chicken) to generate amplitude modulated focused ultrasound, which produced shear waves at the frequency of the modulation signal. Figure 5.4 outlines the amplitude modulation used in MR-HUM.

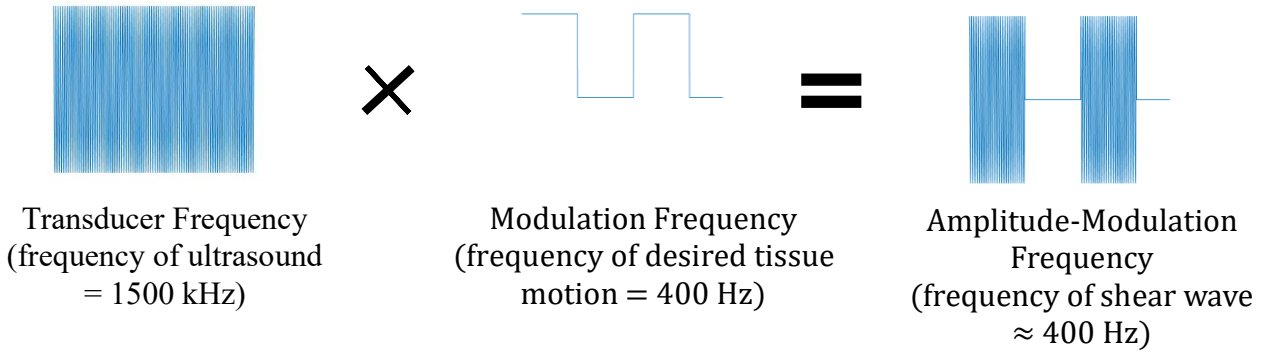

Figure 5.4: Amplitude modulation of focused ultrasound at 400 Hz. High frequency of ultrasound is modulated by low frequency to produce amplitude modulation, resulting in shear waves at the low frequency.

Gelatin: MRE data were acquired with a modified 2D multi-slice spin-echo sequence [117] with 1 mm isotropic voxels, TR = 1000 ms, and TE = 36 ms covering a volume of 32 x 32 x 27 mm^3. Sinusoidal motion encoding gradients (1-3 cycles) of amplitude 20 G/cm were synchronized with motion to induce phase contrast proportional to displacement.

Chicken: MRE data were acquired with a modified 2D multi-slice spin-echo sequence [117] with 1 mm isotropic voxels, TR = 1000 ms, and TE = 33-34 ms covering a volume of 32 x 32 x 12 mm^3 or 24 x 24 x 12 mm^3. Sinusoidal motion encoding gradients (1-3 cycles) of amplitude 20 G/cm were synchronized with motion to induce phase contrast proportional to displacement.

MRE data were phase-unwrapped and rigid body motion effects were removed. During analysis, imaging data was masked at 10 mm radius from the center of actuation because MR-HUM shear waves dissipate quickly from the focal region.

5.3.3.2 Direct actuation MRE

Shear waves are excited at 300 Hz using a piezo electric actuator. MRE data were acquired with a modified 2D multi-slice spin-echo sequence with 1 mm isotropic voxels, TR of 1000 ms, and TE of 36 ms covering a volume of 48 x 48 x 21 mm^3. Sinusoidal motion encoding gradients (1-3

cycles) of amplitude 8 G/cm were synchronized with motion to induce phase contrast proportional to displacement. MRE data were phase-unwrapped and rigid body motion effects were removed.

5.3.3.3 Diffusion Tensor Imaging

DTI was performed for all chicken samples at all orientations tested. Diffusion tensors were estimated using 30 diffusion-weighted directions and 2 averages. The scan used 2 mm isotropic voxel resolution over an imaging volume of 48 x 48 x 15 mm^3. Fractional anisotropy (FA) was estimated from diffusion tensor eigenvalues, and fiber direction ($\boldsymbol{a}$) was estimated from the first principal eigenvector.

5.4 Results

5.4.1 Gelatin Samples

Wave patterns in the two gelatin samples for both methods of actuation were consistent with isotropic material model. Waves in sample imaged using MR-HUM had a spherical pattern, while waves from the piezoelectric actuator were cylindrical. Figure 5.5 (A and C) shows the shear waves (w-component) for both actuation methods.

Shear modulus was estimated using an isotropic viscoelastic material model for LDI with a kernel size of 5 mm [1]. Figure 5.5 (B and D) shows the shear moduli for both actuation methods. The mean storage modulus for the entire masked regions of two samples were 3.6 ± 0.3 kPa for piezo actuation and 3.4 ± 0.3 kPa for MR-HUM.

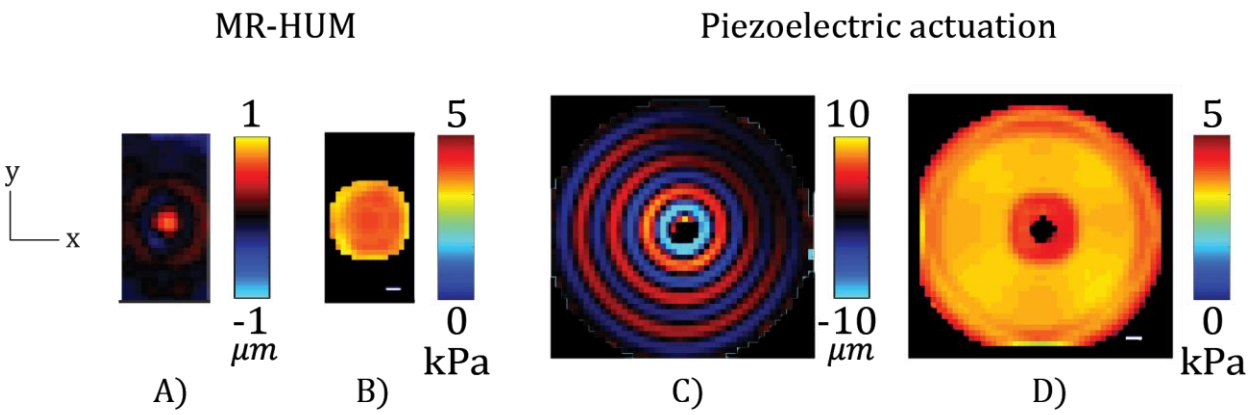

Figure 5.5: Shear waves and shear moduli of gelatin using MR-HUM (A-B) and piezoelectric actuation (C-D) at 300 Hz. (A) Shear waves (w-component) for one slice near the focus. (B) Shear modulus in a region within 8 mm radius of the center (surrounding material has been masked out). White scale bar represents 3mm. (C) Wave field for piezoelectric actuation. Note the higher amplitude of motion for shear waved excited using piezoelectric actuation. (D) Shear modulus estimates in piezoelectically-excited sample. White line represents 3mm.

5.4.2 Chicken Sample

Fiber direction was estimated using DTI as described above. The data was masked to show only the region of chicken that was within 10 mm radius of the focal region. Figure 5.6 shows the sample area in the dotted line and fiber directions from one sample with fibers at 51° and 87° to the actuation direction. Fiber direction in the samples show fibers with a consistent, clear orientation.

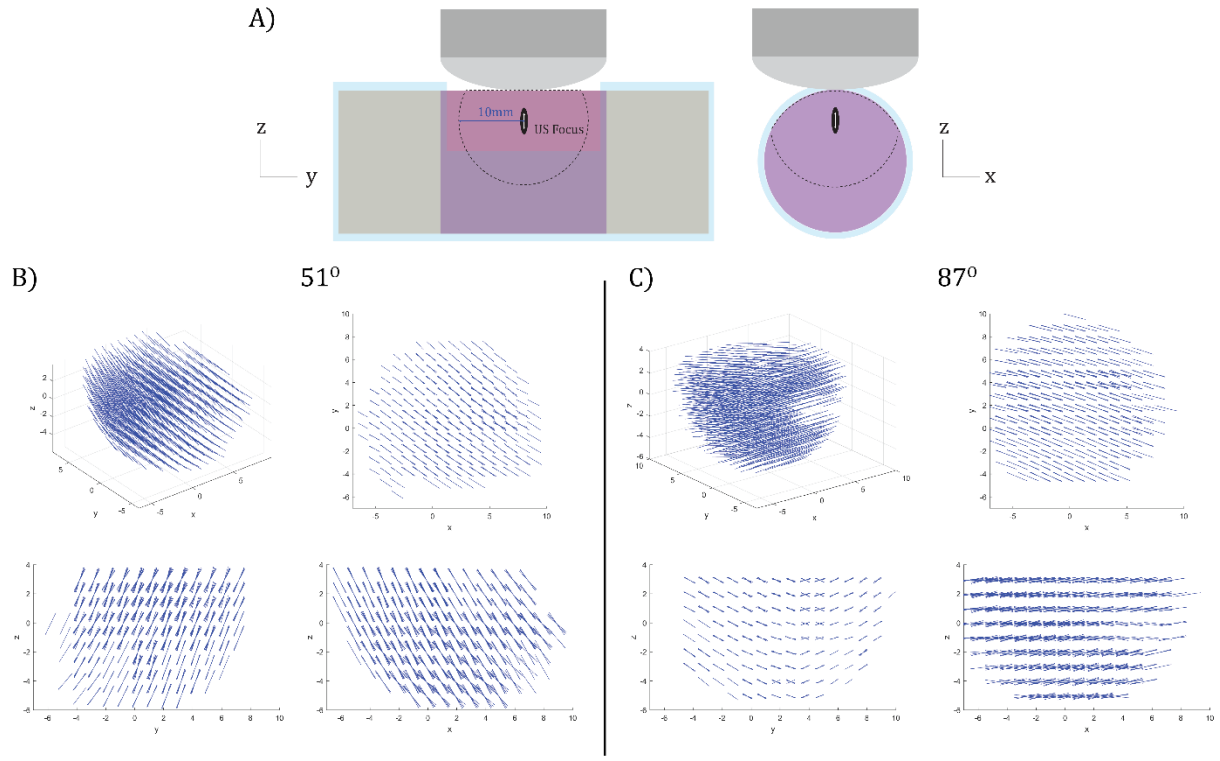

Figure 5.6: DTI results from one sample at two different angles. (A) Schematic diagram. The region of the sample outlined by dotted lines (top) is the partial sphere of 10 mm radius centered about the focal region that was used in the analysis. The sample was rotated 36° between the two experiments. (B-C) DTI estimates of fiber direction are displayed for multiple views for the two orientations: (B) $\beta = 51°$ and (C) $\beta = 87°$.

Shear wave patterns in chicken breast are consistent with an ITI material model. Non-circular waves are observed for all samples; typically wavefronts are elliptical with the major semi-axis aligned with the fiber direction from DTI. Propagation direction was estimated from the wave fields using an array of directional filters [6, 21]. Slow and fast polarization directions were calculated from propagation direction and fiber direction. Figure 5.7 and Figure 5.8 show the results from the directional filtering analysis for a chicken breast sample where actuation was 51° and 87°, respectively, to the fiber direction at 400 Hz on a slice near the center of actuation. The fiber direction ($\boldsymbol{a}$), propagation direction ($\boldsymbol{n}$), slow polarization direction ($\boldsymbol{m}_s$), and fast polarization direction ($\boldsymbol{m}_f$) are shown for the chicken breast sample. The shear wave displacement

is shown for three directions (U, V, W). All samples were masked by distance from focus and DTI fractional anisotropy (FA>0.01).

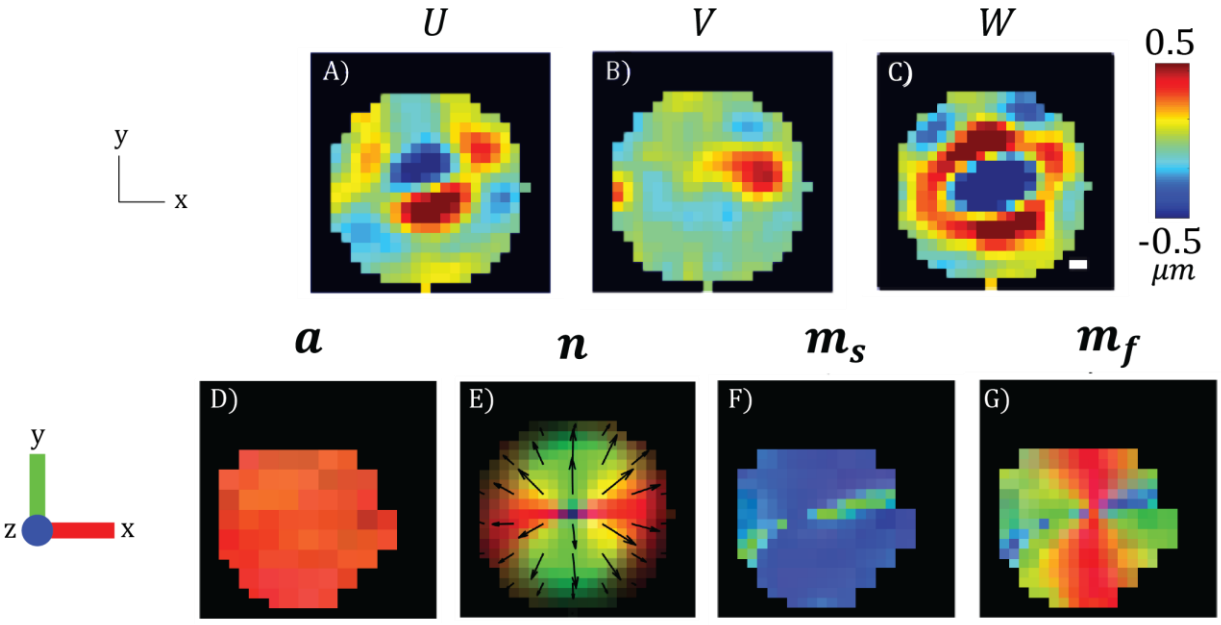

Figure 5.7: MR-HUM chicken breast results for sample with actuation direction 87° to the fiber direction for directional filtering analysis. (A-C) Shear wave displacement in three directions (U, V, W) for a slice near the center of actuation. (D-G) Fiber direction ($\boldsymbol{a}$), propagation direction ($\boldsymbol{n}$), slow polarization direction ($\boldsymbol{m_s}$), and fast polarization direction ($\boldsymbol{m_f}$) are shown for the chicken breast sample. Samples were masked at 10 mm radius from focus. Scale bar in (C) is 2mm.

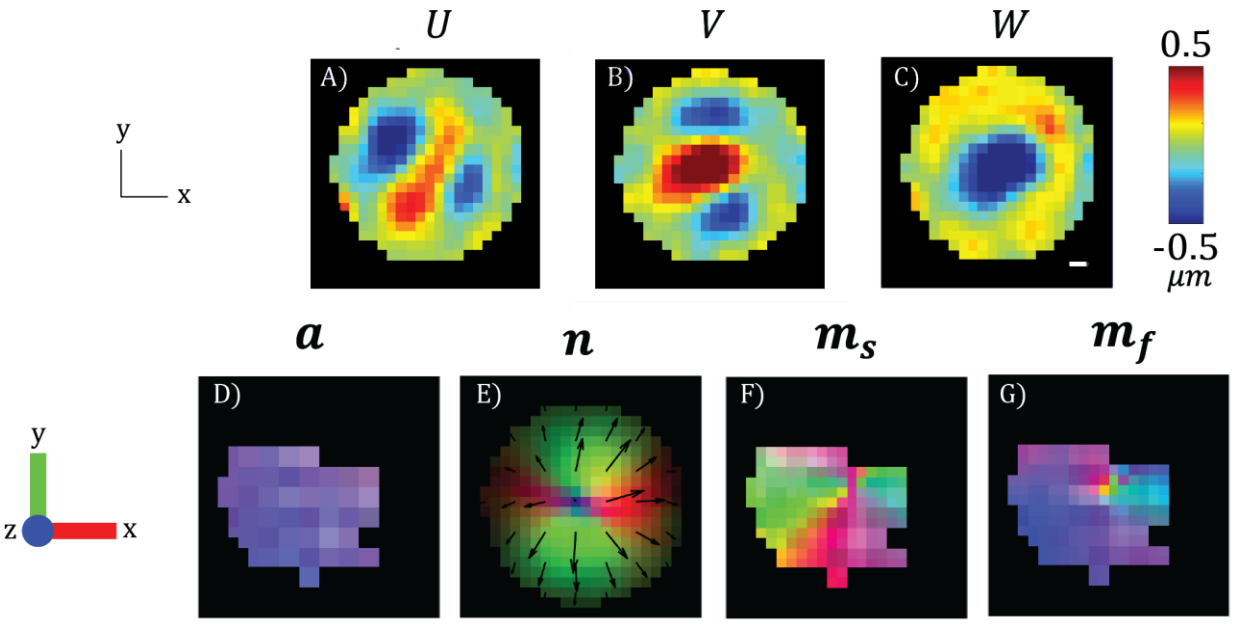

Figure 5.8: MR-HUM chicken breast results for sample with actuation direction 51° to the fiber direction for directional filtering analysis. (A-C) Shear wave displacement in three directions (U, V, W) for a slice near the center of actuation. (D-G) Fiber direction ($\boldsymbol{a}$), propagation direction ($\boldsymbol{n}$), slow polarization direction ($\boldsymbol{m_s}$), and fast polarization direction ($\boldsymbol{m_f}$) are shown for the chicken breast sample. Samples were masked at 10 mm radius from focus. Scale bar in (C) is 2mm.

5.5 Discussion and Conclusions

In this experimental study, MR-HUM was used as a new method for shear wave excitation and imaging of gelatin and *ex vivo* chicken breast. Gelatin samples were used to compare wave fields and shear modulus estimates between MR-HUM and piezo actuation for an isotropic medium. Both wave fields appeared to match the isotropic material model. Waves in MR-HUM propagated from the center of the actuation with approximately spherical wavefronts. While shear waves emanate from the center of actuation in all directions, the SNR decreases significantly with distance. Although wave amplitudes were low, even within 8-10 mm of the US focus, amplitudes within that region had sufficiently high octahedral shear strain (OSS) signal to noise ratio (SNR) material property estimation. For that reason, MR-HUM analysis only included voxels within 6

mm of the ultrasound focus. This local estimation enables property estimation within smaller regions of tissue, like white matter tracts, with less influence from surrounding tissues.

The experimental setup for MR-HUM allowed for simple sample rotation, which enabled multiple experiments to be performed within one sample. One experimental sample could thus be imaged with multiple directions of actuation, allowing the sample to experience both slow and fast shear waves, which is necessary for improved anisotropic parameter estimation [31].

MR-HUM has several advantages over conventional actuation with respect to anisotropic parameter estimation. MR-HUM provides much greater control over the direction of shear wave propagation and polarization compared to boundary excitation (previous chapter). Rather than waves only traveling inwards from the surface of the material, in both simulations and experiment, actuation could easily be varied with respect to fiber direction. MR-HUM is non-destructive, allowing multiple tests to be performed within the same sample. In direct actuation, for example by the titanium rod driven by a piezoelectric actuator, the sample is punctured, which disrupts its integrity before other directions of actuation can be performed.

One of the potential drawbacks of MR-HUM is sample heating. MR-HUM uses focused ultrasound waves, which at high power or prolonged exposure, can produce heating in the focal region. To minimize heating, MR-HUM utilized square waves for amplitude modulation. MRE sequences were optimized to run quickly and ample time was given between scans to ensure low heating of the sample. MRI can be used to estimate temperature changes, but due to the lack of a ground-truth temperature measurement, detailed investigation of sample heating was postponed. All studies were done at power levels that did not cause detectable changes (color, stiffness, warmth)

in the sample. Preliminary investigation of MR-HUM-driven temperature changes is described in Appendix D.

5.6 Summary

This chapter showed that MR-HUM is feasible; FUS can create shear waves with multiple propagation and polarization directions that can be imaged by MRE sequences. Wave fields are limited to the focal region so properties estimated from method are localized. MR-HUM provides enhanced control over wave direction and placement within an anisotropic sample. This method thus addresses some of the challenges of anisotropic material property estimation. The next step, described in the following chapter, is to use date from MR-HUM for anisotropic parameter estimation.

Chapter 6:Estimation of anisotropic material parameters from MR-HUM

6.1 Overview

Leveraging the experimental methods presented in the previous chapter, MR-HUM data will be analyzed by an extension to the anisotropic inversion introduced in chapter 4 to estimate the material properties of *ex vivo* tissue. The inversion approach will be confirmed for MR-HUM using simulations and then applied to the experimental MR-HUM data introduced in the previous chapter.

This study is the first to use MR-HUM data to comprehensively and quantitatively characterize anisotropic material properties of a soft biological tissue *ex vivo*. This is also the first study to simulate MR-HUM to investigate anisotropic wave propagation and to compare these results to experiments.

6.2 Objective and Significance

Soft tissue, specifically fibrous biological tissues, are anisotropic structurally and mechanically. Muscles, tendons, collagen, white matter of the brain, and cardiac tissue are important examples of fibrous tissue. Anisotropy may have an impact in injury mechanisms or reflect tissue health, so understanding the effects of these characteristics is important for the study of these materials. However, measurements of anisotropic mechanical properties are complicated due to experimental and theoretical challenges. The approach presented in this chapter addresses some of the challenges by expanding the capabilities of MRE to characterize anisotropic tissue properties

noninvasively using MR-HUM, which was presented in the previous chapter. The goal of this chapter is to investigate and apply analysis methods for characterization of anisotropic behavior of fibrous materials and soft tissues using MR-HUM.

Previous work has explored theoretical methods to estimate material properties of linear elastic, incompressible, transversely isotropic (ITI) materials using MR elastography [31]. This method has undergone preliminary evaluation using experimental imaging data from slow (pure transverse) and fast (quasi-transverse) shear waves in ITI materials using one actuation direction per MRE scan [30]. To better characterize an ITI material, multiple actuation directions within the same sample are necessary. We propose to improve our ability to characterize anisotropic soft tissues in the linear regime, by using MR-HUM, which is a localized, variable, harmonic shear wave actuation system based on focused ultrasound. Thus, the goal of this chapter is to develop and evaluate anisotropic inversion methods that can exploit the advantages, as well as cope with the challenges of MR-HUM, like sample heating.

6.3 Methods

6.3.1 Simulations

A finite element model (COMSOL Multiphysics; v. 5.3a, Stockholm, Sweden) of a nearly-incompressible transversely isotropic (NITI) cylinder was used to simulate MR-HUM in anisotropic tissue similar to the experimental methods of chicken breast explained in the previous chapter. The data from the ideal situations were used to validate and assess two methods for anisotropic parameter estimation.

Harmonic forcing at a single location was provided, with the force oriented at five different angles of actuation with respect to fiber direction (Figure 6.1A-C). The data from these ideal situations were used to validate two forms of anisotropic parameter estimation, directional filtering with local direct inversion (DF- LDI) and phase gradient (PG).

The simulation domain was a linear, elastic, nearly incompressible, homogenous cylinder of 27 mm diameter and 50 mm length (Figure 6.1A-B; dimensions chosen to match experimental samples). A harmonic body load at a single frequency was applied in the *z*-direction to a small spherical region of 1 mm radius, at the center of the cylinder. The solution for the steady state frequency response was found using COMSOL's frequency domain solver. The domain consisted of 100,505 quadratic Lagrange elements, corresponding to 432,883 degrees of freedom. The boundaries of the cylinder were rigid. Displacement data from the simulation were exported into MATLAB and interpolated onto a 3D grid with 1 mm^3 voxel resolution for analysis using the LiveLink feature of COMSOL ("*mphinterp*" command). For each simulation, the cylinder material had one fiber direction with an angle of $\beta = 0°,\ 30°, 45°, 60°, \text{or } 90°$ relative to the actuation direction, creating a total of 5 models (Figure 6.1C). The harmonic body load produced shear waves propagating with approximately spherical wave fronts outward from the center of the cylinder.

Analysis of the simulations were performed on data from the spherical region within 10 mm radius of the center of the cylinder (location of the harmonic body load) to eliminate effects of wave dissipation and reflections from boundaries. All voxels outside of this region were masked out (eliminated from the analysis; Figure 6.1D-G, shown in black). Fiber direction ($\boldsymbol{a}$; Figure 6.1D for 90° case), shear wave displacement ($\boldsymbol{U}$), and propagation direction ($\boldsymbol{n}$; Figure 6.1E for 90° case)

were found from the simulation inputs and outputs. Shear wave polarization directions ($\boldsymbol{m}_s$ and $\boldsymbol{m}_f$) were calculated using equations 2.37 and 2.38 (Figure 6.1F-G for 90° case).

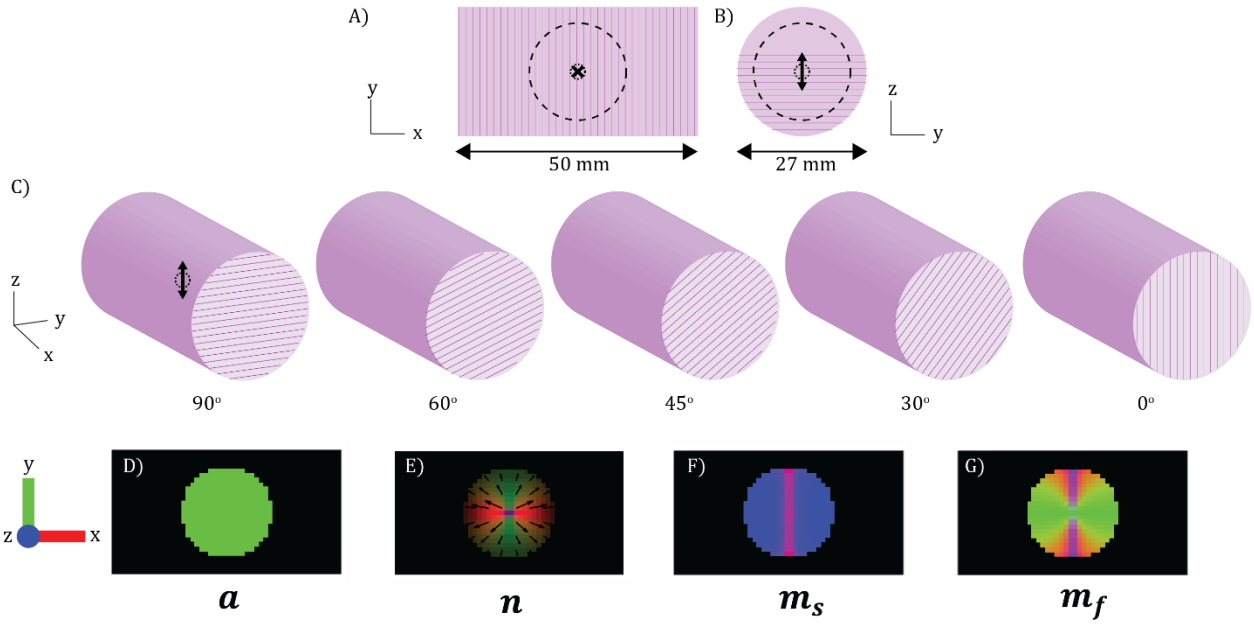

Figure 6.1: Simulation of MR-HUM. (A-B) A body load is applied to the small spherical region in the center of the cylinder of 50 mm length (A, *x*-z view) and 27 mm diameter (B, *y*-z view). The $\beta = 90°$ case is shown. (C) Five models for simulation of MR-HUM, showing the fiber direction at 90°, 60°, 45°, 30°, and 0° to the actuation direction (*z*-direction). (D-G) Parameters of the $\beta = 90°$ case of the simulation shown by colormap where red is in the direction of the *x*-axis, green is in the direction of the *y*-axis, and blue is in the direction of the *z*-axis. All voxels greater than 10 mm from the center (actuation) are removed from analysis using a mask. (D) Fiber direction ($\boldsymbol{a}$) is strictly along the *y*-axis. (E) The shear wave propagation direction ($\boldsymbol{n}$) is outwards from the center. Black arrows emphasize the direction of the wave. (F) Slow shear wave polarization direction ($\boldsymbol{m_s}$) is mainly along the *z*-axis and (G) fast shear wave polarization direction ($\boldsymbol{m_f}$) is mainly along the *y*-axis.

Two sets of material properties were used for the simulations. One simulation set incorporated approximately brain-like shear modulus, with parameters of $\mu = 2000$ Pa, $\phi = 1$, and $\zeta = 2$. Actuation was created by applying a body force of 50 kN/m^3 at 300 Hz. A second simulation set incorporated stiffer, approximately muscle-like, shear modulus, with parameters of $\mu = 7500$ Pa, $\phi = 1$, and $\zeta = 1$. The actuation was created by applying a body force of 150 kN/m^3 at 400 Hz. This simulation set was chosen to approximate the MR-HUM chicken breast experiment explained in the previous chapter. The actuation body forces were chosen to produce micron-level displacement in the simulation.

Data from these simulations, which are noise-free and thus represent an idealized "best-case" scenario, were used to evaluate two approaches for anisotropic property estimation.

6.3.2 Experimental MR-HUM

Eleven (11) cylindrical samples of chicken breast of 25 mm (1.0 inch) diameter and varying height > 25 mm were imbedded in gelatin-glycerol mixture (described in 5.3.2). The samples were tested in a modified 50 mL tube with a 25 × 25 mm window. The ultrasound transducer was placed above the surface of the chicken breast sample with a water-filled bladder as an air-free connection. The focus of the ultrasound transducer was electronically moved to 2 mm below the natural focus. Samples were actuated at 400 Hz with ~1.5 W ultrasound power. Each sample underwent two MR-HUM scans (described in Chapter 5.3.3.1). The sample was rotated approximately 45° between the two scans, with the transducer remaining stationary.

6.3.3 Approach to Anisotropic Property Estimation

6.3.3.1 Overview of Estimation Using Multiple Linear Regression

Two approaches were used to estimate the material properties of the chicken breast samples: (i) directional filtering with local direct inversion (DF-LDI) and (ii) phase gradient (PG). These approaches were used to separate the waves by polarization direction ("slow" and "fast") and to approximate the apparent shear modulus (ρc^2) for each type. After those steps, the two analysis methods were essentially the same. The three unknown parameters of an NITI material were estimated from the equations for slow and fast shear waves (explained in Chapter 4.3.3) using a multiple linear regression model of the form:

$$y = \beta_0 + \beta_1 x_1 + \beta_2 x_2. \tag{6.1}$$

The unknown parameters are $\beta_0 = \mu$, $\beta_1 = \mu\phi$ and $\beta_2 = \mu\zeta$. The dependent variable is the apparent shear modulus: $y = \mu_{app}$ ($\mu_{app} = \mu_s$ for slow waves and $\mu_{app} = \mu_f$ for fast shear waves). The independent variables in the multiple regression are defined in terms of the angle θ as follows:

$$x_1 = \begin{cases} \cos^2\theta & (\text{"slow" voxels}) \\ \cos^2 2\theta & (\text{"fast" voxels}) \end{cases} \text{ and } x_2 = \begin{cases} 0 & (\text{"slow" voxels}) \\ \sin^2 2\theta & (\text{"fast" voxels}) \end{cases}. \tag{6.2}$$

6.3.3.2 Classification of Voxels as "Slow" or "Fast"

For a voxel to be included in the analysis, multiple conditions must be met to ensure that approximations and assumptions are reasonably accurate. (i) The voxel must experience a minimum wave amplitude; (ii) the voxel must be within a certain radius of the center of actuation; (iii) the propagation direction within the voxel must be close to that of radially propagating waves, and (iv) the voxel must have a fractional anisotropy above a threshold. Table 6.1 summarizes the inclusion criteria for the analysis.

Table 6.1: Inclusion criteria for analysis of anisotropic parameter estimation for both simulations and experiments. Parameters were chosen to be consistent with experimental studies, which had lower wave amplitude and generally low FA.

Inclusion Criteria	Equation	Parameter
Amplitude	$\|U\| > A\,\|U\|_{median}$	$A = 0.1$
Propagation direction	$\boldsymbol{n} \cdot \boldsymbol{e_r} > prop_{thresh}$	$prop_{thresh} = 0.75$
Radial distance	$r < R_{max}$	$R_{max} = 10\,mm$
Fraction Anisotropy	$FA > FA_{thresh}$	$FA_{thresh} = 0.01$

After voxels are selected based on these inclusion criteria, they must also meet classification criteria to be sorted as either a "slow" or "fast" voxel. The voxel must have a dominant shear wave polarization (be dominated by either a slow or fast shear wave – not both). A voxel was classified as a fast or slow shear wave voxel if the normalized displacement or curl component in the fast or slow polarization direction exceeded a minimum "polarization threshold" (pol_{thresh}) and the other component was below a corresponding maximum value ($1 - pol_{thresh}$). The normalized fast and slow shear wave displacement components are:

$$\widehat{U}_f = \frac{\boldsymbol{U} \cdot \boldsymbol{m_f}}{|\boldsymbol{U}|}, \tag{6.3}$$

$$\widehat{U}_s = \frac{\boldsymbol{U} \cdot \boldsymbol{m_s}}{|\boldsymbol{U}|}. \tag{6.4}$$

Thus a voxel would be designated as "fast" if $\widehat{U}_f > pol_{thresh}$ and $\widehat{U}_s < 1 - pol_{thresh}$, and a voxel is classified as "slow" if $\widehat{U}_s > pol_{thresh}$ and $\widehat{U}_f < 1 - pol_{thresh}$. Analogous criteria could be applied to the curl field, $\boldsymbol{\Gamma}$; interestingly it can be shown that the curl polarizations are orthogonal to the displacement polarization directions, so that the normalized curl components are:

$$\hat{\Gamma}_f = \frac{\boldsymbol{\Gamma} \cdot \boldsymbol{m_s}}{|\boldsymbol{\Gamma}|}, \tag{6.5}$$

$$\hat{\Gamma}_s = \frac{\boldsymbol{\Gamma} \cdot \boldsymbol{m_f}}{|\boldsymbol{\Gamma}|}. \tag{6.6}$$

Voxels that did not meet either of these criteria were excluded from the analysis. In this study, DF-LDI used displacement for classification and PG used curl. Table 6.2 and

Table **6.3** outline the classification criteria used for DF-LDI and PG methods.

Table 6.2: Classification criteria for DF-LDI analysis

Classification Criteria for DF-LDI	**Equation**	**Parameter**
Polarization direction - slow	$\left\|\widehat{U}_s\right\| > pol_{thresh}$ $\left\|\widehat{U}_f\right\| < 1 - pol_{thresh}$	$pol_{thresh} = 0.75$
Polarization direction - fast	$\left\|\widehat{U}_f\right\| > pol_{thresh}$ $\left\|\widehat{U}_s\right\| < 1 - pol_{thresh}$	$pol_{thresh} = 0.75$

Table 6.3: Classification criteria for PG analysis

Classification Criteria for PG	**Equation**	**Parameter**
Polarization direction - slow	$\left\|\hat{\Gamma}_s\right\| > pol_{thresh}\,\|\Gamma\|_{median}$	$pol_{thresh} = 0.75$
Polarization direction - fast	$\left\|\hat{\Gamma}_f\right\| > pol_{thresh}\,\|\Gamma\|_{median}$	$pol_{thresh} = 0.75$

A sensitivity analysis of the effects of selection criteria on parameter estimates is shown in Appendix E.

6.3.3.3 Directional Filtering with LDI (DF-LDI) (c.f. Chapter 4.3.3.3)

The apparent shear modulus ($\mu_{app} = \rho c^2$) was calculated for each voxel using local direct inversion (LDI). Shear modulus was estimated from the shear wave displacements using the viscoelastic analog of the Navier equation, which assumes the material is linear, isotropic, and locally homogenous [1] (see Chapter 2.3.2.2). After LDI analysis, shear wave data were characterized by shear wave polarization, with voxels classified as either slow or fast based on the slow and fast shear wave criteria (Table 4.2). Directional filtering (using 192 filter directions) was used to identify average propagation direction, $\boldsymbol{n}$. Fiber direction, $\boldsymbol{a}$, was obtained from DTI and the angle θ between $\boldsymbol{n}$ and $\boldsymbol{a}$ was found. Polarization directions $\boldsymbol{m_s} = (\boldsymbol{n} \times \boldsymbol{a})/|\boldsymbol{n} \times \boldsymbol{a}|$ and $\boldsymbol{m_f} = \boldsymbol{n} \times \boldsymbol{m_s}$ were calculated, and the normalized slow and fast displacement ($\widehat{U}_s$ and $\widehat{U}_f$) components were used to classify voxels as either "slow" or "fast." These values were then used in the multiple linear regression (Eq. 6.1) to estimate μ, $\mu\phi$ and $\mu\zeta$. A flow chart for this method is shown in Figure 4.7.

6.3.3.4 Phase Gradient (PG)

The wave propagation direction ($\boldsymbol{n}$) of the data was assumed to be purely radial, emanating from center of actuation. Slow and fast polarization directions ($\boldsymbol{m_s}$ and $\boldsymbol{m_f}$ respectively) and propagation-fiber angle, θ, were calculated using the assumed propagation direction and the fiber direction ($\boldsymbol{a}$) of the sample/simulation.

$$\boldsymbol{m_s} = \frac{\boldsymbol{n}\times\boldsymbol{a}}{|\boldsymbol{n}\times\boldsymbol{a}|} \quad (6.7, \text{c.f. } 2.37)$$

$$\boldsymbol{m_f} = \boldsymbol{n} \times \boldsymbol{m_s} \quad (6.8, \text{c.f. } 2.37)$$

The curl of the displacement was then sorted into slow and fast components.

$$\Gamma_s = \boldsymbol{\Gamma} \cdot \boldsymbol{m_f} \quad (6.9)$$

$$\Gamma_f = \boldsymbol{\Gamma} \cdot \boldsymbol{m_s} \quad (6.10)$$

Next, the phase angles of the slow and fast (ψ_s and ψ_f) waves were calculated.

$$\psi_s = \angle\Gamma_s \quad (6.11)$$

$$\psi_s = \angle\Gamma_f \quad (6.12)$$

The wave numbers ($\boldsymbol{k_s}$ and $\boldsymbol{k_f}$) were estimated from the gradients of phase.

$$\boldsymbol{k_s} = \boldsymbol{\nabla}\psi_s \quad (6.13)$$

$$\boldsymbol{k_f} = \boldsymbol{\nabla}\psi_f \quad (6.14)$$

Wavelength for slow and fast waves (λ_s and λ_f) were calculated from the radial component of the wave number vectors.

$$\lambda_s = \frac{2\pi}{\boldsymbol{k_s}\cdot\boldsymbol{n}} \quad (6.15)$$

$$\lambda_f = \frac{2\pi}{\boldsymbol{k_f}\cdot\boldsymbol{n}} \quad (6.16)$$

Apparent shear modulus was calculated from wavelength, using the density value of $\rho = 1000\,\frac{kg}{m^3}$ and the frequency of the actuation (f).

$$\mu_{app} = \mu_s = \rho(\lambda_s f)^2, \tag{6.17}$$

$$\mu_{app} = \mu_f = \rho(\lambda_f f)^2. \tag{6.18}$$

Voxels classified as either slow or fast were masked based on the slow and fast shear wave criteria (Table 6.3). These values and the corresponding values of the independent variables for "slow" and "fast" voxels were used in the linear regression equation (Eq. 6.1) to estimate values of μ, $\mu\phi$ and $\mu\zeta$. Figure 6.2 outlines the steps of PG.

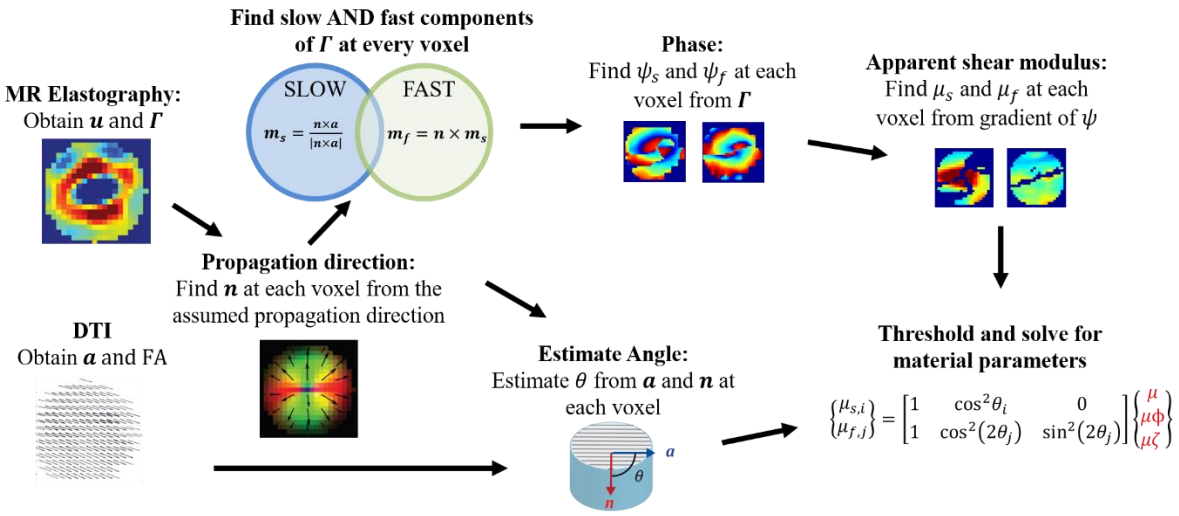

Figure 6.2: Flow chart outlining the steps of shear wave separation and anisotropic parameter estimation using PG.

6.4 Results

6.4.1 Simulation – DF-LDI

The simulation output consisted of the shear wave displacements, mirroring the output of the MRE sequence in an MR-HUM experiment. Fiber direction was treated as a known parameter. Figure 6.3 shows the shear wave displacements and slow and fast shear wave components for one simulation case where actuation was 90° to the fiber direction. For this specific case, the majority of the waves were classified as slow shear waves. Changing the direction of actuation, relative to the fiber direction, produced various different combinations of slow and/or fast shear waves.

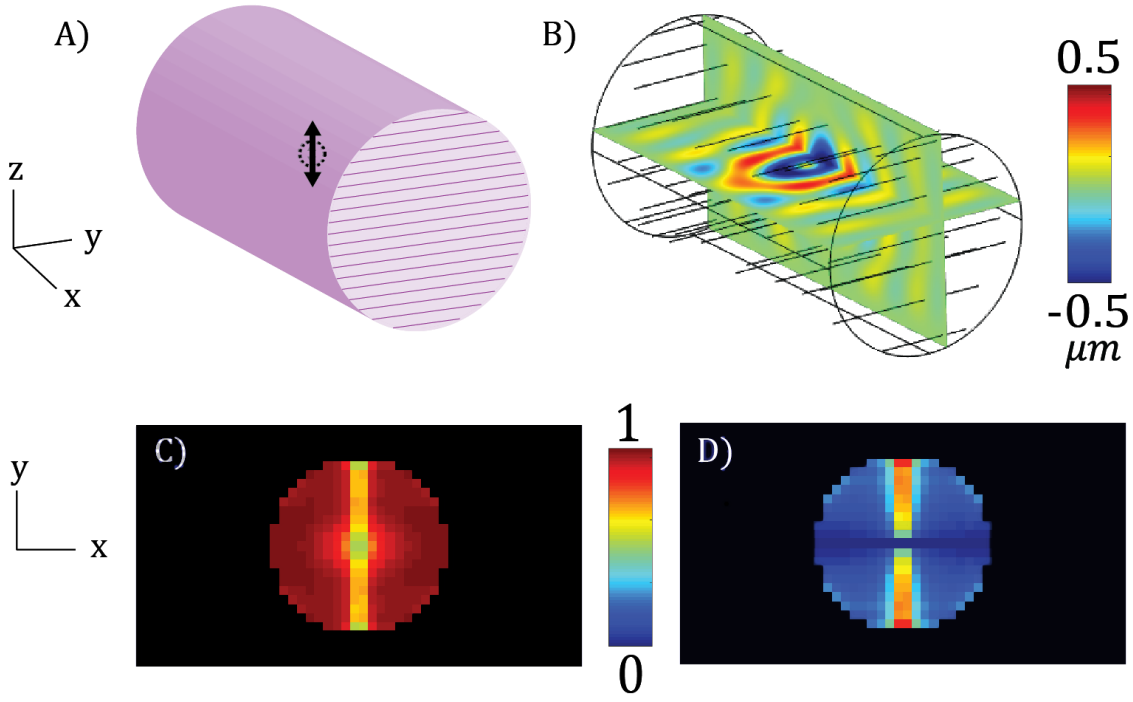

Figure 6.3: Simulation and DF-LDI analysis of NITI cylinder with actuation 90° to fiber direction for the muscle-like simulation case at 400 Hz actuation frequency. (A) Cylinder with fibers along the *y*-axis. The small sphere outlines the actuation source, which was centered in the cylinder and experienced oscillatory force in the *z*-direction. (B) Shear wave displacements (*w*-component) on two perpendicular planes through the center of the cylinder. The black lines represent the fiber direction. (C) The normalized component of displacement in the slow polarization direction, $\hat{U}_s$, masked by displacement amplitude. The slice shown is the center slice normal to *z*-axis. Voxels farther than 10 mm from the center were masked out. Most of the displacement for this simulation case is due to slow shear waves. (D) The normalized component of displacement in the fast polarization direction, $\hat{U}_f$, masked by displacement amplitude. Fast shear waves do not contribute much to the displacement field. Even voxels that apparently exhibit fast shear waves also have a large slow shear wave component (see panel C), so they will not be classified as "fast" voxels for the regression analysis.

The angle between the propagation direction and the fiber direction, θ, was calculated for the sample. Apparent shear modulus, μ_{app}, was calculated for the entire volume using LDI. All voxels were categorized as slow or fast (or neither) based on the criteria stated in Chapter 6.3.3 (Table **6.1** and Table 4.2). Figure 6.4 shows the θ and $\mu_{app}$and the corresponding slow and fast components for the simulation case where the actuation direction is perpendicular to the fiber direction. For

this specific case, all voxels used in the analysis were classified as slow shear wave voxels. Some voxels were excluded because they had components of both slow and fast shear waves.

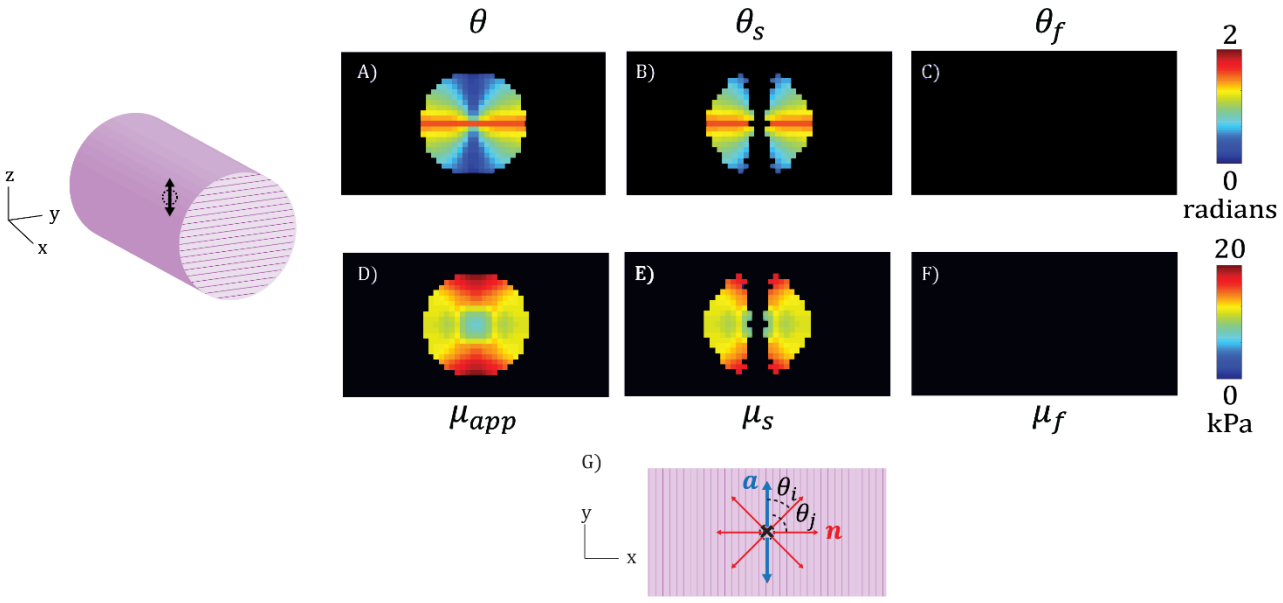

Figure 6.4: Angle and apparent shear modulus on central slice for the simulation case with actuation 90° to fibers for the muscle-like sample excited at 400 Hz. (A) The angle between the propagation direction and fiber direction (θ) for all voxels within 10 mm of center. (B) Estimates of θ in voxels that were classified as slow based on the criteria (θ_s). All voxels that were not classified as slow are masked out (shown as black). (C) Estimates of θ in voxels that were classified as fast (θ_f). No voxels for this case of the simulation were classified as fast. (D) The apparent shear modulus (μ_{app}) estimated using isotropic viscoelastic LDI. (E) Estimates of μ_{app} in voxels that were classified as slow (μ_s). All voxels not classified as slow were masked out (shown as black). The images are further masked so that only voxels within 10 mm are included. (F) Estimates of μ_{app} in voxels that were classified as fast based on the inclusion criteria (μ_f). No voxels for this case of the simulation were classified as fast. (G) Schematic diagram of θ with $\boldsymbol{n}$ and $\boldsymbol{a}$.

After classification, all voxels from the simulation that were classified as either slow or fast were used to estimate the three material parameters ($\mu, \mu\phi, \mu\zeta$) using the linear regression model (Eq. 6.1). Statistics were performed using MATLAB's built-in linear regression model ("*fitlm*"). Figure 6.5 shows all the apparent shear modulus voxels classified as slow or fast versus the sine or cosine of angle for all cases of the simulation for the brain-like stiffness at 300 Hz (A-slow voxels and B-fast voxels) and the muscle-like stiffness at 400 Hz (C-slow voxels and D-fast voxels).

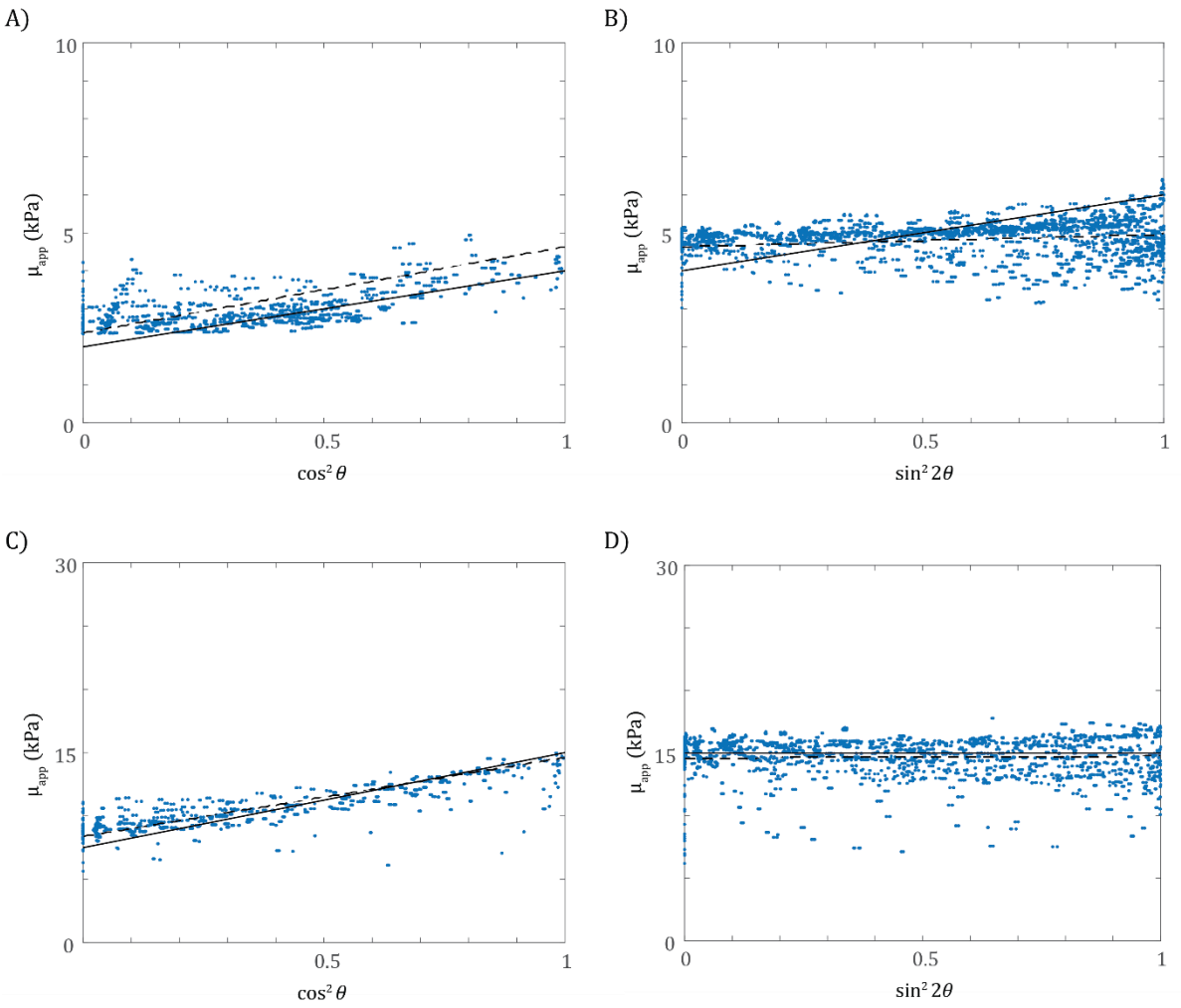

Figure 6.5: Results from all NITI cylinder simulations for all cases for DF-LDI method. Each dot represents one voxel that met slow (A and C) or fast (B and D) criteria for DF-LDI analysis. The black solid line represents the linear relationship expected for the input parameters for brain-like tissue (A -B): $\mu = 2$ kPa, $\phi = 1, \zeta = 2$ and muscle like tissue (C-D): $\mu = 7.5$ kPa, $\phi = 1, \zeta = 1$. The black dashed line represents the linear regression model for the estimated material parameters found using DF-LDI. (A) Apparent shear modulus in slow voxels for all simulation cases of the NITI cylinder for brain-like tissue. (B) Apparent shear modulus in fast voxels for all simulation cases of the NITI cylinder for brain-like tissue. (C) Apparent shear modulus in slow voxels for all simulation cases of the NITI cylinder for muscle-like tissue. (D) Apparent shear modulus in fast voxels for all simulation cases of the NITI cylinder for muscle-like tissue.

Table 6.4 shows the results of the DF-LDI anisotropic parameter estimation for both simulation cases: brain-like stiffness and muscle-like stiffness. For both cases shear modulus was over-estimated and the shear and tensile anisotropy were under-estimated.

Table 6.4: Comparison between exact values of the simulation parameters and the values estimated by DF-LDI for brain-like tissue and muscle-like tissue, using multiple linear regression. For the brain-like stiffness simulation, 7,734 voxels were used in the linear model fit (R^2=0.75). The p-value was less than machine precision. For the muscle-like stiffness simulation, 7,304 voxels were used in the linear model fit (R^2=0.69). The p-value was less than machine precision. $\mu, \mu\phi,$ and $\mu\zeta$ are in units of kPa; ϕ and ζ are unitless.

		Input	**Estimated**	**Error (%)**
Brain-like stiffness	μ [kPa]	2.00	2.37	18.4
	$\mu\phi$ [kPa]	2.00	2.27	13.3
	$\mu\zeta$ [kPa]	4.00	2.59	35.2
	ϕ	1.00	0.96	4.31
	ζ	2.00	1.09	45.3
		Input	**Estimated**	**Error**
Muscle-like stiffness	μ [kPa]	7.50	8.39	11.8
	$\mu\phi$ [kPa]	7.50	6.22	17.1
	$\mu\zeta$ [kPa]	7.50	6.37	15.1
	ϕ	1.00	0.74	25.8
	ζ	1.00	0.76	24.0

6.4.2 Simulation – Phase Gradient Inversion

Voxels were first separated into slow and fast categories based on the polarization direction (Table 6.3). Figure 6.6 shows the results of initial voxel classification for displacement ($\boldsymbol{U}$: panels A-B) and curl ($\boldsymbol{\Gamma}$: panels C-D) with amplitude thresholding for the $\beta = 90°$ case at 400 Hz. The phase angle ($\boldsymbol{\psi}$) of each shear wave component was calculated using the curl. Figure 6.6E-F show the phase for the $\beta = 90°$ case at 400 Hz, with arrows representing the propagation direction for the voxels that meet all the criteria for slow or fast waves (note: there are no arrows on voxels

categorized as fast because those voxels did not meet criteria for inclusion). After all masking and classification was performed, the angle between propagation direction and fiber direction (θ) and apparent shear modulus (μ_{app}) are shown for slow and fast voxels. Figure 6.6 G-J shows the classification in one slice for the $\beta = 90°$ case at 400 Hz. As shown in the previous section, the majority of the voxels for the $\beta = 90°$ case were classified as slow.

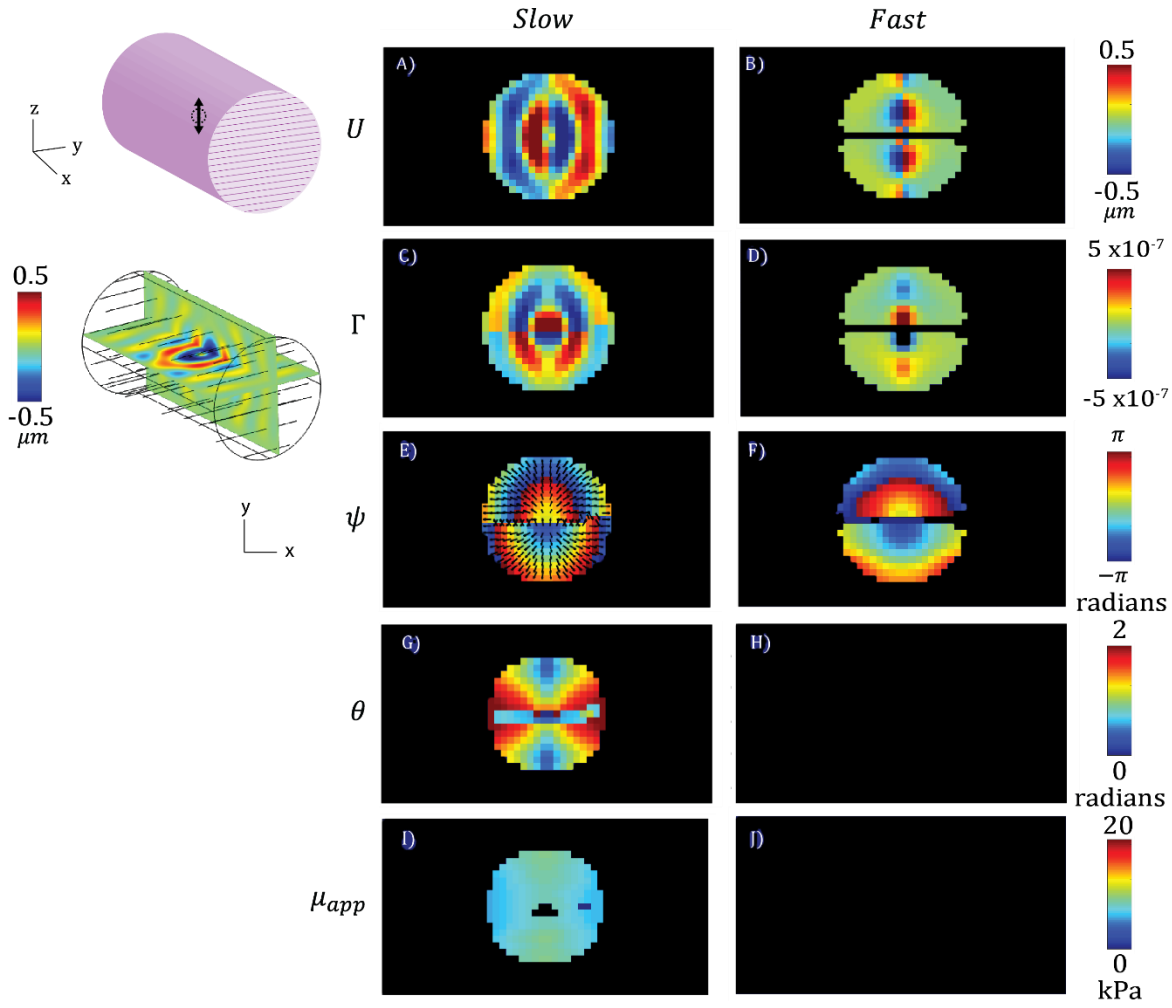

Figure 6.6: Simulation and phase gradient (PG) analysis of NITI cylinder with actuation 90° to fiber direction at 400 Hz. Voxels were masked based on inclusion criteria from Table 6.1. Images are from the center slice normal to the *z*-axis. (A) Displacement field component (U_s) contributed by shear waves with slow polarization. (B) Displacement field component (U_f) due to shear waves with fast polarization. (C) Curl field component (Γ_s) due to shear waves with slow polarization. (D) Curl field component (Γ_f) due to shear waves with fast polarization. (E) Phase angle (ψ) of slow shear wave curl field, U_s. Black arrows represent the propagation direction. Arrows only appear over voxels that meet the classification criteria for inclusion in the analysis (Table 6.3). (F) Phase angle (ψ) of fast shear wave curl field, U_f. There are no black arrows that represent the propagation direction because no fast voxels for this case meet the criteria for inclusion in the analysis (Table 6.3). (G) Angle between propagation direction and fiber direction (θ) for slow voxels. Voxels that did not meet classification criteria were masked out (Table 6.3). (H) Angle between propagation direction and fiber direction (θ) for fast voxels. No fast voxels met the classification criteria (Table 6.3). I) Apparent shear modulus (μ_{app}) in slow voxels. Voxels that did not meet classification criteria were masked out (Table 6.3). (J) Apparent shear modulus (μ_{app}) categorized by fast polarization. No fast voxels met the classification criteria (Table 6.3).

As in the previous section, after classification into slow or fast voxels using PG method, all remaining voxels were used to estimate the anisotropic material parameters ($\mu, \mu\phi, \mu\zeta$) using the

multiple linear regression model (Eq. 6.1). The multiple linear regression analysis was performed using the linear regression function ("*fitlm*") in MATLAB Statistics and Machine Learning Toolbox. Figure 6.7 shows all the apparent shear modulus voxels classified as slow or fast versus the angle for all cases of the simulation for the brain-like stiffness at 300 Hz (A-slow voxels and B-fast voxels) and the muscle-like stiffness at 400 Hz (C-slow voxels and D-fast voxels).

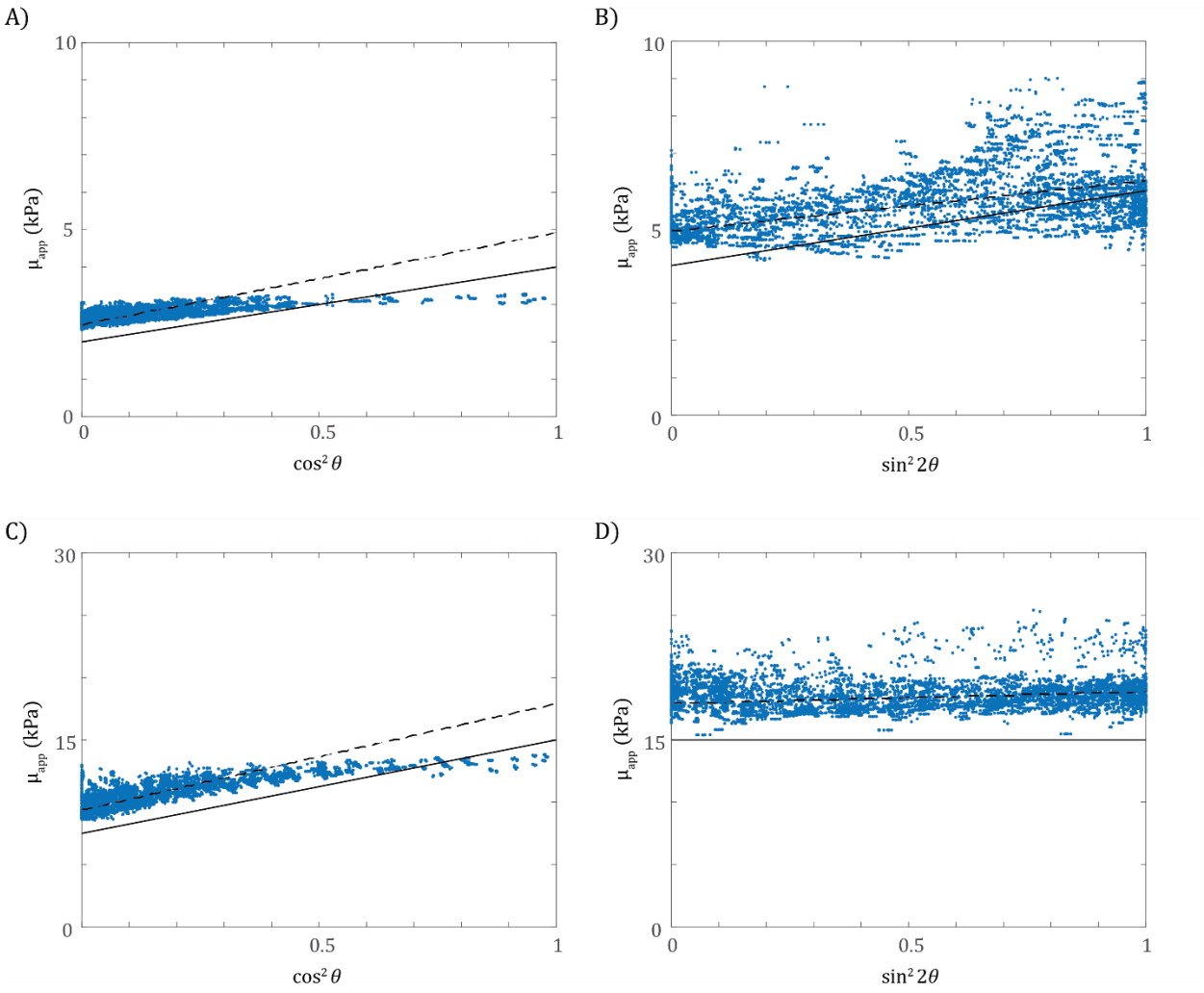

Figure 6.7: Apparent shear modulus from all NITI cylinder simulations for all cases, estimated by the PG method. Each dot represents one voxel that met slow (A and C) or fast (B and D) criteria for PG analysis. The black solid line represents the linear relationship expected for the input parameters for brain-like tissue (A -B): $\mu = 2$ kPa, $\phi = 1, \zeta = 2$ and muscle like tissue (C-D): $\mu = 7.5$ kPa, $\phi = 1, \zeta = 1$. The black dashed line represents the linear regression model for the estimated material parameters found using PG. (A) Apparent shear modulus in slow voxels for all simulation cases of the NITI cylinder for brain-like tissue. B) Apparent shear modulus in fast voxels for all simulation cases of the NITI cylinder for brain-like tissue. (C) Apparent shear modulus in slow voxels for all simulation cases of the NITI cylinder for muscle-like tissue. (D) Apparent shear modulus in fast voxels for all simulation cases of the NITI cylinder for muscle-like tissue.

Table 6.5 shows the results of the PG anisotropic parameter estimation for both simulation cases: brain-like stiffness and muscle-like stiffness. The inputs, estimated values, and error are shown.

Table 6.5: Comparison between the simulation parameter input and the values estimated by phase gradient (PG) for brain-like tissue and muscle-like tissue stiffness values. The input column shows the material parameters used for the simulation. The estimated values are the results of PG estimation, fitted using a linear model regression. For the brain-like stiffness simulation, 11,825 voxels were used in the linear model fit (R^2=0.859). The p-value was less than machine precision. For the muscle-like stiffness simulation, 12,501 voxels were used in the linear model fit (R^2=0.908). The p-value was less than machine precision. $\mu, \mu\phi,$ and $\mu\zeta$ are in units of kPa; ϕ and ζ are unitless.

		Input	**Estimated**	**Error (%)**
Brain-like stiffness	μ [kPa]	2	2.46	23.0
	$\mu\phi$ [kPa]	2	2.46	23.0
	$\mu\zeta$ [kPa]	4	3.81	4.7
	ϕ	1	1.00	0.0
	ζ	2	1.55	22.5
		Input	**Estimated**	**Error**
Muscle-like stiffness	μ [kPa]	7.5	9.38	25.1
	$\mu\phi$ [kPa]	7.5	8.53	13.7
	$\mu\zeta$ [kPa]	7.5	9.48	26.4
	ϕ	1	0.91	9.1
	ζ	1	1.01	1.0

6.4.3 Experiment – DF-LDI

Shear wave displacement fields were calculated from the phase images from the MR-HUM scan (Chapter 2.3.1). Eigenvalues and eigenvectors of the diffusion tensor, which correspond principal diffusivity values and directions, were obtained from the DTI scan and used to estimate fractional anisotropy (FA) (Eq. 2.58) and fiber direction (a). Section 5.4.2 shows the results from the MR-

HUM and DTI scan for one chicken sample actuated at two different angles to the fiber. Voxels were excluded from the estimation if they did not meet the inclusion criteria (Table 6.1). Voxels were classified as slow or fast, using the criteria defined in Table 6.2. Figure 6.8 A-B and Figure 6.9 A-B show the contributions of slow versus fast shear waves for a chicken breast sample where the actuation direction was 51° and 87° from the fiber direction, respectively. Figure 6.8 C and Figure 6.9 C show θ. This can be masked based on the criteria for slow and fast shear waves to categorize θ as slow or fast (Figure 6.8 D-E and Figure 6.9 D-E). LDI was used to calculate the shear modulus, μ_{app}, shown in Figure 6.8 F and Figure 6.9 F. This was also masked based on the criteria for slow and fast shear waves to categorize μ_{app} as slow or fast (Figure 6.8 G-H and Figure 6.9 G-H). Only voxels that are sufficiently slow or sufficiently fast are included in the analysis (Table 6.2). Only a few voxels in the $\beta = 51°$ degrees case are either slow or fast. The $\beta = 87°$ case is almost exclusively categorized as slow shear waves. The voxels that remain in the analysis match the positions on the polarization maps (Figure 6.8 A-B and Figure 6.9 A-B) where regions of high polarization (red) exist.

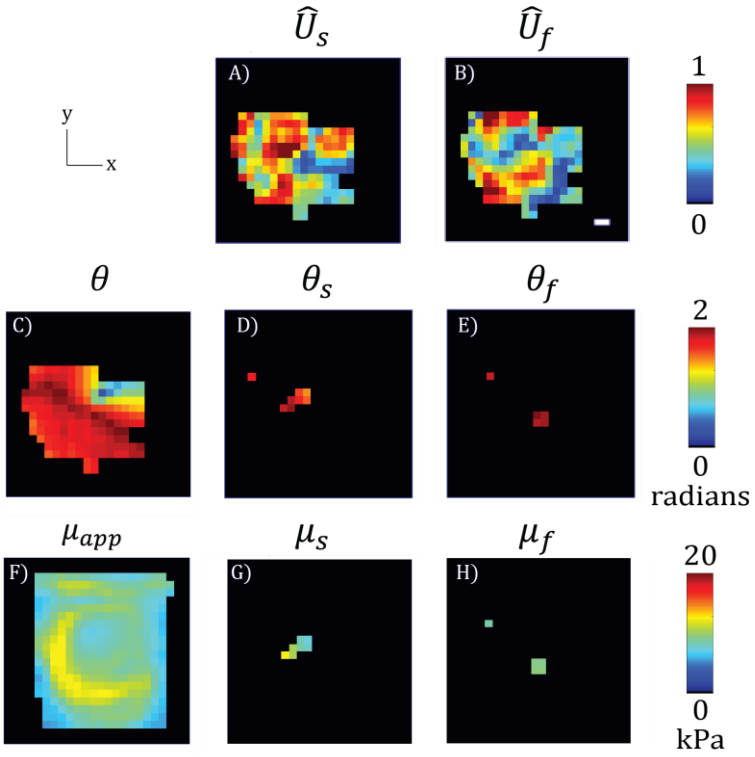

Figure 6.8: Experimental results from MR-HUM in muscle tissue (chicken breast) sample with actuation direction 51° to the fiber direction, analyzed using DF-LDI. These images correspond to chicken breast sample shear wave displacements and wave results in Figure 5.8. The slice is near the center of actuation, with voxels that do not meet the inclusion criteria (Table 6.1) removed during masking (black). (A) The normalized component of displacement in the slow polarization direction, $\widehat{U}_s$. (B) The normalized component of displacement in the fast polarization direction, $\widehat{U}_s$. (C) The angle between the propagation direction and fiber direction (θ). (D) The angle θ in slow voxels, masked by slow shear wave polarization classification (Table 6.2). This slice shows very few slow voxels that meet classification criteria (these voxels correspond to simultaneous "hot spots" in the $\widehat{U}_s$ field in panel A and "cold spots" in the $\widehat{U}_f$ field in panel B). (E) The angle θ in fast voxels, masked by shear wave polarization classification (Table 6.2). This slice shows very few fast voxels that meet classification criteria (these voxels correspond to simultaneous "hot spots" in the $\widehat{U}_f$ field in panel B and "cold spots" in the $\widehat{U}_s$ field in panel A). (F) The apparent shear modulus (μ_{app}) calculated by isotropic viscoelastic LDI. (G) The apparent shear modulus in slow voxels, masked by shear wave polarization classification (Table 6.2). This slice shows slow voxels that meet classification criteria (these voxels correspond to simultaneous "hot spots" in the $\widehat{U}_f$ field in panel B and "cold spots" in the $\widehat{U}_s$ field in panel A). (H) The apparent shear modulus in fast voxels, masked by shear wave polarization classification (Table 6.2). This slice shows very few fast voxels that meet classification criteria (these voxels correspond to simultaneous "hot spots" in the $\widehat{U}_f$ field in panel B and "cold spots" in the $\widehat{U}_s$ field in panel A). Scale bar in (B) is 2mm.

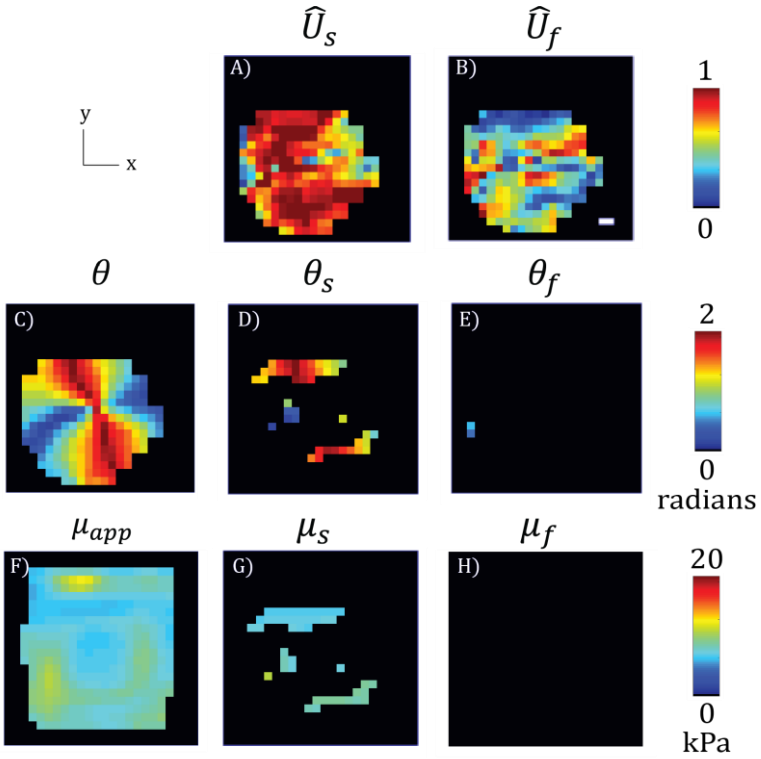

Figure 6.9: Experimental results from MR-HUM in muscle tissue (chicken breast) sample with actuation direction 87° to the fiber direction, analyzed using DF-LDI. These images correspond to chicken breast sample shear wave displacements and wave results in Figure 5.9. The slice is near the center of actuation, with voxels that do not meet the inclusion criteria (Table 6.1) removed during masking (black). (A) The normalized component of displacement in the slow polarization direction, $\widehat{U}_s$. (B) The normalized component of displacement in the fast polarization direction, $\widehat{U}_s$. (C) The angle between the propagation direction and fiber direction (θ). (D) The angle θ in slow voxels, masked by slow shear wave polarization classification (Table 6.2). This slice shows slow voxels that meet classification criteria (these voxels correspond to simultaneous "hot spots" in the $\widehat{U}_s$ field in panel A and "cold spots" in the $\widehat{U}_f$ field in panel B). (E) The angle θ in fast voxels, masked by shear wave polarization classification (Table 6.2). This slice shows very few fast voxels that meet classification criteria (these voxels correspond to simultaneous "hot spots" in the $\widehat{U}_f$ field in panel B and "cold spots" in the $\widehat{U}_s$ field in panel A). (F) The apparent shear modulus (μ_{app}) calculated by isotropic viscoelastic LDI. (G) The apparent shear modulus in slow voxels, masked by shear wave polarization classification (Table 6.2). This slice shows slow voxels that meet classification criteria (these voxels correspond to simultaneous "hot spots" in the $\widehat{U}_f$ field in panel B and "cold spots" in the $\widehat{U}_s$ field in panel A). (H) The apparent shear modulus in fast voxels, masked by shear wave polarization classification (Table 6.2). This slice shows very few fast voxels that meet classification criteria (these voxels correspond to simultaneous "hot spots" in the $\widehat{U}_f$ field in panel B and "cold spots" in the $\widehat{U}_s$ field in panel A). Scale bar in (B) is 2mm.

Similar to the simulations in the previous sections, after classification, all voxels from each sample (two MR-HUM experiments) that were classified as either slow or fast were used to estimate the three material parameters ($\mu, \mu\phi, \mu\zeta$) using the multiple linear regression model from MATLAB. Figure 6.10 shows the apparent shear modulus for voxels classified as slow or fast versus the

relevant functions of angle for one chicken sample (shown in above figures) using DF-LDI. A total of four samples were used in the analysis. Samples were excluded if fewer than 150 voxels from the two combined MR-HUM experiments met inclusion criteria for the anisotropic parameter estimation, or if $p > 0.05$ for any parameter in the multiple linear model regression model.

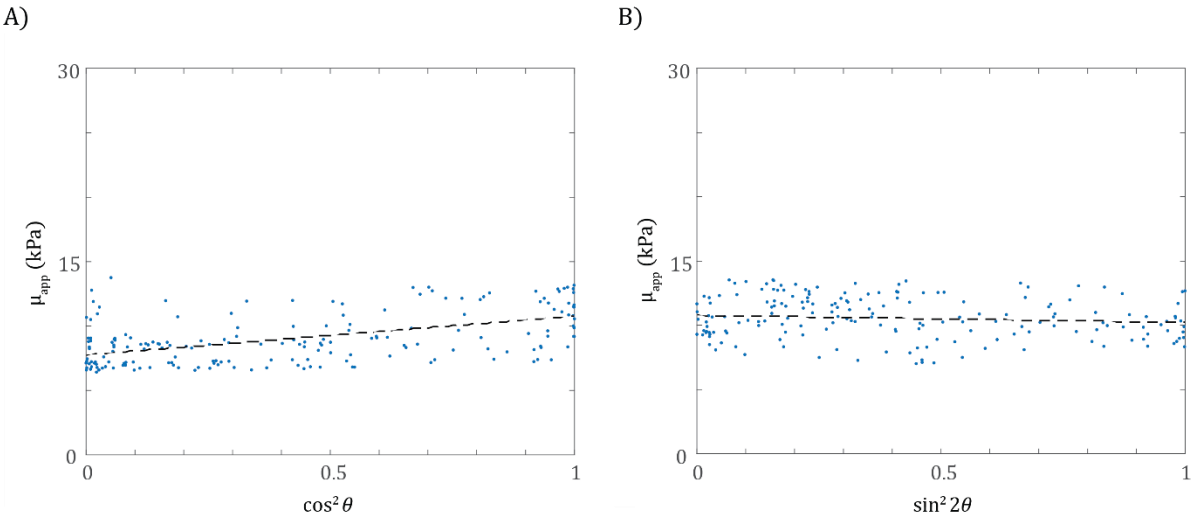

Figure 6.10: Apparent shear modulus, μ_{app}, of all slow and fast voxels from one chicken sample (two MR-HUM experiments, (A-B) and all (n=4) samples (C-D) using DF-LDI. Each dot represents one voxel that met the slow (A and C) or fast (B and D) criteria for DF-LDI analysis. The black dashed line represents the multiple linear regression model for the estimated material parameters found using DF-LDI. (A) Apparent shear modulus in slow voxels for one chicken sample. (B) Apparent shear modulus in fast voxels for one chicken sample.

Figure 6.11 shows the results from DF- LDI after the parameter estimation using the multiple linear regression function in MATLAB. Each of the estimates is shown with its 95% confidence interval. The results from a multiple linear model regression model using slow and fast voxels from all four tissue samples are shown by black diamonds. Table 6.6 shows the estimated parameter values, together with their standard error, from the multiple linear regression model using data from all four samples together (black diamonds from Figure 6.11).

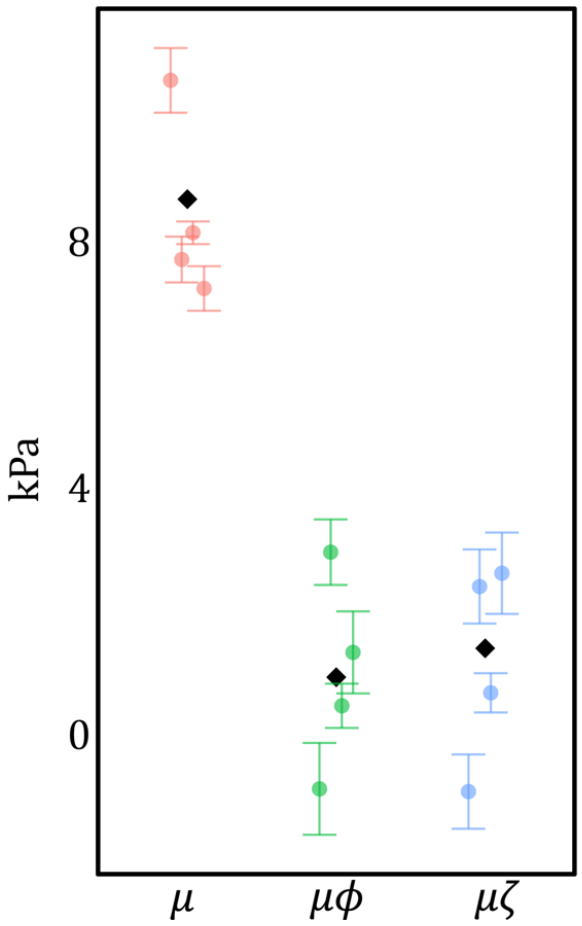

Parameter	Estimated
μ [kPa]	8.48 ± 1.30
$\mu\phi$ [kPa]	1.03 ± 1.39
$\mu\zeta$ [kPa]	1.25 ± 1.43
ϕ	0.142 ± 0.173
ζ	0.171 ± 0.180

Figure 6.11: Results of DF- LDI anisotropic parameter estimation for all four chicken breast samples used in the analysis. (A) Estimates of $\mu, \mu\phi,$ and $\mu\zeta$ for each of the four samples (dots) are plotted with their 95% confidence intervals. Black diamonds show the parameter estimates from all four samples are included together in the multiple linear regression model. A total of 5,572 voxels were used in the linear model fit of the four samples ($R^2 = 0.0394$).

Table 6.6: Average estimated parameter values from the DF-LDI analysis of the four chicken samples. Values are shown with the standard deviation. $\mu, \mu\phi,$ and $\mu\zeta$ are in units of kPa; ϕ and ζ are unitless.

6.4.4 Experiment – Phase Gradient (PG)

Shear wave displacement and curl fields were calculated from the phase images from the MR-HUM scan (Chapter 2.3.2.3). Eigenvalues and eigenvectors of the diffusion tensor, which correspond to principal diffusivity values and directions, were obtained from the DTI scan and used to estimate fractional anisotropy (FA) (Eq. 2.58) and fiber direction ($\boldsymbol{a}$). Section 5.4.2 shows the displacements, fiber direction, propagation direction, and polarization directions from the MR-

HUM and DTI scan for one chicken sample actuated at two different angles to the fiber. Voxels were excluded from the estimation if they did not meet the inclusion criteria (Table 6.1). The shear waves were classified as slow or fast, as explained in 6.3.3.2 (Table 6.3). Figure 6.12 and Figure 6.13 show the results of the PG analysis for the chicken breast sample in which actuation was 51° and 87° to the fiber direction at 400 Hz. Images are from a slice near the center of actuation (same samples are shown in 5.4.3 and 6.4.3). Figure 6.12 and Figure 6.13 show the results of initial voxel classification for displacement (U: panels A-B) and curl (Γ: panels C-D), masked with by inclusion criteria (Table 6.1) for the $\beta = 51°$ and $\beta = 87°$ cases at 400 Hz. Phase angle (ψ) was calculated from the slow (Γ_s) and fast (Γ_f) curl components. Figure 6.12E-F and Figure 6.13 E-F show the phase of the shear wave for the two cases; arrows represent the propagation direction for the voxels that match all inclusion criteria for slow and fast waves. After all masking was performed, the angle between propagation direction and fiber direction (θ) and apparent shear modulus (μ_0) were found for slow or fast voxels based on the classification criteria (Table 6.3). Figure 6.12 and Figure 6.13 G-J show the categorization at one slice for the two cases. The majority of the voxels were classified as fast for the $\beta = 51°$ case and slow for the $\beta = 87°$ case.

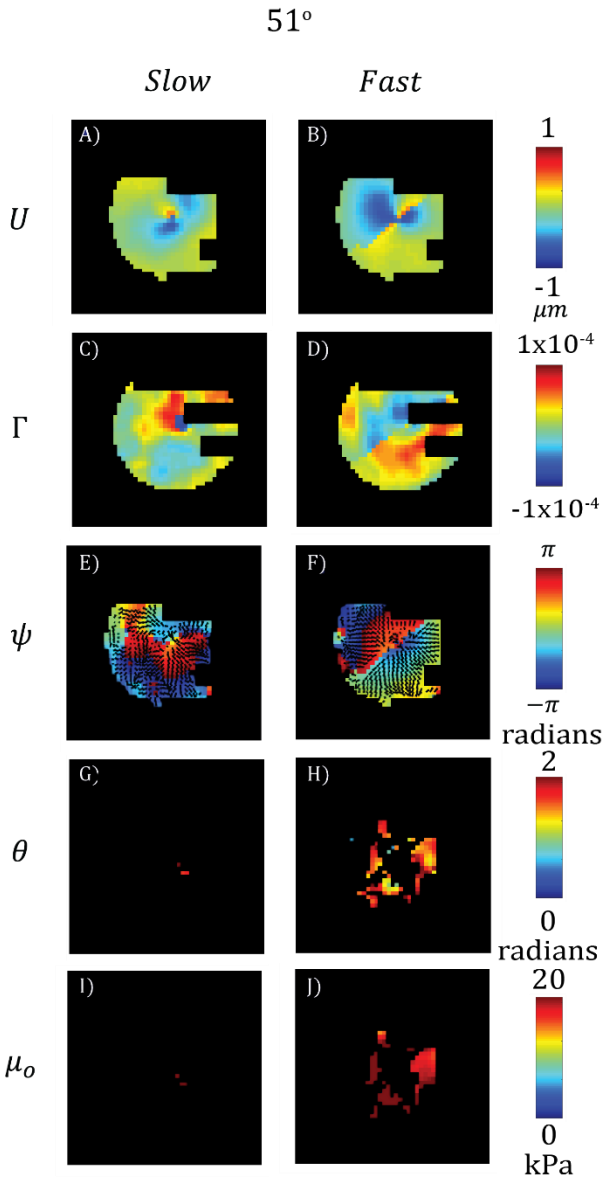

Figure 6.12: Results from PG analysis of MR-HUM data from chicken breast sample with actuation at $\beta = 51°$ to fiber direction at 400 Hz. Voxels were masked based on inclusion criteria from Table 6.1. Images are from the slice near the center of actuation normal to the *z*-axis. (A) Displacement field component (U_s) contributed by shear waves with slow polarization. (B) Displacement field component (U_f) due to shear waves with fast polarization. (C) Curl field component (Γ_s) due to shear waves with slow polarization. (D) Curl field component (Γ_f) due to shear waves with fast polarization. (E) Phase angle (ψ) of slow shear wave curl field, U_s. Black arrows represent the propagation direction. (F) Phase angle (ψ) of fast shear wave curl field, U_f. Black arrows represent the propagation direction. (G) Angle between propagation direction and fiber direction (θ) for slow voxels. Voxels that did not meet classification criteria were masked out (Table 6.3). (H) Angle between propagation direction and fiber direction (θ) for fast voxels. Voxels that did not meet classification criteria were masked out (Table 6.3). I) Apparent shear modulus (μ_{app}) in slow voxels. Voxels that did not meet classification criteria were masked out (Table 6.3). (J) Apparent shear modulus (μ_{app}) categorized by fast polarization. Voxels that did not meet classification criteria were masked out (Table 6.3).

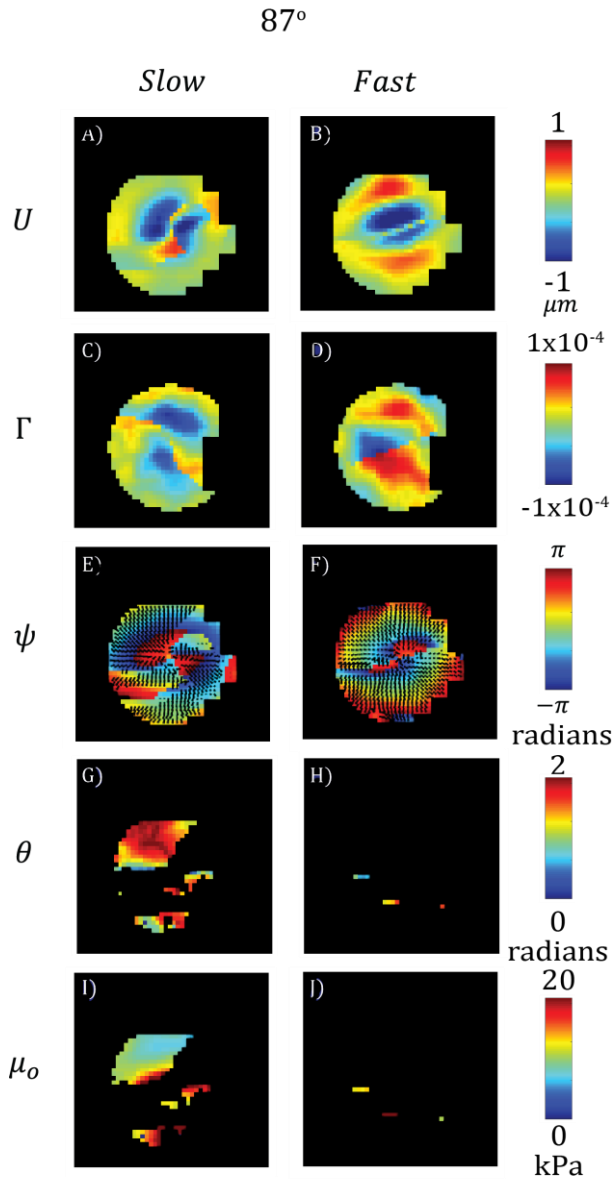

Figure 6.13: Results from PG analysis of MR-HUM data from chicken breast sample with actuation at $\beta = 87°$ to fiber direction at 400 Hz. Voxels were masked based on inclusion criteria from Table 6.1. Images are from the slice near the center of actuation normal to the *z*-axis. (A) Displacement field component (U_s) contributed by shear waves with slow polarization. (B) Displacement field component (U_f) due to shear waves with fast polarization. (C) Curl field component (Γ_s) due to shear waves with slow polarization. (D) Curl field component (Γ_f) due to shear waves with fast polarization. (E) Phase angle (ψ) of slow shear wave curl field, U_s. Black arrows represent the propagation direction. (F) Phase angle (ψ) of fast shear wave curl field, U_f. Black arrows represent the propagation direction. (G) Angle between propagation direction and fiber direction (θ) for slow voxels. Voxels that did not meet classification criteria were masked out (Table 6.3). (H) Angle between propagation direction and fiber direction (θ) for fast voxels. Voxels that did not meet classification criteria were masked out (Table 6.3). I) Apparent shear modulus (μ_{app}) in slow voxels. Voxels that did not meet classification criteria were masked out (Table 6.3). (J) Apparent shear modulus (μ_{app}) categorized by fast polarization. Voxels that did not meet classification criteria were masked out (Table 6.3).

After slow and fast classification, all slow and fast voxels were used in the parameter estimation using the multiple linear regression model from MATLAB. Figure 6.14 shows the apparent shear modulus voxels classified as slow or fast versus the angle for one chicken sample (shown in above figures) using PG.

A total of six samples were used in the analysis. Samples were excluded if fewer than 150 voxels from the two combined MR-HUM experiments met inclusion criteria for the anisotropic parameter estimation, or if $p > 0.05$ for any parameter in the multiple linear model regression model.

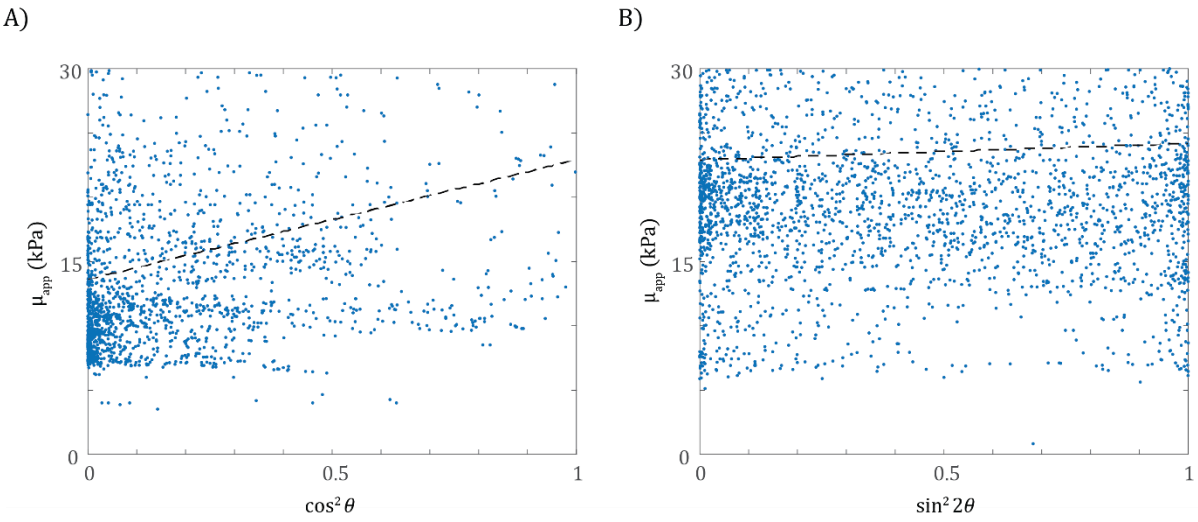

Figure 6.14: Apparent shear modulus, μ_{app}, estimated by PG analysis from one chicken sample (two MR-HUM experiments, panels A-B) and all (n=6) samples (panels C-D). Each dot represents one voxel that met the slow (A and C) or fast (B and D) criteria for PG analysis. The black dashed line represents the multiple linear regression model for the estimated material parameters found using PG. (A) Apparent shear modulus in slow voxels for one chicken sample. (B) Apparent shear modulus in fast voxels for one chicken sample.

Figure 6.15 shows the results from PG method after the parameter estimation for the chicken samples using MATLAB's linear regression model. Each of the sample is plotted with the 95% confidence interval. A multiple linear regression analysis was also run using voxels from all six chicken samples (shown in black diamonds).

Table 6.7 shows the estimated parameters with their standard error from the linear regression model using all six samples together (black diamonds from Figure 6.15).

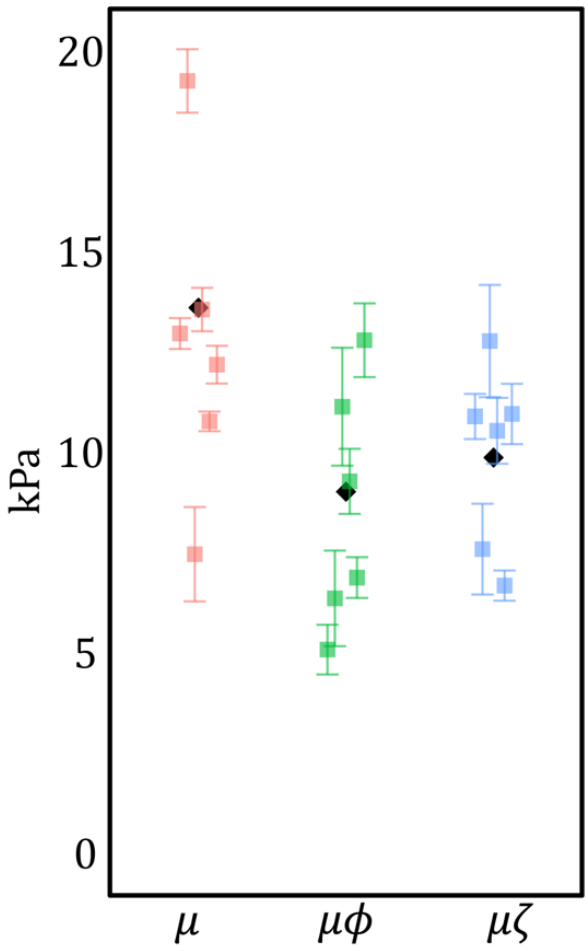

Parameter	Estimated
μ [kPa]	12.74 ± 3.5
$\mu\phi$ [kPa]	8.63 ± 2.73
$\mu\zeta$ [kPa]	9.95 ± 2.10
ϕ	0.765 ± 0.399
ζ	0.874 ± 0.408

Figure 6.15: Results of PG anisotropic parameter estimation for all six chicken breast samples used in the analysis. (A) Estimates of $\mu, \mu\phi,$ and $\mu\zeta$ for each of the six samples (dots) are plotted with their 95% confidence intervals. Black diamonds show the parameter estimates if voxels from all six samples are included together in the multiple linear regression model. A total of 30,705 voxels were used in the linear model fit of the four samples ($R^2 = 0.104$).

Table 6.7: Average estimated parameter values from the PG analysis of the six chicken samples. Values are shown with the standard deviation. $\mu, \mu\phi,$ and $\mu\zeta$ are in units of kPa; ϕ and ζ are unitless.

6.5 Discussion and Conclusions

This chapter explored anisotropic parameter estimation using two different analysis methods. The two analysis methods, directional filtering with local direct inversion (DF-LDI) and phase gradient

(PG) were used to analyze simulated and experimental MR-HUM data. Simulations provide a means for rigorous assessment of the ability of each method to estimate parameters in the absence of noise or other imperfections of real experimental data.

Based on results using data from the two simulations, DF-LDI appeared to provide better estimates of the baseline shear modulus, μ, however it consistently underestimated the shear and tensile anisotropy, ϕ and ζ. PG provided better estimates of the shear and tensile anisotropy parameters, ϕ and ζ, but consistently over-estimated the baseline shear modulus, μ. Figure 6.16 shows a comparison of the multiple linear regression results from simulations for DF-LDI (circles), PG (squares), to the exact values (simulation inputs; black diamonds) for brain-like tissue (A) and muscle-like tissue (B). The 95% confidence intervals for each estimate are also shown for the DF-LDI and PG results. Thus, even for ideal (simulated) data, anisotropic parameter estimation methods remain imperfect.

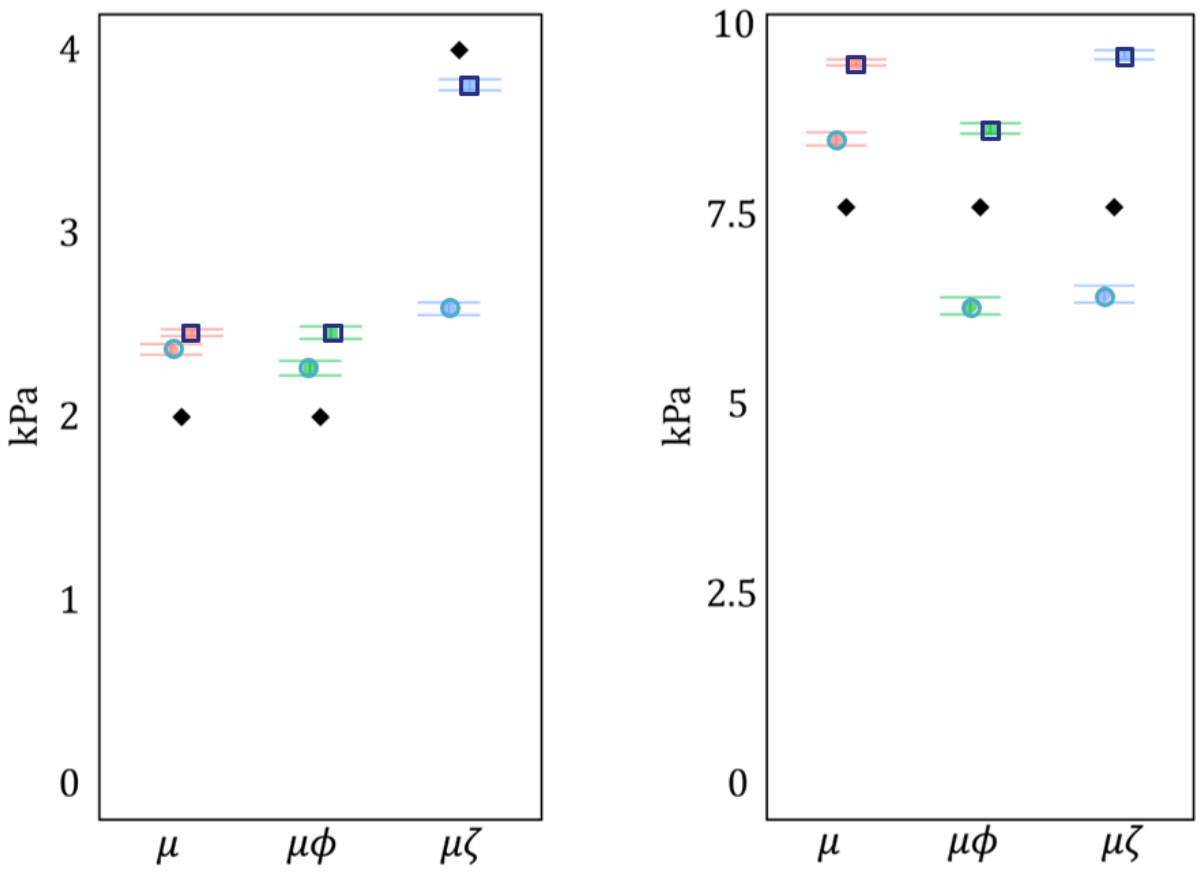

Figure 6.16: Comparison of anisotropic parameter estimates from DF-LDI and PG methods applied to data from simulations. Exact (input) parameter values are shown by black diamonds. Estimated parameters and 95% confidence intervals are shown for DF-LDI (circles) and PG (squares). (A) Results from simulations with brain-like stiffness. (B) Results from simulations with muscle-like stiffness.

When these methods were applied to experimental data, non-ideal features of the data amplified the errors in these two analysis methods. The PG method appeared to be most affected, exhibiting a large spread in values for the baseline shear modulus. Part of this was caused by "wrapping" in phase estimates, which led to large discontinuities in phase estimates. A better method of smoothing or unwrapping might increase the reliability of this method. In addition, the phase gradient is computed by numerical differentiation, which has intrinsic error due to discretization, and amplifies the effects of noise.

DF-LDI is limited by the resolution and accuracy of apparent shear modulus estimates. Currently, the use of an isotropic viscoelastic LDI method with large ($5 \times 5 \times 5$ mm^3) smoothing kernels contributes to error in the anisotropic parameters. In addition, directional filters have a finite bandwidth, so that estimates of propagation direction have limited precision.

In the PG method, many more voxels were retained in the analysis compared to DF-LDI. Samples analyzed using PG had on average 4,900 voxels for the parameter estimation step, while samples analyzed using DF-LDI had only 1,400 voxels on average. This is because the PG method does not exclude voxels that have both slow and fast components as long as each component meets the criteria for inclusion.

From this experiment and analysis, chicken breast was observed to be mildly anisotropic (by DF-LDI) or moderately anisotropic (by PG) in both shear and tensile modulus. The experimental results are consistent with previous studies on turkey breast and cardiac muscle, as well as preliminary direct testing on chicken breast. Schmidt et al. estimated the anisotropic parameters of turkey breast using MRE and dynamic shear testing (DST). For MRE, they estimated $\mu \sim 33$ kPa, $\phi \sim 1.3$, and $\zeta \sim 9.2$ using piezoelectric direct and surface actuation at 800 Hz (the ζ estimate is suspected to be unreliable due to challenges in estimating wavelength). For DST, they estimated $\mu \sim 4$ kPa and $\phi \sim 0.6$ at 20-40 Hz [30]. Preliminary DST testing of chicken breast samples (n=7) provided estimates of $\mu = 6.19 \pm 1.71$ kPa and $\phi \sim 0.84 \pm 0.30$ at 25-45 Hz. For a viscoelastic tissue, like chicken breast, the shear modulus of the material is expected to increase with increased frequency. Riek et al. noted the increase in estimated isotropic shear modulus of bovine muscle *ex vivo* from $\mu \sim 12$ kPa at 200 Hz to $\mu \sim 35$ kPa at 800 Hz using MRE [118]. Humphrey et al. performed biaxial testing of resting cardiac muscle. From the data, we were able

to estimate the tensile anisotropy from the elastic stretch region of the equibiaxial test as $\zeta = 0.61 \pm 0.25$ [119]. Preliminary biaxial testing of chicken breast (n=4) provided estimates of $\zeta = 0.93 \pm 0.65$. Figure 6.17 depicts the anisotropic parameters estimated from the previous work and different methods. The large standard deviations and spread of ϕ and ζ estimated from traditional methods (DST, and biaxial testing) demonstrate the complexity of anisotropic parameter estimation. The ground truth is almost impossible to obtain, especially for materials like white matter in the brain. Because of this, both (i) verification via simulation and (ii) extensive comparison between approaches provide important evidence for viability of the anisotropic parameter estimation method.

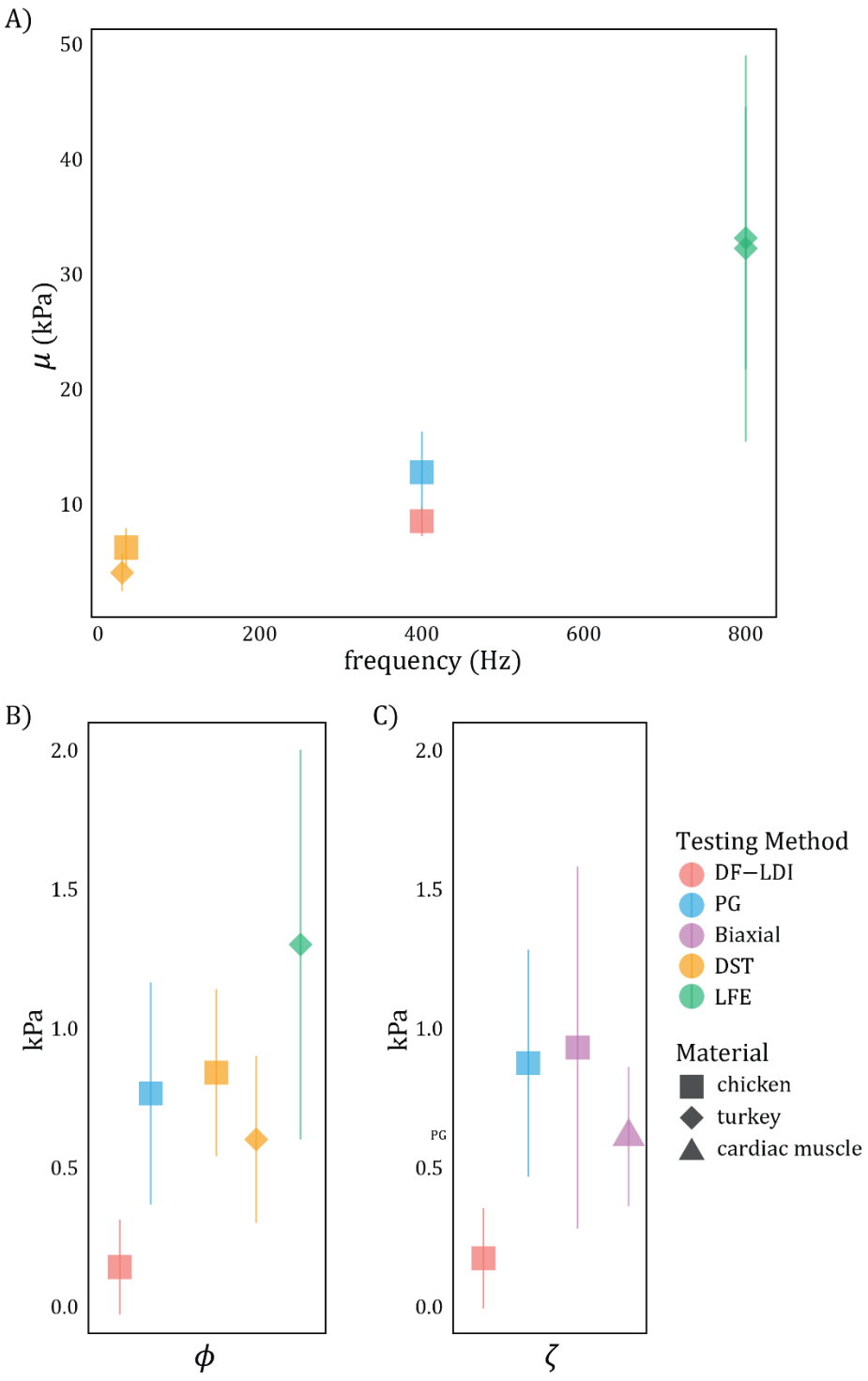

Figure 6.17: Comparison of estimated anisotropic parameters μ, ϕ, and ζ from various testing methods and muscle types with their standard deviations. MR-HUM is the only method that estimated all three parameters from the same sample. (A) Estimated μ from DST (chicken and turkey), DF-LDI (chicken), PG (chicken), and MRE using LFE (turkey [30]). Muscle tissue is viscoelastic, which means μ is expected to increase frequency. (B) Estimated ϕ from DST (chicken and turkey [30]), DF-LDI (chicken), PG (chicken), and MRE using LFE (turkey [30]). (C) Estimated ζ from biaxial testing (chicken and cardiac muscle [119]), DF-LDI (chicken), and PG (chicken).

6.6 Summary

This chapter demonstrated the application of MR-HUM as an alternative approach for anisotropic parameter estimation and explored two analysis methods, DF-LDI and PG. Although both analysis methods have intrinsic limitations, the two approaches provide estimates of anisotropic parameters that are reasonably accurate in MR-HUM simulations. When applied to data from MR-HUM experiments, estimates of shear modulus and shear anisotropy are similar to corresponding measurements from direct mechanical testing. Combining the analysis approaches, or using inverse modeling (the focus of future work), may further improve results.

Chapter 7: Summary and Outlook

7.1 Summary of Thesis

This thesis focuses on estimation of material property of brain tissue using magnetic resonance elastography (MRE) and on work to extend MRE to account for anisotropy in nearly incompressible transversely isotropic (NITI) materials.

Chapter 1 presented the motivation for material property estimation in soft tissue. It also included an overview of relevant prior work in modeling, MRE, anisotropic parameter estimation, and focused ultrasound (FUS). The specific aims for the thesis are also introduced in Chapter 1.

Chapter 2 reviewed the theoretical concepts that underlie anisotropic MRE. This theoretical overview covers the basic principles of continuum mechanics and wave motion, along with underlying principles of imaging and image analysis procedures.

Chapter 3 established the importance of *in vivo* material property estimation methods by illustrating and quantifying the difference between *in vivo* and *ex vivo* estimates (Aim 1). The results described in Chapter 3 thus demonstrate that, in order to estimate anisotropic material properties for living biological tissues like the brain, it is necessary to develop noninvasive methods for *in vivo* measurement.

Chapter 4 introduced a method for anisotropic MRE based on directional filtering and local direct inversion (DF-LDI) that was used to estimate anisotropic parameters from waves excited by external surface actuation (Aim 2). This method was shown to work well for simulated data, but when applied to experimental *in vivo* brain data, the parameter estimates were inconclusive. The

data and analysis suggest a degree of tissue anisotropy, but confidence in parameter estimates was low. The results from this study motivated the exploration of a new MRE method, MR imaging of harmonic ultrasound-induced motion (MR-HUM).

Chapter 5 described the experimental implementation of MR-HUM, including instrumentation and procedures for MR-compatible FUS. Using this implementation, harmonic shear waves produced with FUS were successfully measured using MRI.

Chapter 6 described the application of this approach for estimating anisotropic parameters in a NITI material. Two methods, DF-LDI and phase gradient (PG), were evaluated on data from a simulation of an MR-HUM experiment in anisotropic soft tissue (Aim 3). Based on the simulation results, the methods have complementary strengths. Both methods were applied to MR-HUM experimental data of *ex vivo* chicken breast, a material that appears clearly to be transversely isotropic. The DF-LDI and PG methods both yielded estimates of shear modulus of correct order along with a moderate shear and tensile anisotropy.

Despite our work to improve anisotropic MRE, there are still limitations that motivate further work. Some of these limitations are from the fundamental assumptions that underlie the decomposition of displacement fields into slow and fast shear waves. Strictly speaking, these pure wave modes exist only in a uniform infinite domain. No experimental system is an infinite domain.

In addition, many biological tissues, including brain tissue, are heterogeneous. The X-Box simulation showed that the accuracy of the DF-LDI method was degraded by heterogeneity; even with noise-free data the method did not provide accurate estimates of material properties of the NITI tracts. Heterogeneity was also likely a contributing factor to the inconclusive anisotropic

estimates for white matter of porcine brain tissue (Chapter 4). For heterogeneous tissues like brain, the difference in material properties between white matter and gray matter appear to be on the order of 20-40% [83]. These differences can be obscured by noise, especially if they exist in small regions. When heterogeneities are smaller than the wavelength of the shear wave, as seen *in vivo* and some simulations, subtle or moderate differences in properties can difficult to detect with certainty.

The DF-LDI method described in this thesis is limited by the need to separate wave fields into regions or voxels that exhibit *either* slow or fast shear waves, *but not both*. This reduces the number of voxels that can be used in parameter estimation, since voxels that do not exhibit pure slow or fast modes are excluded. The PG method uses all voxels in which the displacement contains sufficient contributions from slow and fast waves, even when both are present. However, the PG method is subject to inaccuracies due to numerical differentiation and phase wrapping.

Even with these limitations, the studies described in this thesis have clearly identified problems specific to MRE of anisotropic tissues and have begun to address them. More work is necessary to continue to improve anisotropic parameter estimation.

7.2 Future Work

Next steps for this project include the extension of MR-HUM to heterogeneous tissue, like the brain. Using the experimental setup described in Chapter 5, anisotropic material properties of *ex vivo* brain tissue white matter (as in Chapter 3) could be estimated. MR-HUM could also be extended to *in vivo* brain tissue. Preliminary MR-HUM testing has been performed on the mouse brain *in vivo,* and FUS has been applied to the brains of domestic pigs *in vivo*. Finally, modifying

our approach to include a more sophisticated inversion method, like inverse finite element method [120] (which does not rely on separating slow and fast shear waves) could improve the estimation of anisotropic material parameters.

7.3 Summary of Achievements

Although there is more work to be done to successfully incorporate anisotropy into MRE, this this work successfully led to improvements to anisotropic MRE. During this thesis, I demonstrated that, to estimate anisotropic material properties for living biological tissues like the brain, we need noninvasive methods for *in vivo* measurement. I introduced a method for anisotropic MRE based on directional filtering and local direct inversion (DF-LDI) and used it to estimate anisotropic parameters from waves excited by external actuation. Lastly, I implemented a novel localized, noninvasive actuation system, MR-HUM, and used it to estimate anisotropic material parameters in soft tissue.

Appendix A: Error Analysis

The table below summarizes differences between *in vivo* and *ex vivo* experiments and their possible effects.

Table A.1: Error analysis comparing *in vivo* and *ex vivo* experiments

Potential error source	Comments	*In vivo*	*Ex vivo*
Wave amplitude	Shear modulus is estimated from the wave length. Differences in wave amplitude should not directly affect modulus estimates. In both methods, waves had enough amplitude to produce visible shear waves. In the small-strain regime we do not expect modulus to depend on amplitude.	Wave amplitude ~1.5μm Strain amplitude ~$2x10^{-4}$	Wave amplitude ~15μm Strain amplitude ~$2x10^{-3}$
Dominant wave direction	Both methods produced shear wave polarization displacements perpendicular to the dominant fiber direction, oriented right-left, of the corpus callosum. Although the tissue is actuated in different anatomical directions, the tissue is actuated similarly relative to the dominant fiber axis in both situations.	Dominant actuation direction: anterior-posterior (AP)	Dominant actuation direction: superior-inferior (SI)
Temperature	Temperature difference could cause differences in tissue properties. However, cooling of viscoelastic tissue generally leads to stiffening, so the temperature difference is more likely to mask differences in stiffness between the (apparently stiffer) *in vivo* and softer *ex vivo* tissue. The fact that a difference is still observed tends to support the paper's conclusions that *in vivo* tissue is stiffer.	Body temperature ~37°C	Room temperature ~21°C
Excitation method	Excitation differences created differences in propagation direction. *In vivo* waves were excited externally and propagated inward from the skull. *Ex vivo* waves were	External actuation of skull by vibration of jaw	Axial excitation by central rod embedded in tissue

	excited in the center of the tissue and propagated outward (the rod created an internal boundary which was removed through erosion of voxels). The direction of wave propagation should not have an effect since fiber orientation was similar.		
Voxel size	Voxel size affects the physical size of the estimation kernel for LDI, and the size of the eroded regions at boundaries. Kernel size does affect parameter estimates. Estimates converge as kernel size increases; kernel size is limited by sample size. Estimated effect: Results vary 3-7% (*ex vivo*) and 7-10% (*in vivo*) between kernel sizes of 5x5x5 to 7x7x7 voxels.	1.5 mm^3 isotropic voxels	1 mm^3 isotropic voxels
Boundary conditions	Boundary conditions are different, but comparable. The *in vivo* brain is surrounded by cerebrospinal fluid (CSF) and the skull. The *ex vivo* brain is surrounded in gelatin/glycerol and a hard plastic case. The boundaries should have only small effects on the conclusions of the study for two reasons: (1) In both cases, we analyzed interior ROIs, removed from the boundaries. All results are based on these interior ROIs. (2) Observed differences in estimated properties are greater at higher frequencies (with short wavelengths) at which the effects of boundaries are less likely to be important than at lower frequencies (longer wavelengths).	Skull and cerebral spinal fluid (CSF)	Gelatin/glycerol and plastic cylinder case

Appendix B: Linear Mixed Model

The multivariate regressions of storage modulus (μ') and loss modulus (μ'') were performed (Matlab R2017, Statistics Toolbox) using a linear mixed-effects model with random subject effects and fixed effects of group (*in vivo* vs. *ex vivo*) and frequency in the form:

$$y_i = a + b_1 x_{1i} + b_2 x_{2i} + b_3 x_{1i} x_{2i}. \quad \text{(B.1)}$$

In this model, y_i is μ' or μ'', a is the intercept, b_1 is the slope of the group variable, x_{1i} is the value of the group variable, b_2 is the slope of the frequency variable, x_{2i} is the value of the frequency variable, and b_3 is the slope of the interaction between group and frequency. The value of the group variable defines whether the tissue is *in vivo* ($x_{1i} = 1$) or *ex vivo* ($x_{1i} = 0$). Tables B.1 and B.2 outline the results of the analysis of μ' and μ'', respectively. The slopes between μ' *in vivo* and *ex vivo* were significantly different ($p < 0.0001$) and frequency was a good predictor of the data ($p < 0.0001$). No significant differences were observed between μ'' *in vivo* and *ex vivo* over this frequency range ($p = 0.285$). The linear mixed-effects model is plotted with μ' and μ'' estimates in Figure 8.

Table B.1: Results of multivariate regression of storage modulus (μ') using a linear mixed-effects model with random subject effects

Effect	Variable	Estimate	Standard Error	Alpha (lower, upper)	P
Intercept	a	0.361	0.128	0.05 (0.102, 0.620)	0.007
Group	b_1	-0.926	0.178	0.05 (-1.283, -0.568)	<0.0001
Frequency (Hz)	b_2	0.0140	0.0007	0.05 (0.0126,0.0154)	<0.0001
Group*Frequency	b_3	0.0143	0.0016	0.05 (0.0110,0.0176)	<0.0001

Table B.2: Results of multivariate regression of loss modulus (μ'') using a linear mixed-effects model with random subject effects

Effect	Variable	Estimate	Standard Error	Alpha (lower, upper)	P
Intercept	a	-0.309	0.070	0.05 (-0.448, 0.167)	<0.0001
Group	b_1	-0.108	0.100	0.05 (-0.310, -0.093)	0.285
Frequency (Hz)	b_2	0.00592	0.00035	0.05 (0.00522,0.00662)	<0.0001
Group*Frequency	b_3	0.00324	0.00091	0.05 (0.00140,0.00508)	0.0009

Appendix C: Summary of Rheological Model Fitting

Several rheological models were fitted to the complex shear modulus estimates from both *in vivo* and *ex vivo* data. Classic rheological models do not fit the estimated moduli well (Table C.1), possibly due to poroelastic behavior [121]. However, as noted by Testu et al. [122], dual power-law models fitted separately to μ' and μ'' fit the frequency-dependent shear moduli much better than the classic (springpot) power-law.

Table C.1: Summary of rheological data fitting.

Model	***In vivo***		***Ex vivo***	
	Parameters	R^2	Parameters	R^2
Power law (dual) [122] $\mu' = \kappa_1 \omega^{\alpha_1}$ $\mu'' = \kappa_2 \omega^{\alpha_2}$	$\kappa_1 = 2.88 \times 10^{-4}$ $\alpha_1 = 1.39$ $\kappa_2 = 8.60 \times 10^{-9}$ $\alpha_2 = 2.75$	0.924	$\kappa_1 = 7.93 \times 10^{-3}$ $\alpha_1 = 0.840$ $\kappa_2 = 2.11 \times 10^{-5}$ $\alpha_2 = 1.48$	0.940
Power law (springpot) [123] $\mu^* = \kappa(i\omega)^{\alpha}$	$\kappa = 0.490$ $\alpha = 0.214$	0.168	$\kappa = 0.563$ $\alpha = 0.253$	0.357
Zener [124] $\mu^* = \mu_\infty \frac{1 + d(i\omega\tau)}{1 + i\omega\tau}$	$\mu_\infty = 1.09$ $d = 2.38$ $\tau = 1.77 \times 10^{-3}$	0.257	$\mu_\infty = 1.93$ $d = 2.58$ $\tau = 6.61 \times 10^{-4}$	0.515
Fractional Zener [124] $\mu^* = \mu_\infty \frac{1 + d(i\omega\tau)^{0.5}}{1 + i\omega\tau}$	$\mu_\infty = 0.473$ $d = 7.88$ $\tau = 9.64 \times 10^{-4}$	0.178	$\mu_\infty = 0.722$ $d = 10.89$ $\tau = 2.60 \times 10^{-4}$	0.377
Generalized Maxwell [90] $\mu^* = \mu_\infty + \frac{i\omega\tau_1\mu_1}{1 + i\omega\tau_1} + \frac{i\omega\tau_2\mu_2}{1 + i\omega\tau_2}$	$\mu_\infty = 1.09$ $\mu_1 = 3.00 \times 10^{-15}$ $\mu = 1.51$ $\tau_1 = 2.84 \times 10^{-5}$ $\tau_2 = 1.77 \times 10^{-3}$	0.257	$\mu_\infty = 1.93$ $\mu_1 = 3.15 \times 10^{-14}$ $\mu_2 = 3.05$ $\tau_1 = 3.48 \times 10^{-5}$ $\tau_2 = 6.61 \times 10^{-4}$	0.515

Units: *Power law*: κ, κ_1, κ_2 (kPa-s$^{\alpha}$), α (non-dimensional). *Zener*, *fractional Zener*, *and generalized Maxwell*: μ_∞, μ_1 μ_2 (kPa); d (non-dimensional); τ, τ_1, τ_2 (s).

Appendix D: MR Thermometry for MR-HUM

As noted in Chapter 5, one of the drawbacks of MR-HUM is sample heating, which is most prevalent at the focus of the ultrasound transducer. MR thermometry can be used to monitor the level of heating within a tissue due to focused ultrasound (FUS) [125]. MR thermometry is based on using the proton resonant frequency shift (PRF shift) to measure the change in tissue temperature [126, 127].

MRI can detect changes in temperature using phase mapping [125, 127]. Changes in temperature are proportional to changes in phase, as described by

$$\Delta T = \frac{\phi(T) - \phi(T_0)}{\gamma \alpha B_0 \, TE} \tag{D.1}$$

where ΔT is the change in temperature, $\phi(\mathrm{T})$ is the current phase map, $\phi(\mathrm{T_0})$ is the reference phase map, γ is the gyromagnetic ratio ($\gamma = 42.58$ MHz/T), α is the temperature-dependence coefficient ($\alpha = -0.01\mathrm{x}10^{-6}$ °C^{-1}), B_0 is the magnetic field strength ($B_0 = 4.7\ T$ for this study), and TE is the echo time ($TE = 0.004\ s$ for this study). The temperature coefficient of PRF shift is almost constant and independent of tissue types and thermal history. The reference map allows for the separation of phase changes due to temperature increase versus static spatial variations of phase.

There are several sources of temperature-independent phase changes that can lead to error in the estimate of ΔT. These include motion of the subject (or sample), gradual fluctuations of the center frequency of the MR scanner due to environmental changes, dynamic temporal and spatial

fluctuations of the magnetic field due to magnet heating [125, 126, 128-133]. It has been shown that B_0 drift can result in apparent temperature change on the order of 7°C/min and subject motion can lead to errors up to 265°C [125, 129, 134].

MR thermometry for MR-HUM poses some challenges. Typically, an MR thermometry sequence is performed during FUS so the temperature can be constantly monitored. However, since MR-HUM creates motion in the tissue, so that most of the phase change observed is due to the harmonic motion, instead of the temperature change.

Thermometry could also be performed before and after MR-HUM and the change in phase between those two scans could be subtracted. However, phase drift during the time delay in this procedure may introduce phase variations which may not be solely related to temperature change. One potential way to avoid this is to use phantoms that remain at a constant temperature as references. However, those references do not undergo the motion of MR-HUM that could lead to phase offset after the scan. Figure D.1 shows the heating and cooling cycles through differences in phase taken before and after MR-HUM scans. Since the phase maps are acquired with gaps of 5-15 minutes, phase drift and other sources of error likely contribute to the change of phase, as well as changes of temperature.

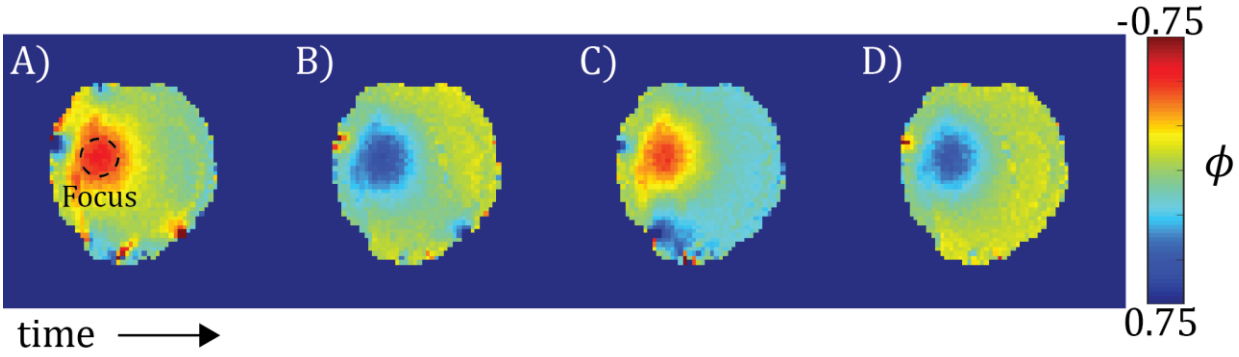

Figure D.1: Change in phase for one slice of a 48mm diameter PVA disk over two heating and cooling cycles. Negative phase change is related to a positive temperature change. Errors in phase have not been sufficiently addressed, so resulting phase changes shown above should only be interpreted qualitatively, not quantitatively. If these values of phase change are put into Equation D.1, the temperature values range from about ± 11. (A) Change in phase after an MR-HUM scan of ~10 minutes. An increase in temperature can be seen at the focus (outlined by black dotted circle). (B) Change in phase after waiting post-MR-HUM scan for ~14 minutes. Cooling is observed in focal region. (C) Change in phase after an MR-HUM scan of ~10 minutes. Increase in temperature can be seen at the focus. (D) Change in phase that occurred after waiting post-MR-HUM scan for ~5 minutes. Cooling is observed in the focal region.

Although MR thermometry is a useful tool in quantifying temperature changes in MR samples, more work is needed before it can accurately detect changes in temperature from MR-HUM. A detailed investigation should be performed with thermocouples and thermal constant phantoms to determine accurate measurements. This will need to be studied further as MR-HUM moves to *in vivo* testing. I did not include quantitative MR thermometry in this thesis. Cognizant of the potential effects of heating, we used shortened MRE sequences at power levels that did not cause externally detectable changes in color or temperature of the sample.

Appendix E: Parameter Sensitivity Analysis

A sensitivity analysis of the effect of polarization threshold for select parameter estimates was performed for MR-HUM simulations and experiments using DF-LDI and PG analysis.

E.1 DF-LDI Simulation

The sensitivity analysis from DF-LDI is shown in Table E.1. Increasing the polarization threshold from 0.5 to 0.9 deceases the error by 10-30% for all parameters. Increasing the polarization threshold does severely limit the number of voxels used in the inversion from 14,607 to 2,807 voxels.

Table E.1: Sensitivity analysis for polarization threshold for MR-HUM simulation set. A kernel size of 5x5x5 was used for this data. Input values are $\mu = 7.50$ kPa, $\phi = 1.00$, and $\zeta = 1.00$.

Polarization Threshold (pol_{thresh})	μ [kPa]	% error μ	ϕ	% error ϕ	ζ	% error ζ	Number of voxels
0.5	8960	19.5	0.57	43.2	0.56	44.3	14607
0.6	8720	16.3	0.64	36.0	0.63	36.7	11616
0.7	8472	13.0	0.71	28.8	0.72	27.6	8624
0.8	8251	10.0	0.78	22.3	0.81	19.4	5849
0.9	8167	8.9	0.78	21.9	0.86	13.7	2807

A sensitivity analysis of the effect of amplitude threshold for parameter estimates from DF-LDI is shown in Table E.2. Changing the amplitude threshold has no effect on the parameter estimation for the simulation with ideal data.

Table E.2: Sensitivity analysis for amplitude threshold for MR-HUM simulation set. Kernel size of 5x5x5 and $pol_{thresh} = 0.75$ was used for this data. Input values are $\mu = 7.50$ kPa, $\phi = 1.00$, and $\zeta = 1.00$.

Amplitude Threshold (A)	μ [kPa]	% error μ	ϕ	% error ϕ	ζ	% error ζ	Number of voxels
0.05	8388	11.8	0.74	25.9	0.76	24.1	7304
0.1	8388	11.8	0.74	25.9	0.76	24.1	7304
0.2	8388	11.8	0.74	25.9	0.76	24.1	7304

A sensitivity analysis of the effect of kernel size for parameter estimates from DF-LDI is shown in Table E.3. Decreasing the kernel size improves estimations for all parameters.

Table E.3: Sensitivity analysis for kernel size for MR-HUM simulation set. $A = .01$ and $pol_{thresh} = 0.75$ was used for this data. Input values are $\mu = 7.50$ kPa, $\phi = 1.00$, and $\zeta = 1.00$.

Kernel Size	μ [kPa]	% error μ	ϕ	% error ϕ	ζ	% error ζ	Number of voxels
3	8124	8.3	0.80	20.1	0.82	18.0	7304
5	8388	11.8	0.74	25.9	0.76	24.1	7304
7	8751	16.7	0.67	33.1	0.66	33.8	7304

E.1 PG Simulation

The sensitivity analysis from PG is shown in Table E.4. Increasing the polarization threshold from 0.5 to 0.9 slightly increases the error for all parameters. Increasing the polarization threshold does severely limit the number of voxels used in the inversion from 17,997 to 7,088 voxels. The lowest error appears to be around $pol_{thresh} = 0.6$ to 0.8.

Table E.4: Sensitivity analysis for polarization threshold for MR-HUM simulation set. Input values are $\mu = 7.50$ kPa, $\phi = 1.00$, and $\zeta = 1.00$.

Polarization Threshold (pol_{thresh})	μ [kPa]	% error μ	ϕ	% error ϕ	ζ	% error ζ	Number of voxels
0.5	9418	25.6	0.92	8.1	0.99	1.2	17997
0.6	9389	25.2	0.92	8.1	1.00	0.0	16069
0.7	9382	25.1	0.91	8.7	1.01	0.8	13791
0.8	9387	25.2	0.91	9.2	1.01	1.4	10925
0.9	9528	27.0	0.89	11.1	0.98	1.7	7088

A sensitivity analysis of the effect of amplitude threshold for parameter estimates from PG simulations is shown in Table E.5. Changing the amplitude threshold has a very small effect on the estimated parameters

Table E.5: Sensitivity analysis for amplitude threshold for MR-HUM simulation set. $pol_{thresh} = 0.75$ was used for this data. Input values are $\mu = 7.50$ kPa, $\phi = 1.00$, and $\zeta = 1.00$.

Amplitude Threshold (A)	μ [kPa]	% error μ	ϕ	% error ϕ	ζ	% error ζ	Number of voxels
0.05	9376	25.0	0.91	9.2	1.01	1.2	12535
0.1	9383	25.1	0.91	9.1	1.01	1.1	12501
0.2	9463	26.2	0.89	11.1	1.00	0.1	12400

E.1 DF-LDI Experiment

The sensitivity analysis of the MR-HUM experiment for one sample analyzed by DF-LDI is shown in Table E.6. Increasing the polarization threshold from 0.5 to 0.9 deceases the estimation of the

baseline shear modulus, μ, and increases the estimations for shear and tensile anisotropy, ϕ and ζ. Increasing the polarization threshold does severely limit the number of voxels used in the inversion from 1,927 to 52 voxels.

Table E.6: Sensitivity analysis for polarization threshold for one MR-HUM experiment. A kernel size of 5x5x5 was used for this data.

Polarization Threshold ($\boldsymbol{pol_{thresh}}$)	$\boldsymbol{\mu}$ [kPa]	$\boldsymbol{\phi}$	$\boldsymbol{\zeta}$	Number of voxels
0.5	9033	0.16	0.12	1927
0.6	8768	0.20	0.17	1134
0.7	8229	0.29	0.24	580
0.8	7431	0.45	0.34	223
0.9	6906	0.58	0.37	52

A sensitivity analysis of the effect of amplitude threshold for parameter estimates from DF-LDI is shown in Table E.7. Changing the amplitude threshold has no effect on the parameter estimation for the simulation with ideal data.

Table E.7: Sensitivity analysis for amplitude threshold for one MR-HUM experiment. Kernel size of 5x5x5 and $pol_{thresh} = 0.75$ was used for this data.

Amplitude Threshold ($\boldsymbol{A}$)	$\boldsymbol{\mu}$ [kPa]	$\boldsymbol{\phi}$	$\boldsymbol{\zeta}$	Number of voxels
0.05	7764	0.39	0.32	365
0.1	7764	0.39	0.32	365
0.2	7764	0.39	0.32	365

A sensitivity analysis of the effect of kernel size for parameter estimates from DF-LDI is shown in Table E.8. Decreasing the kernel size improves estimations for all parameters.

Table E.8: Sensitivity analysis for kernel size for one MR-HUM experiment. $A = .01$ and $pol_{thresh} = 0.75$ was used for this data.

Kernel Size	$\boldsymbol{\mu}$ [kPa]	$\boldsymbol{\phi}$	$\boldsymbol{\zeta}$	Number of voxels
3	7196	0.41	0.25	400
5	7764	0.39	0.32	365
7	8765	0.26	0.27	367

E.1 PG Experiment

The sensitivity analysis of the MR-HUM experiment for one sample analyzed by PG is shown in Table E.9. Increasing the polarization threshold from 0.5 to 0.9 increases the estimates for ϕ and ζ. Increasing the polarization threshold does severely limit the number of voxels used in the inversion from 11,208 to 1,117 voxels.

Table E.9: Sensitivity analysis for polarization threshold for one MR-HUM experiment.

Polarization Threshold ($\boldsymbol{pol_{thresh}}$)	$\boldsymbol{\mu}$ [kPa]	$\boldsymbol{\phi}$	$\boldsymbol{\zeta}$	Number of voxels
0.5	13674	0.22	0.20	11208
0.6	14424	0.32	0.29	8949
0.7	14346	0.49	0.55	6397
0.8	13530	0.76	0.97	3627
0.9	15093	0.60	0.96	1117

A sensitivity analysis of the effect of amplitude threshold for parameter estimates from one PG MR-HUM experiment is shown in Table E.10. Changing the amplitude threshold has no effect on the estimated parameters for the values chosen.

Table E.10: Sensitivity analysis for amplitude threshold for one MR-HUM experiment. $pol_{thresh} = 0.75$ was used for this data.

Amplitude Threshold ($\boldsymbol{A}$)	$\boldsymbol{\mu}$ [kPa]	$\boldsymbol{\phi}$	$\boldsymbol{\zeta}$	Number of voxels
0.05	13605	0.69	0.78	5018
0.1	13605	0.69	0.78	5018
0.2	13605	0.69	0.78	5018

References

[1] R. J. Okamoto, E. H. Clayton, and P. V. Bayly, "Viscoelastic properties of soft gels: comparison of magnetic resonance elastography and dynamic shear testing in the shear wave regime," *Physics in Medicine and Biology,* vol. 56, no. 19, p. 6379, 2011.

[2] A. H. S. Holbourn, "Mechanics of Head Injuries," *The Lancet,* vol. 242, no. 6267, pp. 438-441, 1943.

[3] V. E. Johnson, W. Stewart, and D. H. Smith, "Axonal pathology in traumatic brain injury," *Experimental neurology,* vol. 246, pp. 35-43, 2013.

[4] CDC. (2019). *Traumatic Brain Injury & Cuncussion*. Available: https://www.cdc.gov/traumaticbraininjury/index.html

[5] J. A. Langlois, W. Rutland-Brown, and M. M. Wald, "The epidemiology and impact of traumatic brain injury: a brief overview," *The Journal of head trauma rehabilitation,* vol. 21, no. 5, pp. 375-8, Sep-Oct 2006.

[6] R. J. Okamoto, A. J. Romano, C. L. Johnson, and P. V. Bayly, "Insights Into Traumatic Brain Injury From MRI of Harmonic Brain Motion," *Journal of Experimental Neuroscience,* vol. 13, p. 1179069519840444, 2019.

[7] P. V. Bayly, T. S. Cohen, E. P. Leister, D. Ajo, E. C. Leuthardt, and G. M. Genin, "Deformation of the human brain induced by mild acceleration," *Journal of neurotrauma,* vol. 22, no. 8, pp. 845-856, 2005/08/01 2005.

[8] S. Chatelin, A. Constantinesco, and R. Willinger, "Fifty years of brain tissue mechanical testing: from in vitro to in vivo investigations," *Biorheology,* vol. 47, no. 5-6, pp. 255-76, 2010.

[9] K. B. Arbogast and S. S. Margulies, "Material characterization of the brainstem from oscillatory shear tests," *Journal of Biomechanics,* vol. 31, no. 9, pp. 801-807, 1998.

[10] L. E. Bilston, Z. Liu, and N. Phan-Thien, "Linear Viscoelastic Properties of Bovine Brain Tissue in Shear," *Biorheology,* vol. 34, no. 6, p. 8, 1997.

[11] D. W. A. Brands, "The Large Shear Strain Dynamic Behavior of In-Vitro Porcine Brain Tissue and a Silicone Gel Model Material " *Stapp Car Crash Journal,* vol. 44, p. 14, 2000.

[12] S. L. Nicolle, Mourad; Willinger , Rémy "Shear Properties of Brain Tissue over a Frequency Range Relevant for Automotive Impact Situations: New Experimental Results," *Stapp Car Crash Journal,* vol. 48, p. 20, 2004.

[13] M. Hrapko, J. A. van Dommelen, G. W. Peters, and J. S. Wismans, "The influence of test conditions on characterization of the mechanical properties of brain tissue," *Journal of Biomechanical Engineering,* vol. 130, no. 3, p. 031003, Jun 2008.

[14] A. K. Ommaya, "Mechanical properties of tissues of the nervous system," *Journal of Biomechanics,* vol. 1, no. 2, p. 10, 1968.

[15] F. Shen, T. E. Tay, J. Z. Li, S. Nigen, P. V. Lee, and H. K. Chan, "Modified Bilston nonlinear viscoelastic model for finite element head injury studies," *Journal of Biomechanical Engineering,* vol. 128, no. 5, pp. 797-801, Oct 2006.

[16] K. L. Thibault and S. S. Margulies, "Age-dependent material properties of the porcine cerebrum: effect on pediatric inertial head injury criteria," *Journal of Biomechanics,* vol. 31, no. 12, pp. 1119-1126, 1998.
[17] J. Vappou, E. Breton, P. Choquet, C. Goetz, R. Willinger, and A. Constantinesco, "Magnetic resonance elastography compared with rotational rheometry for in vitro brain tissue viscoelasticity measurement," *MAGMA,* vol. 20, no. 5-6, pp. 273-8, Dec 2007.
[18] K. Miller, K. Chinzei, G. Orssengo, and P. Bednarz, "Mechanical properties of brain tissue in-vivo: experiment and computer simulation," *Journal of Biomechanics,* vol. 33, no. 11, pp. 1369-76, Nov 2000.
[19] B. Rashid, M. Destrade, and M. D. Gilchrist, "Mechanical characterization of brain tissue in compression at dynamic strain rates," *Journal of the Mechanical Behavior of Biomedical Materials,* vol. 10, p. 15, 2012.
[20] A. Gefen and S. S. Margulies, "Are in vivo and in situ brain tissues mechanically similar?," *Journal of Biomechanics,* vol. 37, no. 9, pp. 1339-52, Sep 2004.
[21] E. H. Clayton, J. R. Garbow, and P. V. Bayly, "Frequency-dependent viscoelastic parameters of mouse brain tissue estimated by MR elastography," *Physics in Medicine and Biology,* vol. 56, no. 8, pp. 2391-2406, Mar 22 2011.
[22] Y. Feng, E. H. Clayton, Y. Chang, R. J. Okamoto, and P. V. Bayly, "Viscoelastic properties of the ferret brain measured in vivo at multiple frequencies by magnetic resonance elastography," *Journal of Biomechanics,* vol. 46, no. 5, pp. 863-70, Mar 15 2013.
[23] C. L. Johnson *et al.*, "Viscoelasticity of subcortical gray matter structures," *Human Brain Mapping,* vol. 37, no. 12, pp. 4221-4233, Dec 2016.
[24] S. Papazoglou, U. Hamhaber, J. Braun, and I. Sack, "Algebraic Helmholtz inversion in planar magnetic resonance elastography," *Physics in Medicine and Biology,* vol. 53, no. 12, pp. 3147-3158, 2008.
[25] K. Schregel *et al.*, "Demyelination reduces brain parenchymal stiffness quantified in vivo by magnetic resonance elastography," *PNAS,* vol. 109, no. 17, pp. 6650-5, Apr 24 2012.
[26] J. Vappou, E. Breton, P. Choquet, R. Willinger, and A. Constantinesco, "Assessment of in vivo and post-mortem mechanical behavior of brain tissue using magnetic resonance elastography," *Journal of Biomechics,* vol. 41, no. 14, pp. 2954-9, Oct 20 2008.
[27] S. Chatelin *et al.*, "Computation of axonal elongation in head trauma finite element simulation," *Journal of the Mechanical Behavior of Biomedical Materials,* vol. 4, no. 8, pp. 1905-19, Nov 2011.
[28] S. Chatelin, C. Deck, and R. Willinger, "An anisotropic viscous hyperelastic constitutive law for brain material finite-element modeling," *Journal of Biorheology,* vol. 27, no. 1-2, pp. 26-37, 2012.
[29] E. C. Qin *et al.*, "Combining MR elastography and diffusion tensor imaging for the assessment of anisotropic mechanical properties: a phantom study," *Journal of Magenetic Resonance Imaging,* vol. 37, no. 1, pp. 217-26, Jan 2013.
[30] J. L. Schmidt *et al.*, "Magnetic resonance elastography of slow and fast shear waves illuminates differences in shear and tensile moduli in anisotropic tissue," *Journal of Biomechanics,* vol. 49, no. 7, pp. 1042-9, May 03 2016.

[31] D. J. Tweten, R. J. Okamoto, J. L. Schmidt, J. R. Garbow, and P. V. Bayly, "Estimation of material parameters from slow and fast shear waves in an incompressible, transversely isotropic material," *Journal of Biomechanics,* vol. 48, no. 15, pp. 4002-9, Nov 26 2015.
[32] A. A. Badachhape *et al.*, "The Relationship of Three-Dimensional Human Skull Motion to Brain Tissue Deformation in Magnetic Resonance Elastography Studies," *Journal of Biomechanical Engineering,* vol. 139, no. 5, May 01 2017.
[33] I. Sack *et al.*, "The impact of aging and gender on brain viscoelasticity," *NeuroImage,* vol. 46, no. 3, pp. 652-657, 2009.
[34] R. Sinkus, M. Tanter, T. Xydeas, S. Catheline, J. Bercoff, and M. Fink, "Viscoelastic shear properties of in vivo breast lesions measured by MR elastography," *Magnetic Resonance Imaging,* vol. 23, no. 2, pp. 159-165, 2005.
[35] A. S. Al-Bsharat, W. N. Hardy, K. H. Yang, T. B. Khalil, S. Tashman, and A. I. King, "Brain/Skull Relative Displacement Magnitude Due to Blunt Head Impact: New Experimental Data and Model," *43rd Stapp Car Crash Conference Proceedings,* p. 14 1999.
[36] H.-S. Kang, R. Willinger, B. M. Diaw, and B. Chinn, "Validation of a 3D Anatomic Human Head Model and Replication of Head Impact in Motorcycle Accident by Finite Element Modeling," *SAE Transactions,* vol. 106, p. 10, 1997.
[37] S. Kleiven and W. N. Hardy, "Correlation of an FE Model of the Human Head with Local Brain Motion--Consequences for Injury Prediction," *Stapp Car Crash Journal,* vol. 46, pp. 123-44, Nov 2002.
[38] J. S. Ruan, T. Khalil, and A. I. King, "Human Head Dynamic Response to Side Impact by Finite Element Modeling," *Journal of Biomechanical Engineering,* vol. 113, no. 3, p. 8, 1991.
[39] E. G. Takhounts, R. H. Eppinger, J. Q. Campbell, R. E. Tannous, E. D. Power, and L. S. Shook, "On the Development of the SIMon Finite Element Head Model," *Stapp Car Crash Journal,* vol. 47, p. 27, 2004.
[40] E. G. Takhounts *et al.*, "Investigation of Traumatic Brain Injuries Using the Next Generation of Simulated Injury Monitor (SIMon) Finite Element Head Model," *Stapp Car Crash Journal,* vol. 52, p. 31, 2008.
[41] C. Giordano, S. Zappalà, and S. Kleiven, "Anisotropic finite element models for brain injury prediction: the sensitivity of axonal strain to white matter tract inter-subject variability," *Biomechanics and Modeling in Mechanobiology,* vol. 16, no. 4, pp. 1269-1293, 2017.
[42] S. Kleiven, "Predictors for Traumatic Brain Injuries Evaluated through Accident Reconstructions," *Stapp Car Crash Journal,* vol. 51, p. 34, 2007.
[43] T. A. Shugar and U. S. N. H. T. S. Administration, *A Finite Element Head Injury Model: Theory, development, and results*. Department of Transportation, National Highway Traffic Safety Administration, 1977.
[44] C. Ward, M. Chan, and A. Nahum, "Intracranial Pressure — A Brain Injury Criterion," *SAE Transactions,* vol. 89, p. 14, 1980.
[45] L. Zhang *et al.*, "Recent advances in brain injury research: a new human head model development and validation," *Stapp Car Crash Journal,* vol. 45, pp. 369-94, Nov 2001.

[46] A. I. King, K. H. Yang, L. Zhang, and W. Hardy, "Is head injury caused by linear or angular acceleration?," in *IRCOBI Conference*, Lisbon, Portugal, 2003, p. 12.
[47] J. Vappou, C. Maleke, and E. E. Konofagou, "Quantitative viscoelastic parameters measured by harmonic motion imaging," (in English), *Physics in Medicine and Biology,* vol. 54, no. 11, pp. 3579-3594, Jun 7 2009.
[48] H. Chen *et al.*, "Harmonic motion imaging for abdominal tumor detection and high-intensity focused ultrasound ablation monitoring: an in vivo feasibility study in a transgenic mouse model of pancreatic cancer," *IEEE Trans Ultrason Ferroelectr Freq Control,* vol. 62, no. 9, pp. 1662-73, Sep 2015.
[49] L. Sandrin *et al.*, "Transient elastography: a new noninvasive method for assessment of hepatic fibrosis," *Ultrasound in Medicine & Biology,* vol. 29, no. 12, pp. 1705-1713, 2003/12/01/ 2003.
[50] K. R. Nightingale, M. L. Palmeri, R. W. Nightingale, and G. E. Trahey, "On the feasibility of remote palpation using acoustic radiation force," (in English), *Journal of the Acoustical Society of America,* vol. 110, no. 1, pp. 625-634, Jul 2001.
[51] R. Muthupillai, D. J. Lomas, P. J. Rossman, J. F. Greenleaf, A. Manduca, and R. L. Ehman, "Magnetic resonance elastography by direct visualization of propagating acoustic strain waves," *Science (New York, N Y),* vol. 269, no. 5232, pp. 1854-7, Sep 29 1995.
[52] N. McDannold and S. E. Maier, "Magnetic resonance acoustic radiation force imaging," *Medical Physics,* vol. 35, no. 8, pp. 3748-58, Aug 2008.
[53] A. Manduca *et al.*, "Magnetic resonance elastography: non-invasive mapping of tissue elasticity," *Medical Image Analysis,* vol. 5, no. 4, pp. 237-54, Dec 2001.
[54] D. Klatt, U. Hamhaber, P. Asbach, J. Braun, and I. Sack, "Noninvasive assessment of the rheological behavior of human organs using multifrequency MR elastography: a study of brain and liver viscoelasticity," *Physics in Medicine and Biology,* vol. 52, no. 24, pp. 7281-7294, 2007.
[55] I. Sack, K.-J. Streitberger, D. Krefting, F. Paul, and J. Braun, "The Influence of Physiological Aging and Atrophy on Brain Viscoelastic Properties in Humans," *PLOS ONE,* vol. 6, no. 9, p. e23451, 2011.
[56] S. M. Atay, C. D. Kroenke, A. Sabet, and P. V. Bayly, "Measurement of the dynamic shear modulus of mouse brain tissue in vivo by magnetic resonance elastography," *Journal of Biomechanical Engineering,* vol. 130, no. 2, p. 021013, 2008.
[57] C. L. Johnson *et al.*, "Local mechanical properties of white matter structures in the human brain," *Neuroimage,* vol. 79, pp. 145-52, Oct 01 2013.
[58] Y. Feng, R. J. Okamoto, R. Namani, G. M. Genin, and P. V. Bayly, "Measurements of mechanical anisotropy in brain tissue and implications for transversely isotropic material models of white matter," *Journal of the Mechanical Behavior of Biomedical Materials,* vol. 23, pp. 117-32, Jul 2013.
[59] M. Hrapko, J. A. W. van Dommelen, G. W. M. Peters, and J. S. H. M. Wismans, "The mechanical behaviour of brain tissue: Large strain response and constitutive modelling," *Biorheology,* vol. 43, no. 43, p. 13, 2006.
[60] J. A. van Dommelen, T. P. van der Sande, M. Hrapko, and G. W. Peters, "Mechanical properties of brain tissue by indentation: interregional variation," *Journal of the Mechanical Behavior of Biomedical Materials,* vol. 3, no. 2, pp. 158-66, Feb 2010.

[61] J. R. Doherty, G. E. Trahey, K. R. Nightingale, and M. L. Palmeri, "Acoustic radiation force elasticity imaging in diagnostic ultrasound," *IEEE Transactions on Ultrasonics, Ferroelectrics, and Frequency Control,* vol. 60, no. 4, pp. 685-701, 2013.
[62] Y. Liu *et al.*, "Concurrent Visualization of Acoustic Radiation Force Displacement and Shear Wave Propagation with 7T MRI," *PLoS One,* vol. 10, no. 10, p. e0139667, 2015.
[63] H. Odeen, J. de Bever, L. W. Hofstetter, and D. L. Parker, "Multiple-point magnetic resonance acoustic radiation force imaging," *Magnetic Resonance in Medicine,* vol. 81, no. 2, pp. 1104-1117, Feb 2019.
[64] K. Nightingale, M. S. Soo, R. Nightingale, and G. Trahey, "Acoustic radiation force impulse imaging: in vivo demonstration of clinical feasibility," *Ultrasound in Medicine & Biology,* vol. 28, no. 2, pp. 227-235, 2002.
[65] Y. Liu *et al.*, "Supersonic transient magnetic resonance elastography for quantitative assessment of tissue elasticity," *Physics in Medicine & Biology,* vol. 62, no. 10, pp. 4083-4106, May 21 2017.
[66] S. A. McAleavey, M. Menon, and J. Orszulak, "Shear-Modulus Estimation by Application of Spatially-Modulated Impulsive Acoustic Radiation Force," *Ultrasonic Imaging,* vol. 29, no. 2, pp. 87-104, 2007.
[67] A. P. Sarvazyan, O. V. Rudenko, S. D. Swanson, J. B. Fowlkes, and S. Y. Emelianov, "Shear wave elasticity imaging: a new ultrasonic technology of medical diagnostics," *Ultrasound in Medicine & Biology,* vol. 24, no. 9, pp. 1419-1435, 1998.
[68] J. Bercoff, M. Tanter, M. Muller, and M. Fink, "The role of viscosity in the impulse diffraction field of elastic waves induced by the acoustic radiation force," *IEEE Transactions on Ultrasonics, Ferroelectrics, and Frequency Control,* vol. 51, no. 11, pp. 1523-1536, 2004.
[69] T. Deffieux, G. Montaldo, M. Tanter, and M. Fink, "Shear Wave Spectroscopy for In Vivo Quantification of Human Soft Tissues Visco-Elasticity," *IEEE Transactions on Medical Imaging,* vol. 28, no. 3, pp. 313-322, 2009.
[70] E. E. Konofagou and K. Hynynen, "Localized harmonic motion imaging: theory, simulations and experiments," *Ultrasound in Medicine & Biology,* vol. 29, no. 10, pp. 1405-1413, 2003.
[71] M. Fatemi and J. F. Greenleaf, "Ultrasound-Stimulated Vibro-Acoustic Spectrography," *Science,* vol. 280, no. 5360, p. 82, 1998.
[72] M. Fatemi and J. F. Greenleaf, "Application of Radiation Force in Noncontact Measurement of the Elastic Parameters," *Ultrasonic Imaging,* vol. 21, no. 2, pp. 147-154, 1999.
[73] S. D. Chen, M. Fatemi, and J. F. Greenleaf, "Quantifying elasticity and viscosity from measurement of shear wave speed dispersion," *Journal of the Acoustical Society of America,* vol. 115, p. 4, 2004.
[74] Z. Hah, C. Hazard, Y. T. Cho, D. Rubens, and K. Parker, "Crawling Waves from Radiation Force Excitation," *Ultrasonic Imaging,* vol. 32, no. 3, pp. 177-189, 2010.
[75] R. Sinkus *et al.*, "Imaging anisotropic and viscous properties of breast tissue by magnetic resonance-elastography," *Magnetic Resonance in Medicine,* vol. 53, no. 2, pp. 372-387, 2005.

[76] M. A. Green, G. Geng, E. Qin, R. Sinkus, S. C. Gandevia, and L. E. Bilston, "Measuring anisotropic muscle stiffness properties using elastography," *NMR in Biomedicine,* vol. 26, no. 11, p. 7, 2013.
[77] D. Klatt, S. Papazoglou, J. Braun, and I. Sack, "Viscoelasticity-based MR elastography of skeletal muscle," *Physics in Medicine and Biology,* vol. 55, no. 21, pp. 6445-6459, 2010.
[78] S. Papazoglou, J. Rump, J. Braun, and I. Sack, "Shear wave group velocity inversion in MR elastography of human skeletal muscle," *Magnetic Resonance in Medicine,* vol. 56, no. 3, pp. 489-497, 2006.
[79] E. C. Qin, L. Jugé, S. A. Lambert, V. Paradis, R. Sinkus, and L. E. Bilston, "In Vivo Anisotropic Mechanical Properties of Dystrophic Skeletal Muscles Measured by Anisotropic MR Elastographic Imaging: The mdx Mouse Model of Muscular Dystrophy," *Radiology,* vol. 273, no. 3, pp. 726-735, 2014.
[80] R. Namani, M. D. Wood, S. E. Sakiyama-Elbert, and P. V. Bayly, "Anisotropic mechanical properties of magnetically aligned fibrin gels measured by magnetic resonance elastography," *Journal of Biomechanics,* vol. 42, no. 13, pp. 2047-2053, 2009.
[81] J. Guo, S. Hirsch, M. Scheel, J. Braun, and I. Sack, "Three-parameter shear wave inversion in MR elastography of incompressible transverse isotropic media: Application to in vivo lower leg muscles," *Magnetic Resonance in Medicine,* vol. 75, no. 4, pp. 1537-1545, 2016.
[82] A. Romano, M. Scheel, S. Hirsch, J. Braun, and I. Sack, "In vivo waveguide elastography of white matter tracts in the human brain," *Magnetic resonance in medicine : official journal of the Society of Magnetic Resonance in Medicine / Society of Magnetic Resonance in Medicine,* vol. 68, no. 5, pp. 1410-22, Nov 2012.
[83] A. T. Anderson *et al.*, "Observation of direction-dependent mechanical properties in the human brain with multi-excitation MR elastography," *Journal of the Mechanical Behavior of Biomedical Materials,* vol. 59, pp. 538-46, Jun 2016.
[84] N. C. Rouze, M. H. Wang, M. L. Palmeri, and K. R. Nightingale, "Finite element modeling of impulsive excitation and shear wave propagation in an incompressible, transversely isotropic medium," *Journal of Biomechanics,* vol. 46, no. 16, pp. 2761-8, Nov 15 2013.
[85] D. Royer, J. L. Gennisson, T. Deffieux, and M. Tanter, "On the elasticity of transverse isotropic soft tissues," *Journal of the Acoustical Society of America,* vol. 129, no. 5, pp. 2757-2760, May 2011.
[86] J. L. Gennisson, S. Catheline, S. Chaffai, and M. Fink, "Transient elastography in anisotropic medium: Application to the measurement of slow and fast shear wave speeds in muscles," (in English), *Journal of the Acoustical Society of America,* vol. 114, no. 1, pp. 536-541, Jul 2003.
[87] S. Aristizabal *et al.*, "Shear wave vibrometry evaluation in transverse isotropic tissue mimicking phantoms and skeletal muscle," *Physics in Medicine and Biology,* vol. 59, no. 24, pp. 7735-7752, 2014.
[88] M. Wang, B. Byram, M. Palmeri, N. Rouze, and K. Nightingale, "Imaging transverse isotropic properties of muscle by monitoring acoustic radiation force induced shear waves using a 2-D matrix ultrasound array," *IEEE Trans Med Imaging,* vol. 32, no. 9, pp. 1671-84, Sep 2013.

[89] C. A. Guertler, R. J. Okamoto, J. L. Schmidt, A. A. Badachhape, C. L. Johnson, and P. V. Bayly, "Mechanical properties of porcine brain tissue in vivo and ex vivo estimated by MR elastography," *Journal of Biomechanics,* vol. 69, pp. 10-18, 2018.
[90] W. Flügge, *Viscoelasticity*, 2d rev. ed. Berlin ; New York: Springer-Verlag, 1975, pp. vii, 194 p.
[91] S. A. Kruse, "Tissue characterization using magnetic resonance elastography: preliminary results," *Physics in Medicine and Biology,* vol. 45, pp. 1579-1590, 2000.
[92] H. Knutsson, C. Westin, and G. Granlund, "Local multiscale frequency and bandwidth estimation," in *Proceedings of 1st International Conference on Image Processing*, 1994, vol. 1, pp. 36-40 vol.1.
[93] A. Manduca, R. Muthupillai, P. J. Rossman, J. F. Greenleaf, and R. L. Ehman, *Image processing for magnetic-resonance elastography* (Medical Imaging 1996). SPIE, 1996.
[94] J. S. Shimony *et al.*, "Quantitative diffusion-tensor anisotropy brain MR imaging: normative human data and anatomic analysis," *Radiology,* vol. 212, no. 3, pp. 770-84, Sep 1999.
[95] S. Mori and P. C. van Zijl, "Fiber tracking: principles and strategies - a technical review," *NMR Biomed,* vol. 15, no. 7-8, pp. 468-80, Nov-Dec 2002.
[96] E. E. Konofagou, C. Maleke, and J. Vappou, "Harmonic Motion Imaging (HMI) for Tumor Imaging and Treatment Monitoring," *Current Medical Imaging Reviews,* vol. 8, no. 1, pp. 16-26, 2012.
[97] C. Maleke, M. Pernot, and E. E. Konofagou, "Single-element focused ultrasound transducer method for harmonic motion imaging," *Ultrasonic Imaging,* vol. 28, no. 3, pp. 144-58, Jul 2006.
[98] R. Sinkus *et al.*, "Potential of MRI and Ultrasound Radiation Force in Elastography: Applications to Diagnosis and Therapy," *Proceedings of the IEEE,* vol. 96, no. 3, pp. 490-499, 2008.
[99] T. Wu, J. P. Felmlee, J. F. Greenleaf, S. J. Riederer, and R. L. Ehman, "MR imaging of shear waves generated by focused ultrasound," *Magnetic resonance in medicine : official journal of the Society of Magnetic Resonance in Medicine / Society of Magnetic Resonance in Medicine,* vol. 43, no. 1, pp. 111-5, Jan 2000.
[100] A. J. Romano *et al.*, "On the feasibility of elastic wave visualization within polymeric solids using magnetic resonance elastography," *The Journal of the Acoustical Society of America,* vol. 116, no. 1, pp. 125-32, Jul 2004.
[101] K. L. Thibault and S. S. Margulies, "Age-dependent material properties of the porcine cerebrum: effect on pediatric inertial head injury criteria," *Journal of Biomechanics,* vol. 31, no. 12, pp. 1119-26, Dec 1998.
[102] L. E. Bilston, Z. Liu, and N. Phan-Thien, "Large strain behaviour of brain tissue in shear: some experimental data and differential constitutive model," *Biorheology,* vol. 38, no. 4, pp. 335-345, 2001 2001.
[103] C. L. Johnson *et al.*, "Magnetic resonance elastography of the brain using multishot spiral readouts with self-navigated motion correction," *Magnetic Resonance in Medicine,* vol. 70, no. 2, pp. 404-12, Aug 2013.
[104] S. M. Smith *et al.*, "Advances in functional and structural MR image analysis and implementation as FSL," *Neuroimage,* vol. 23 Suppl 1, pp. S208-19, 2004.

[105] E. H. Clayton, G. M. Genin, and P. V. Bayly, "Transmission, attenuation, and reflection of shear waves in the human brain," *Journal of the Royal Society Interface,* 2012.
[106] K. B. Arbogast, K. L. Thibault, B. S. Pinheiro, K. I. Winey, and S. S. Margulies, "A high-frequency shear device for testing soft biological tissues," *Journal of Biomechanics,* vol. 30, no. 7, pp. 757-9, Jul 1997.
[107] Y. Feng, R. Namani, R. J. Okamoto, G. M. Genin, and P. V. Bayly, "Anisotropic mechanical properties of brain tissue characterized by shear and indentation tests," presented at the SEM Annual Conference and Exposition on Experimental and Applied Mechanics,, Costa Mesa, CA, 2012.
[108] D. J. Tweten, R. J. Okamoto, and P. V. Bayly, "Requirements for accurate estimation of anisotropic material parameters by magnetic resonance elastography: A computational study," *Magnetic Resonance in Medicine,* Jan 17 2017.
[109] B. M. Sandroff, C. L. Johnson, and R. W. Motl, "Exercise training effects on memory and hippocampal viscoelasticity in multiple sclerosis: a novel application of magnetic resonance elastography," *Neuroradiology,* vol. 59, no. 1, pp. 61-67, 2017.
[110] K.-J. Streitberger *et al.*, "Brain Viscoelasticity Alteration in Chronic-Progressive Multiple Sclerosis," *PLOS ONE,* vol. 7, no. 1, p. e29888, 2012.
[111] J. Wuerfel *et al.*, "MR-elastography reveals degradation of tissue integrity in multiple sclerosis," *NeuroImage,* vol. 49, no. 3, pp. 2520-2525, 2010.
[112] M. C. Murphy *et al.*, "Magnetic resonance elastography of the brain in a mouse model of Alzheimer's disease: initial results," *Magnetic Resonance Imaging,* vol. 30, no. 4, pp. 535-539, 2012.
[113] M. C. Murphy *et al.*, "Decreased brain stiffness in Alzheimer's disease determined by magnetic resonance elastography," *Journal of Magnetic Resonance Imaging,* vol. 34, no. 3, pp. 494-498, 2011.
[114] A. Lipp *et al.*, "Cerebral magnetic resonance elastography in supranuclear palsy and idiopathic Parkinson's disease," *NeuroImage: Clinical,* vol. 3, pp. 381-387, 2013.
[115] J. Weickenmeier, R. de Rooij, S. Budday, P. Steinmann, T. C. Ovaert, and E. Kuhl, "Brain stiffness increases with myelin content," *Acta Biomaterialia,* vol. 42, pp. 265-272, 2016.
[116] J. L. Schmidt *et al.*, "Measurement of anisotropic mechanical properties in porcine brain white matter ex vivo using magnetic resonance elastography," *Journal of the Mechanical Behavior of Biomedical Materials,* vol. 79, pp. 30-37, Mar 2018.
[117] E. H. Clayton and P. V. Bayly, "Brain Response to Extracranial Pressure Excitation Imaged in vivo by MR Elastography," presented at the Society for Experimental Mechanics, Uncasville, Connecticut, 2011.
[118] K. Riek *et al.*, "Wide-range dynamic magnetic resonance elastography," *Journal of Biomechanics,* vol. 44, no. 7, pp. 1380-1386, 2011.
[119] J. D. Humphrey, R. K. Strumpf, and F. C. P. Yin, "Determination of a Constitutive Relation for Passive Myocardium: II.—Parameter Estimation," *Journal of Biomechanical Engineering,* vol. 112, no. 3, pp. 340-346, 1990.
[120] M. D. McGarry *et al.*, "Multiresolution MR elastography using nonlinear inversion," *Medical Physics,* vol. 39, no. 10, pp. 6388-96, Oct 2012.

[121] M. D. McGarry *et al.*, "Suitability of poroelastic and viscoelastic mechanical models for high and low frequency MR elastography," *Medical Physics,* vol. 42, no. 2, pp. 947-57, Feb 2015.
[122] J. Testu *et al.*, "Viscoelastic power law parameters of in vivo human brain estimated by MR elastography," *Journal of the Mechanical Behavior of Biomedical Materials,* vol. 74, pp. 333-341, 2017.
[123] R. C. Koeller, "Applications of Fractional Calculus to the Theory of Viscoelasticity," *Journal of Applied Mechanics,* vol. 51, 1984.
[124] M. Kohandel, S. Sivaloganathan, G. Tenti, and K. Darvish, "Frequency dependence of complex moduli of brain tissue using a fractional Zener model," *Physics in Medicine and Biology,* vol. 50, no. 12, pp. 2799-2805, 2005.
[125] C. Bing *et al.*, "Drift correction for accurate PRF-shift MR thermometry during mild hyperthermia treatments with MR-HIFU," *International Journal of Hyperthermia,* vol. 32, no. 6, pp. 673-687, 2016.
[126] J. D. Poorter, C. D. Wagter, Y. D. Deene, C. Thomsen, F. Ståhlberg, and E. Achten, "Noninvasive MRI Thermometry with the Proton Resonance Frequency (PRF) Method: In Vivo Results in Human Muscle," *Magnetic Resonance in Medicine,* vol. 33, no. 1, pp. 74-81, 1995.
[127] Y. Ishihara *et al.*, "A precise and fast temperature mapping using water proton chemical shift," *Magnetic Resonance in Medicine,* vol. 34, no. 6, pp. 814-823, 1995.
[128] T. Lange, M. Zaitsev, and M. Buechert, "Correction of frequency drifts induced by gradient heating in 1H spectra using interleaved reference spectroscopy," *Journal of Magnetic Resonance Imaging,* vol. 33, no. 3, pp. 748-754, 2011.
[129] A. M. El-Sharkawy, M. Schär, P. A. Bottomley, and E. Atalar, "Monitoring and correcting spatio-temporal variations of the MR scanner's static magnetic field," *Magnetic Resonance Materials in Physics, Biology and Medicine,* vol. 19, no. 5, pp. 223-236, 2006.
[130] R. D. Peters and R. M. Henkelman, "Proton-resonance frequency shift MR thermometry is affected by changes in the electrical conductivity of tissue," *Magnetic Resonance in Medicine,* vol. 43, no. 1, pp. 62-71, 2000.
[131] S. M. Sprinkhuizen, M. K. Konings, M. J. van der Bom, M. A. Viergever, C. J. G. Bakker, and L. W. Bartels, "Temperature-induced tissue susceptibility changes lead to significant temperature errors in PRFS-based MR thermometry during thermal interventions," *Magnetic Resonance in Medicine,* vol. 64, no. 5, pp. 1360-1372, 2010.
[132] A. Boss *et al.*, "Magnetic susceptibility effects on the accuracy of MR temperature monitoring by the proton resonance frequency method," *Journal of Magnetic Resonance Imaging,* vol. 22, no. 6, pp. 813-820, 2005.
[133] X. Zhou, Q. He, A. Zhang, M. Beckmann, and C. Ni, "Temperature measurement error reduction for MRI-guided HIFU treatment," *International Journal of Hyperthermia,* vol. 26, no. 4, pp. 347-358, 2010.
[134] R. T. D. Peters, R. S. Hinks, and R. M. Henkelman, "Ex vivo tissue-type independence in proton-resonance frequency shift MR thermometry," *Magnetic Resonance in Medicine,* vol. 40, no. 3, pp. 454-459, 1998.